Title	Photochemical and Supramolecular Properties of Artificially Constructed Cytochrome b562 Assemblies
Author(s)	梶原，竜太
Citation	大阪大学，2019，博士論文
Version Type	VoR
URL	https://doi.org/10.18910/72363
rights	
Note	

Doctoral Dissertation

Photochemical and Supramolecular Properties of Artificially Constructed Cytochrome b_{562} Assemblies

Ryota Kajihara

January, 2019

Graduate School of Engineering,
Osaka University

Acknowledgement

The study presented in this thesis has been carried out at Department of Applied Chemistry, Graduate School of Engineering, Osaka University from April 2013 to March 2019. The author would like to express his best gratitude to Professor Takashi Hayashi for his continuous guidance, kind suggestions, constant discussions and warm encouragement throughout this research. The author would like to deeply thank Dr. Koji Oohora for his valuable suggestions and helpful discussions.

The author would like to express his gratitude to Dr. Bernard Boitrel at the Institut des Sciences Chemiques de Rennes, Université de Rennes 1 for his kind suggestions and warm encouragement. The author also acknowledges Professor Hidehiro Sakurai and Professor Hiroshi Uyama for reviewing the thesis and their valuable suggestions. The author would like to express his gratitude to Dr. Hiroaki Kitagishi and Ms. Misa Jiromaru for their support in *in vitro* experiments using HeLa cells and confocal microscopy. The author also acknowledges Professor Takayuki Uchihashi for his assistance on high-speed AFM measurements.

The author would like to express his great gratitude to Dr. Akira Onoda for his helpful suggestions and fruitful discussions. Acknowledgement is also made to all members at Professor Takashi Hayashi's group and Dr. Bernard Boitrel's group for their encouragements and friendship in their laboratories.

The author would like to express his great gratitude to his family for their assistance. All the author's work here is dedicated to them. Finally, the author is grateful for financial support by the program of leading graduate schools at Osaka University; Interdisciplinary Program for Biomedical Sciences.

Ryota Kajihara
January 2019

Contents

General Introduction

Protein assembly

In nature, protein assemblies play fundamental roles in biological processes of living organisms.[1] Protein assemblies are constructed by the non-bonding interactions between protein subunits. These assemblies have unique properties and functions derived from the highly-ordered structures. The various assembled structures of proteins such as fibers, rings, and cages are observed in biological systems (Figure 1).

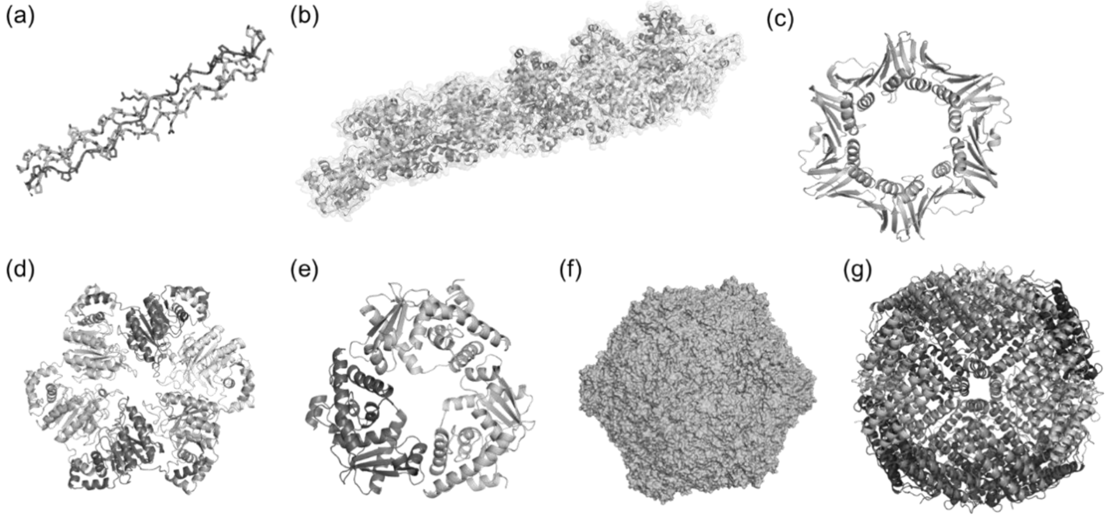

Figure 1. Examples of natural protein assemblies. (a) collagen (PDB: 1BKV), (b) actin filament (PDB: 3G37), (c) β-clamp (PDB: 2POL), (d) gp4 helicase (PDB: 1E0K), (e) λ exonuclease (PDB: 1AVQ), (f) virus capsid of *Cowpea mosaic virus* (PDB: 1NY7), (g) ferritin (PDB: 1FHA)

For example, fibrous protein assemblies (or linear protein assemblies) such as collagen and actin filament support the structure of located tissues (Figure 1a,b). Collagen is found in the extracellular matrix and supports the cell assembled structure of each tissue.[2] Actin filament, one of the cytoskeleton supporting components, regulates the morphology of eukaryotic cells and muscle contraction.[3] The ring-shaped protein assemblies are often found in DNA-related enzymes such as DNA clamp,[4] helicase,[5] nuclease[6] (Figure 1c–e). These ring-shaped enzymes can encircle the DNA strand and involve in fundamental processes of DNA replication, unpacking of double-stranded DNA, and DNA cleavage.[4–6] The cage-like assembly of proteins often has the sphere-like capsule structures with the symmetry of icosahedrons (Figure 1f–h).[7–9] The protein cages have the spatial roles in biological processes to separate the specific molecules from the outer environment. These sphere-like capsule assemblies were often found in virus coat protein, virus capsids (Figure 1f).[7] Virus capsids have robust structure to protect their genomic materials from the outer environment. Other representative protein cages are ferritin[8] and clathrin.[9] They have crucial functions in biochemical and biological processes such as iron ion homeostasis and intracellular trafficking (Figure 1g). Thus, natural protein assemblies have unique functions derived from their assembled morphologies and protein assemblies are promising materials for future applications toward new types of functional biomaterials.

Artificial protein assembly

By mimicking the concept of natural protein assembly, lots of efforts to construct the artificial protein assembly are widely reported for the last decade.[10] Similarly to the natural protein assemblies, the artificial protein assemblies often consist of natural monomeric proteins or small oligomeric proteins in order to construct the higher oligomeric assembly. The various strategies to make artificial protein assemblies are reported so far. These strategies can be classified into two strategies, biological strategy and chemical strategy (Figures 2 and 3).

Biological strategy is a method to employ protein–protein interaction observed in the natural protein assembly. One of the ways to design protein assembly via this strategy is to utilize the natural symmetric protein oligomers as a building block.[11] Yeates *et al.* have reported about the tetrahedral protein cage composed by the fusion protein of C_3-symmetric trimer protein and C_2-symmetric dimer protein subunits (Figure 2a).[11a] Another way of this strategy is the computational design of *de novo* protein assembly.[12] The rational design of protein subunits and protein–protein interface can be achieved by computational simulation in order to construct highly-ordered assembled structures (Figure 2b).

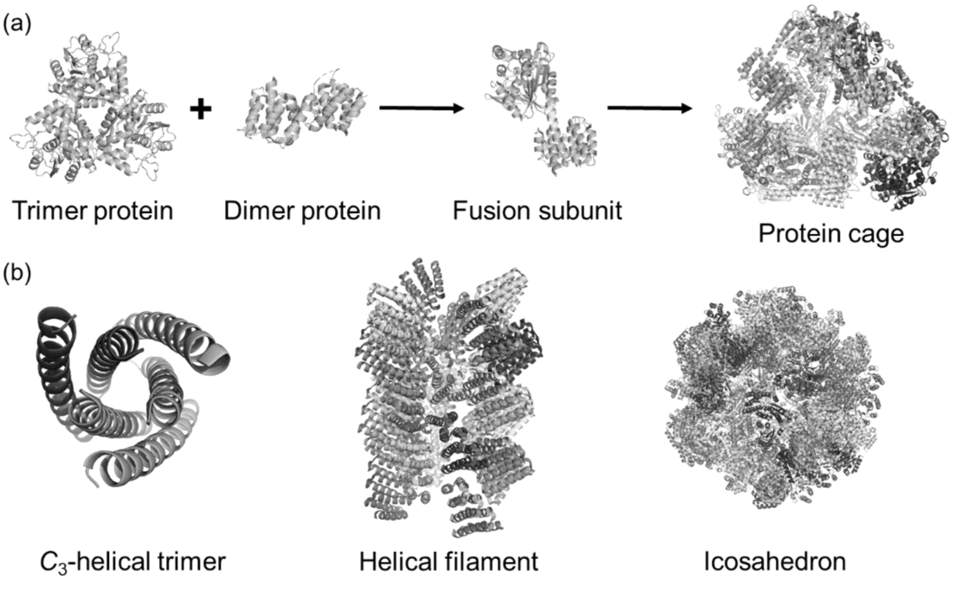

Figure 2. Examples of artificial protein assembly designed by biological strategy: (a) natural symmetry-based assembly (ref. 11a), (b) computationally *de novo* designed assemblies (ref 12).

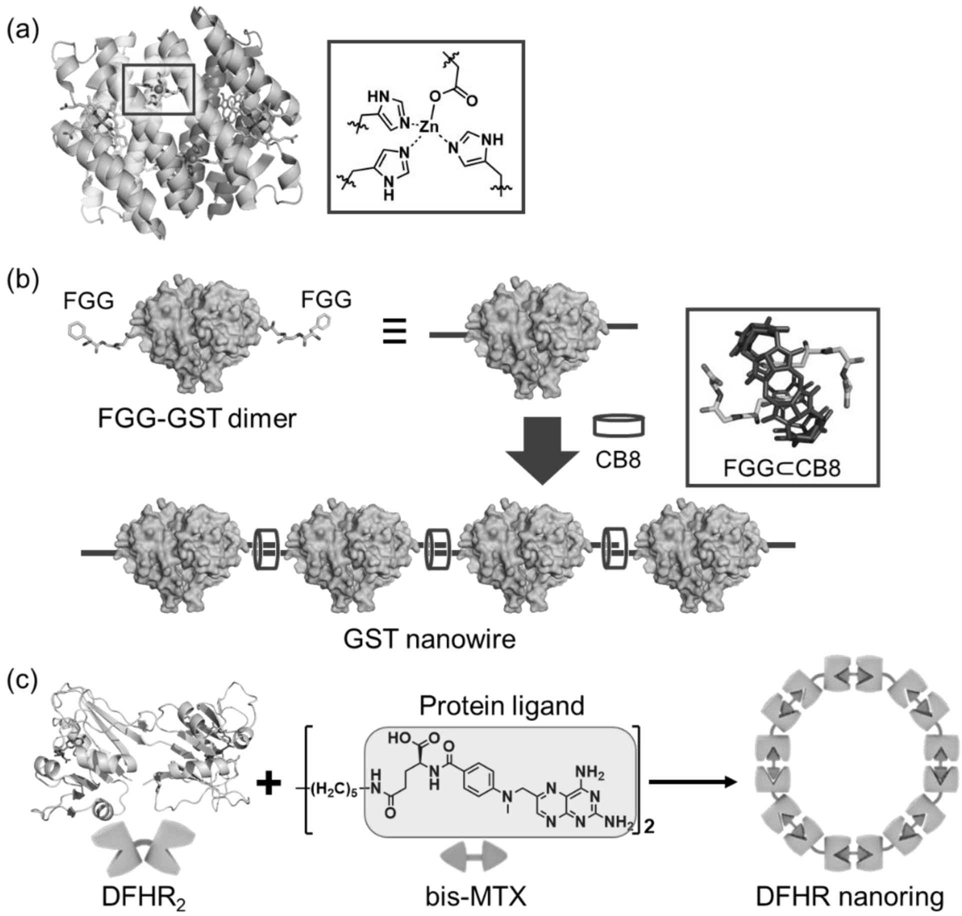

Figure 3. Examples of artificial protein assembly designed by chemical strategy: (a) cytochrome *cb*$_{562}$ tetramer constructed by Zn^{2+} coordination (ref 13), (b) Glutathione S-transferase nanowire designed by the host–guest interaction between FGG peptide and CB8 (ref 14), (c) nanoring assembly of dihydrofolate reductase dimer and bis-methotrexate (bis-MTX) (ref 15).

Chemical strategy utilizes the interactions between protein and compound such as metal coordination, host–guest, and protein–ligand (cofactor) interactions.[13–15] For example, an introduction of the suitable metal coordination site into protein by site-directed mutagenesis drives the assembly upon addition of metal ions. Tezcan *et al.* have reported the cytochrome *cb*$_{562}$ tetramers constructed using the metal coordination bond of Zn^{2+} with the His and Asp residues introduced by mutations (Figure 3a).[13] Next, host–guest interaction between macrocyclic molecules and small peptides or compounds is also useful to produce the protein assembly. One of the examples in this approach is the interaction between cucurbit[8]uril (CB8) and FGG tripeptide.[16] High binding affinity between CB8 and N-terminal FGG-tag sequence enables to form the protein assemblies (Figure 3b).[14] Third method is achieved by employing the protein–ligand interaction or protein–cofactor interaction. Several types of proteins such as enzymes have strong affinities with specific small compounds like ligands and cofactors. This interaction is suitable for the formation of the supramolecular protein assembly. For example, a genetic dimer of enzyme and synthetic dimer of the ligand easily afford the assembled structure (Figure 3c).[15]

Although a variety of artificial protein assemblies with diverse structures are achieved, applications of the artificial protein assemblies have still been under investigations. Several researchers have reported the utilization of the artificial protein assemblies toward light harvesting systems, artificial enzymes, biomedical therapeutic materials and so on (Figure 4).[10,17–19]

Light harvesting system is an array of luminescent pigments to efficiently collect the sunlight with low energy density. The ordered structure of protein assembly is suitable for alignment of the pigment spatially. Liu *et al*. have reported the light harvesting protein assembly using SP1 protein and quantum dots or micelles with pigment molecules.[17] The artificial enzyme based on artificial protein assembly was demonstrated by Tezcan's group. Optimized tetramer of cytochrome cb_{562} was found to show *in vivo* β-lactamase activity.[18] In the biomedical field, protein assemblies are considered as attractive nanomaterials due to its biocompatibility. To date, applications of artificial protein assemblies toward drug delivery, cell–cell interaction, cell recognition have been reported.[19]

Hemoprotein and its application

Hemoprotein is a metalloprotein containing the iron porphyrin complex, heme, as a cofactor and widely exists from archaea to mammalian to play a crucial role in various biological events such as oxidation reactions, gas molecule bindings and electron transfers (Figure 4).[20–22] For instance, cytochrome P450 is a representative heme-containing oxidoreductase which utilizes the high-valent iron-oxo species of heme as an intermediate for the enzymatic reaction.[20] Myoglobin is an O_2-binding hemoprotein to store O_2 molecules in muscle tissues.[21] Cytochromes are a family of the

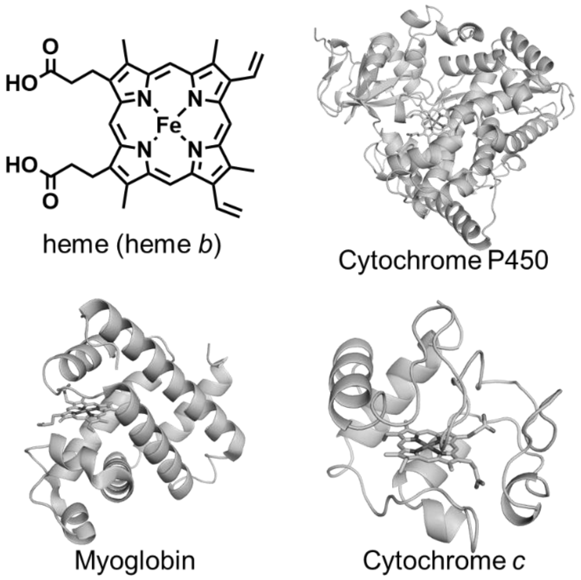

heme (heme *b*)
Cytochrome P450
Myoglobin
Cytochrome *c*

Figure 4. Structure of heme (heme *b*) and representative hemoproteins.

heme-containing electron transporting proteins.[22] The Fe^{2+}/Fe^{3+} redox potentials of heme in cytochromes are important to achieve efficient electron transfer. These unique features are derived from the tuned physicochemical properties of heme by surrounding amino acid residues.

One of the characters of hemoproteins is that heme in protein is replaceable with artificially designed cofactors by "reconstitution method".[23] This reconstitution method is one of the strong approaches to modify the function of hemoprotein. Major strategies to design the artificial prosthetic groups are modifications of peripheral substituents of protoporphyrin IX framework, redesign of macrocyclic structure, and substitution of metal ion center. Especially, modification of the propionate groups of protoporphyrin IX and the metal substitution are simple and effective methods to change the properties of hemoprotein.

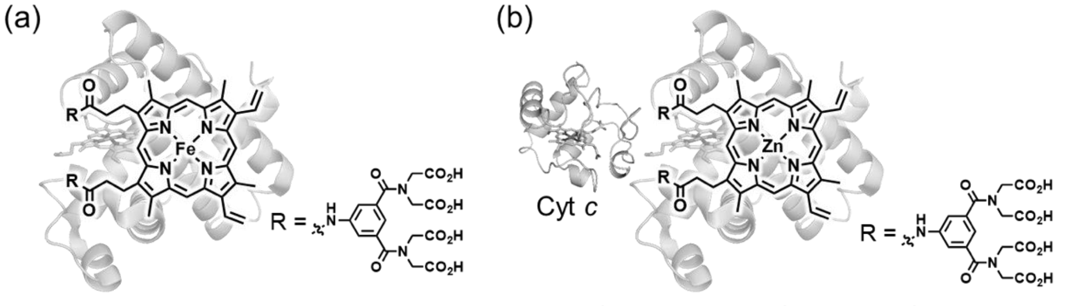

High peroxidase activity

Complexation of rMb with Cyt *c*

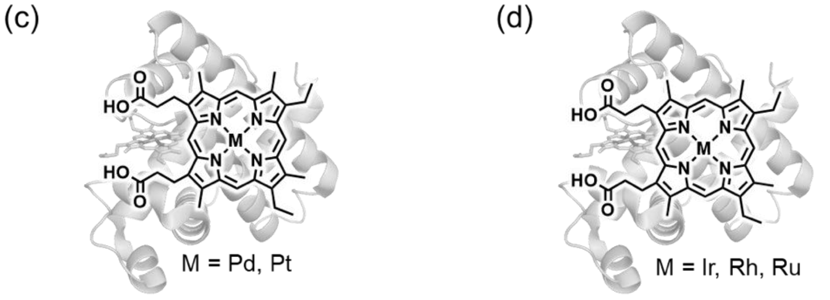

Photosensitizer

Cyclopropanation reaction

Figure 5. Chemical structures of redesigned cofactors and achieved functions of rMb using these cofactors. (a) rMb showing high peroxidase activity. (b) rMb–cytochrome *c* (Cyt *c*) complex. (c) Photosensitizer-containing rMb. (d) rMb catalyzing cyclopropanation of olefins.

Examples of hemoprotein modification with reconstitution method are summarized in Figure 5. Ogoshi and Hayashi *et al.* reported that the reconstituted myoglobin (rMb) with propionate group-modified heme *b* by eight carboxylate groups. The peroxidase activity for oxidation of guaiacol is enhanced by 13-fold compared to native myoglobin.[24] They also demonstrated that this rMb forms a protein complex with cytochrome *c* (Cyt *c*) via electrostatic interaction. By the substitution of the Fe center with Zn ion, this artificial rMb–Cyt *c* complex can achieve the photoinduced electron transfer within the protein complex (Figure 5a,b).[25] Gray *et al.* reported that rMbs with Pd-mesoporphyrin and Pt-mesoporphyrin show intensive phosphorescence emissions and rapid excitation quenching with electron acceptor (Figure 5c).[26] Other metal-substituted rMb was studied by several groups. One of the recent efforts is artificial metalloenzyme catalyzing the cyclopropanation reaction based on myoglobin reconstituted with noble metal porphyrins (Figure 5d).[27] Various hemoproteins and porphyrinoid cofactors have been applied to this strategy. Thus, this strategy is a promising method to modify the characteristics and reactivities of hemoprotein.[23]

Artificial hemoprotein assemblies constructed by heme–heme pocket interaction

Hemoproteins have been focused on as a component of a new biomaterial due to a wide variety of the functions. Especially, utilization of hemoprotein as a building block of protein assembly is considered to be effective in order to construct novel functional nanomaterials.[13,28]

To form artificial hemoprotein assembly, the heme–heme pocket interaction is effective because of high binding affinity between heme and protein matrix ($K > 10^8$ M^{-1}) and having replaceable heme with modified heme or other metalloporphyrin by reconstitution method (*vide supra*). Hayashi *et al.* previously demonstrated the formation of supramolecular hemoprotein assemblies by the strong heme–heme pocket interaction.[29] In these previous works, the cysteine-introduced mutant of hemoprotein is covalently modified by synthetic heme through the selective reaction of cysteine thiol with a functional group such as maleimide. After the removal of intrinsic heme under acidic condition and following neutralization, successive reconstitution of the modified hemoprotein induces the formation of linear hemoprotein assemblies (Figure 6). This is based on the strategy for artificial protein assembly using protein–cofactor interaction.

As a monomer unit of this hemoprotein assembly, cytochrome b_{562} (Cyt b_{562}) was chosen. Cyt b_{562} is one of the electron transporting proteins found in *E. coli*.[30] It is a monomeric hemoprotein with a four-helix bundle structure containing 106 amino acid residues and one heme *b* cofactor. Heme *b* in Cyt b_{562} has a six-coordination low-spin state with Met7 and His102 as axial ligands. In Cyt b_{562}, the protein matrix shows a high binding affinity with heme (K_d = 9 nM)[30b] and high stability against modification and organic solvents. Hayashi *et al.* reported the linear Cyt b_{562} assemblies constructed by H63C mutants (Figure 6).[29] They also demonstrated the formation of 2D Cyt b_{562} network by the linear H63C Cyt b_{562} assembly and a heme triad.[29b] Modification of these assemblies to the inorganic materials such as assembly–nanoparticle conjugate and assembly–electrode conjugate were reported so far.[31] Especially, the electrode conjugated Cyt b_{562} assembly constructed by synthesized zinc porphyrin (ZnP) shows the photocurrent activity derived from the photosensitizer ability of ZnP.

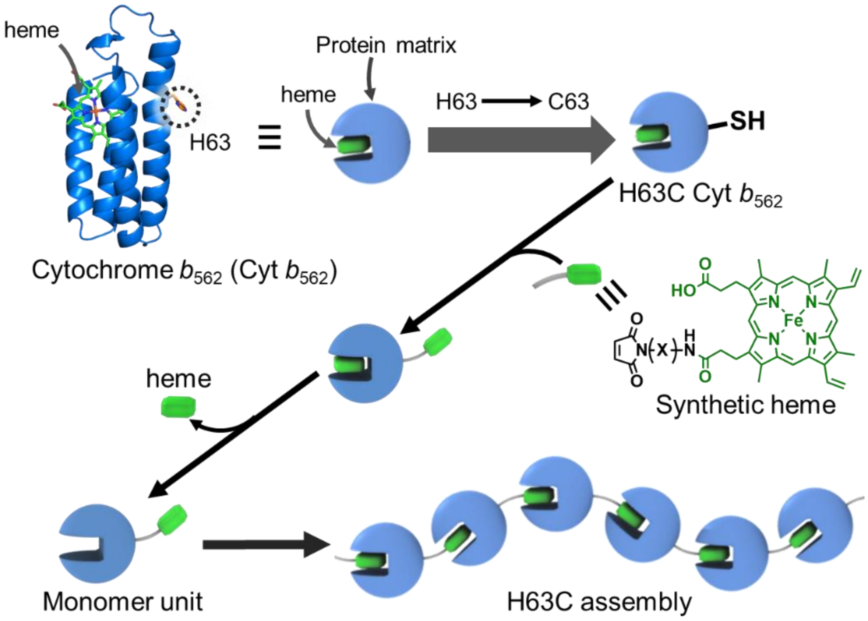

Figure 6. Preparation of Cyt b_{562} assembly using H63C mutant and synthetic heme.

Hayashi and co-workers have recently prepared a Cyt b_{562} assembly using a different mutant, N80C, where the synthesized heme (m–FeP) is attached to the protein surface at the 80th residue (Figure 7).[32] This provides a structurally-defined assembly via the hydrogen bond interaction at the protein interface as a secondary interaction. The linear and periodic helical structure in a solution was characterized by atomic force microscopy (AFM) measurements and circular dichroism (CD) spectroscopy. Especially, CD spectrum of this linear assembly showed a split-type Cotton effect around the wavelength of heme Soret band which is induced by the fixed orientation of heme in the assembly. A mutant assembly of D73A/N80C shows the flexible nature by AFM and CD spectrum due to the lack of secondary hydrogen bond interaction. Moreover, the CD spectrum of the R98A/N80C Cyt b_{562} assembly was found to exhibit an incomplete split-type Cotton effect induced by semi-rigid (or semi-flexible) structure by the weakened hydrogen bond interaction. Thus, the supramolecular structures of this N80C mutant-based assembly can be changed by the simple mutation.

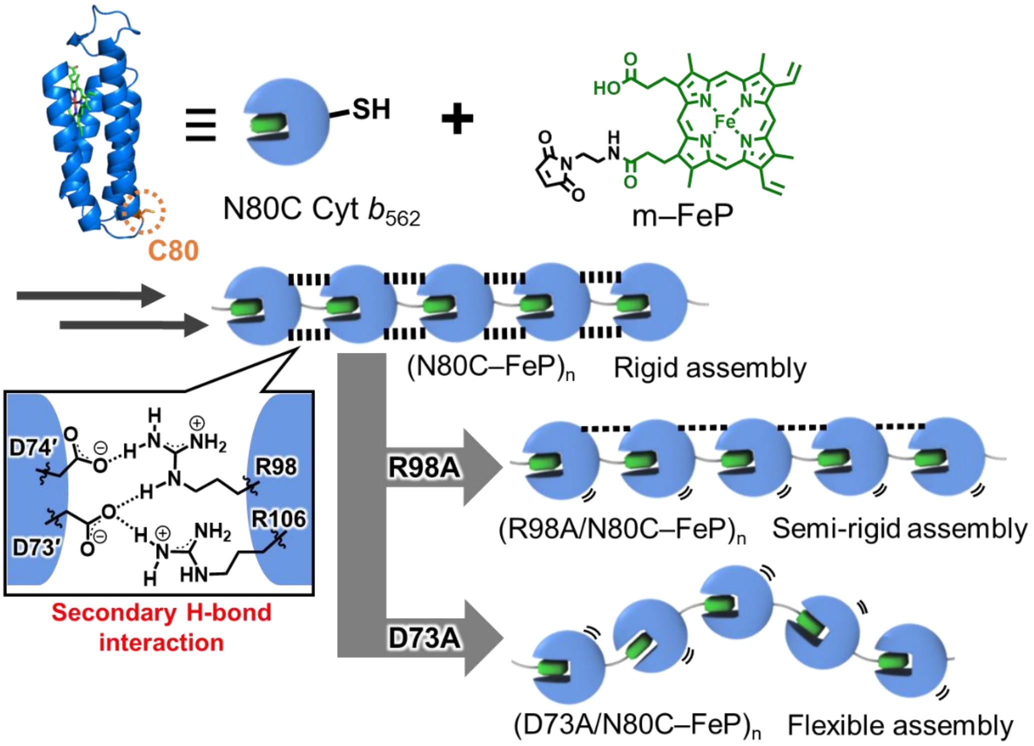

Figure 7. Preparation of three different Cyt b_{562} assemblies based on the N80C mutants, N80C (rigid assembly), R98A/N80C (semi-rigid assembly), and D73A/N80C (flexible assembly).

In order to design the artificial protein assembly for the application to the functional biomaterial, it is necessary to understand the physicochemical properties of their assembling system. Especially, the effect of supramolecular structure to the characteristic of protein assemblies is important to design the sophisticated biomaterials which exhibit the modest properties for their application. Although a variety of artificial protein assemblies are reported hitherto, the protein assemblies which their supramolecular structure are changed by the mutation of their building block are still rare. Thus, the influence of supramolecular structure on the characteristics of protein assemblies is still ambiguous. The author has focused on investigating the influence of changes of supramolecular structure of N80C mutant-based Cyt b_{562} assemblies.

To analyze the effect of mutation-induced rigidity changes, the photochemical properties of Cyt b_{562} assemblies were employed as an indicator because ZnP-containing Cyt b_{562} also provides unique protein assembly. The ZnP has two main photochemical features: (i) intensive fluorescence nature and (ii) long lifetime and high energy of triplet excited states. Therefore, the ZnP-containing Cyt b_{562} assemblies enable the evaluation of the effect of the supramolecular structure on physicochemical properties using these photochemical properties (Chapter 1, 2).

For the design of novel Cyt b_{562} assembly, it is effective to modulate the linker structure between heme (FeP) and maleimide.[29a,33] Modulation of linker structure of Cyt b_{562} assemblies often affects the thermodynamic properties of protein assemblies such as the degree of polymerization and formation of cyclic or spherical supramolecular structures. The author was found the unique property of N80C Cyt b_{562} assembly by employing synthetic FeP with long linker moiety (m–FeP′) (Chapter 3).

Outline of this thesis

Chapter 1: Photoinduced electron transfer within supramolecular cytochrome b_{562} co-assemblies and heterodimers containing Fe and Zn porphyrins

Long-range photoinduced electron transfer between Zn porphyrin and Fe porphyrin (heme) within N80C Cyt b_{562} co-assembly or heterodimer with a well-defined rigid structure. The photoinduced charge separation and subsequent charge recombination were observed in the rigid co-assembly and heterodimer. In contrast, no electron transfer events were observed in a flexible co-assembly and heterodimer. Moreover, analysis of the kinetic constants of electron transfer in heterodimers using Marcus theory suggests that a single-step electron transfer occurs in the system.

Chapter 2: Multivalent effect of arginine residues for cellular uptake of cytochrome b_{562} assembly

Cellular uptake behaviors of N80C mutant-based Cyt b_{562} assemblies were investigated. Multiply arrayed oligoarginine tags, one of the cell-penetrating peptides, on the protein surfaces of the Cyt b_{562} assemblies improve the efficiency of cellular uptake into HeLa cells in a manner which depends on the number of arginine residues in the tags and rigidity of the Cyt b_{562} assemblies. A rigid assembly with tetraarginine tag shows 10-fold higher cellular uptake efficiency than a corresponding rigid assembly without oligoarginine tags.

Chapter 3: Thermodynamically controlled formation of ring-shaped trimer and linear assembly of cytochrome b_{562}

N80C Cyt b_{562} assembly constructed by the modification of heme with a moderately long linker exhibits the two equilibrium states: long linear oligomer under a high concentrated protein condition and ring-shaped trimer under a diluted protein condition. The ring-shaped trimer of Cyt b_{562} is thermodynamically more stable than linear assembly in a dilute condition. Moreover, the isolated ring-shaped trimer is kinetically trapped even in a concentrated solution.

References

(1) Pieters, B. J. E.; van Eldijk, M. B.; Nolte, R. J. M.; Mecinovic, J. *Chem. Soc. Rev.* **2016**, *45*, 24-39

(2) Shoulders, M. D.; Raines, R. T. *Annu. Rev. Biochem*. **2009**, *78*, 929–958.

(3) Dominguez, R.; Holmes, K. C. *Annu. Rev. Biochem*. **2009**, *78*, 929–958.

(4) O'Donnell, M.; Kuriyan, J.; Kong, X.-P.; Stukenberg, P. T.; Onrust, R. *Mol. Biol. Cell.* **1992**, *3*, 953–957.

(5) Singleton, M. R.; Sawaya, M. R.; Ellenberger, T.; Wigley, D. B. *Cell.* **2000**, *101*, 589–600.

(6) Kovall, R. A.; Matthews, B. W. *Proc. Natl. Acad. Sci. U. S. A.* **1998**, *95*, 7893–7897.

(7) Lin, T.; Chen, Z.; Usha, R.; Stauffacher, C. V.; Dai, J.-B.; Schmidt, T.; Johnson, J. E. Virology. **1999**, *265*, 20–34.

(8) Liu, X.; Theil, E. C. *Acc. Chem. Res.* **2005**, *38*, 167–175.

(9) Fotin, A.; Cheng, Y.; Sliz, P.; Grigorieff, N.; Harrison, S. C., Kirchhausen, T.; Walz, T. *Nature*. **2004**, *432*, 573–579.

(10) (a) Luo, Q.; Hou, C.; Bai, Y.; Wang, R.; Liu, J. *Chem. Rev.* **2016**, *116*, 13581–13632. (b) Bai. Y.; Luo. Q.; Liu. J.; *Chem. Soc. Rev*. **2016**, *45*, 2756–2767. (c) Levy, Y. *Biochemistry*. **2017**, *56*, 5040–5048.

(11) (a) Lai, Y. T.; Tsai, K. L.; Sawaya, M. R.; Asturias, F. J.; Yeates, T. O. *J. Am. Chem. Soc*.,**2013**, *135*, 7738–7743. (b) Lai, Y. T.; Reading, E.; Hura, G. L.; Tsai, K, L.; Laganowsky, A.; Asturias, F. J.; Tainer, J. A.; Robinson, C. V.; Yeates, T. O. *Nat. Chem.* **2014**, *6*, 1065–1071.

(12) (a) Boyken. S. E.; Chen, Z.; Groves, B.; Langan, R. A.; Oberdorfer, G.; Ford, A.; Gilmore, J. M.; Xu, C.; DiMaio, F.; Pereira, J. H.; Sankaran, B.; Seelig, G.; Zwart, P. H.; Baker, D. *Science*. **2016**, *352*, 680–687. (b) Shen, H.; Fallas, J. A.; Lynch, E.; Sheffler, W.; Parry. B.; Jannetty, N.; Decarreau, Justin; Wagenbach, M.; Vicente, J. J.; Chen. J.; Wang, L.; Dowling, Q.; Oberdorfer, G.; Stewart, L. Wordeman, L.; de Yoreo, J.; Jacobs-Wagner, C.; Kollman, J.; Baker, D. *Science*. **2018**, *362*, 705–709. (c) Bale, J. B.; Gonen, S.; Liu, Y.; Sheffler, W.; Ellis, D.; Thomas, C.; Cascio, D.; Yeates, T. O.; Gonen, T.; King, N. P.; Baker, D. *Science*. **2016**, *353*, 389–394.

(13) (a) Salgado, E. N.; Ambroggio, X. I.; Brodin, J. D.; Lewis, R. A.; Kuhlman, B.; Tezcan, F. A. *Proc. Natl. Acad. Sci. U. S. A.* **2010**, *107*, 1827–1832. (b) Brodin, J. D.; Ambroggio, X. I.; Tang, C.; Parent, K. N.; Baker, T. S. Tezcan, F. A. *Nat. Chem.* **2012**, *4*, 375–382.

(14) Hou, C.; Li, J.; Zhao, L.; Zhang, W.; Luo, Q.; Dong, Z.; Xu, J.; Liu, J. *Angew. Chem. Int. Ed.* **2013**, *52*, 5590–5593.

(15) Carlson, J. C. T.; Jena, S. S.; Flenniken, M.; Chou, T.; Siegel, R. A.; Wagner, C. R. *J. Am. Chem. Soc.* **2006**, *128*, 7630–7638.

(16) Heitmann, L. M.; Taylor, A. B.; Hart, J.; Urbach, A. R. *J. Am. Chem. Soc*. **2006**, *128*, 12574–12581.

(17) (a) Miao, L.; Han, J.; Zhang, H.; Zhao, L.; Si, C.; Zhang, X.; Hou, C.; Luo, Q.; Xu, J.; Liu, J. *ACS Nano*. **2014**, *8*, 3743–3751. (b) Sun, H.; Zhang, X.; Miao, L.; Zhao, L.; Luo, Q.; Xu, J.; Liu, J. *ACS Nano*. **2016**, *10*, 421–428.

(18) Song, W. J.; Tezcan, F. A. *Science*. **2014**, *346*, 1525–1528.

(19) (a) Li, Q.; So, C. R.; Fegan, A.; Cody, V.; Sarikaya, M.; Vallera, D. A.; Wagner, C. R. *J. Am. Chem. Soc.*

2010, *132*, 17247–17257. (b) Fegan, A.; Kumarapperuma, S. C.; Wagner, C. R.: *Mol. Pharmaceutics*. **2012**, *9*, 3218–3227. (c) Petersburg, J. R.; Shen, J.; Csizmar, C. M. Murphy, K. A.; Spanier, J.; Gabrielse, K.; Griffith, T. S.; Fife, B.; Wagner, C. R. *ACS Nano*. **2018**, *12*, 6563–6576.

(20) Meunier, B.; de Visser, S. P.; Shaik, S. *Chem. Rev*. **2004**, *104*, 3947–3980.

(21) Kendrew, J. C.; Bodo, G.; Dintzis, H. M.; Parrish, R. G.; Wyckoff, H. *Nature*. **1958**, *181*, 662–666.

(22) Liu, J.; Chakraborty, S.; Hosseinzadeh, P.; Yu, Y.; Tian, S.; Petrik, I. *Chem. Rev.* **2014**, *114*, 4366–4469.

(23) Hayashi, T.; Hisaeda, Y. *Acc. Chem. Res.* **2002**, *35*, 35–43.

(24) Hayashi. T.; Hitomi, Y.; Ando, T.; Mizutani, T.; Hisaeda, Y.; Kitagawa, S.; Ogoshi, H. *J. Am. Chem. Soc*. **1999**, *121*, 7747–7750.

(25) Hayashi, T.; Hitomi, Y.; Ogoshi, H. *J. Am. Chem. Soc*. **1998**, *120*, 4910–4915.

(26) Cowan, J. A.; Gray, H. B.; *Inorg. Chem*. **1989**, *28*, 2074–2078.

(27) (a) Key, H. M.; Dydio, P.; Clark, D. S.; Hartwig, J. F. *Nature*. **2016**, *534*, 534–537. (b) Sreenilayam, G.; Moore, E. J., Steck, V.; Fasan, R. *Adv. Synth. Catal.* **2017**, *359*, 2076–2089.

(28) (a) Hirota, S.; Hattori, Y.; Nagao, S.; Taketa, M.; Komori, H.; Kamikubo, H.; Wang, Z.; Takahashi, I.; Negi, S.; Sugiura, Y.; Kataoka, M.; Higuchi, Y. *Proc. Natl. Acad. Sci. U. S. A.* **2010**, *107*, 12854–12859. (b) Miyamoto, T.; Kuribayashi, M.; Nagao, S.; Shomura, Y.; Higuchi, Y.; Hirota, S. *Chem. Sci.* **2015**, *6*, 7336–7342.

(29) (a) Kitagishi, H.; Oohora, K.; Yamaguchi, H.; Sato, H.; Matsuo, T.; Harada, A.; Hayashi, T. *J. Am. Chem. Soc*. **2007**, *129*, 10326–10327. (b) Kitagishi, H.; Kakikura, Y.; Yamaguchi, H.; Oohora, K.; Harada, A.; Hayashi, T. *Angew. Chem. Int. Ed.* **2009**, *48*, 1271–1274.

(30) (a) Nikkila, H.; Gennis, R. B.; Sligar, S. G. *Eur. J. Biochem*. **1991**, *202*, 309–313. (b) Robinson, C. R.; Liu, Y.; Thomson, J. A.; Sturtevant, J. M.; Sligar, S. G. *Biochemistry.* **1997**, *36*, 16141–16146.

(31) (a) Oohora, K.; Onoda, A.; Hayashi, T. *Chem. Commun*. **2012**, *48*, 11714–11726. (b) Onoda, A.; Ueya, Y.; Sakamoto, T.; Uematsu, T.; Hayashi, T. *Chem. Commun*. **2010**, *46*, 9107–9109. (c) Onoda, A.; Kakikura, Y.; Uematsu, T.; Kuwabata, S.; Hayashi, T. *Angew. Chem. Int. Ed.* **2012**, *51*, 2628–2631.

(32) Oohora, K.; Nishiki, F.; Kajihara, R.; Watanabe, H.; Uchihashi, T.; Hayashi, T. *J. Am. Chem. Soc*. **2018**, *140*, 10145–10148.

(33) Oohora, K.; Onuma, Y.; Tanaka, Y.; Onoda, A.; Hayashi, T. *Chem. Commun*. **2017**, *53*, 6879–6882.

Chapter 1

Photoinduced electron transfer within supramolecular cytochrome *b*$_{562}$ co-assemblies and heterodimers containing Fe and Zn porphyrins

1-1. Introduction

The biochemical processes of respiration and photosynthesis both include numerous precise electron transfer (ET) processes mediated by lots of metalloproteins and cofactors.[1–4] It is of particular interest that proteins provide a suitable medium to achieve efficient ET reactions over distances as long as 15 Å because of the efficient electronic coupling and low reorganization energy provided protein polypeptide chain.[2] These long-range ET reactions via protein matrices are often found in natural protein complexes as well as artificially constructed systems containing two or more redox-active site.[2,3,5,6] Generally, the kinetic constants of ET depend on the donor–acceptor distances.[2,3,7] The distance decay constant (*β*) of electron tunneling in a protein is usually within the range of 1.0–1.3 Å^{-1} which is a much smaller range relative to tunneling ranges measured in aqueous solution. Long-range ET reactions with donor–acceptor distances greater than 25 Å in a protein are rare, with the exception of multistep electron hopping through intermediate redox-active aromatic residues (e.g. Tyr, Trp)[5] and/orother redox-active molecules.[4,6] Therefore, a single-step ET over a 25 Å-distance requires a suitable protein scaffold and/or an appropriate protein–protein interface to achieve efficient electron coupling for interprotein ET reactions. Particularly, in the latter case, we recognized that an artificial metalloproteins complex or assembly would provide a useful tool to understand such long range ET processes within a unique protein–protein complex. Over the last two decades, functional modeling efforts using engineered metalloproteins complexes have been successful in elucidating the mechanisms of the ET events.[8] In this respect, recent investigations of artificial metalloproteins assemblies such as hemoprotein assemblies[9] are expected to contribute to the creation of new classes of ET systems. However, demonstrations of ET events occurring within these metalloproteins assemblies have been quite limited thus far.

The previously reported hemoprotein assembly which is designed using N80C mutant of Cyt *b*$_{562}$ and synthetic heme (m–FeP) exhibited the rigid and periodic assembly by the secondary hydrogen bond (H-bond) between protein matrices (*vide supra*).[10] It is also reported that by the mutation of the residues which are related to the secondary H-bond interaction in this assembling system resulted in the weakened interaction or depleted interaction to form semi-rigid or flexible assembly, respectively. Thus, this N80C mutant-based assembling system is suitable to evaluate the effect of non-bonding interaction between protein matrices. Moreover, these Cyt *b*$_{562}$ assemblies can be designed using artificial ZnP (m–ZnP), which the ZnP are often applied to the studies of photoinduced electron tunneling.

Over the past two decades, several investigations of ET systems using Zn porphyrin have been conducted using synthetic molecules[11] and hemoprotein complexes.[8,12] In the latter case, Zn-substituted hemoprotein complexes have been investigated including: complexes of Cyt *c*/Zn-substituted cytochrome *c* peroxidase, cytochrome *b*$_5$/Zn-substituted myoglobin, hemoglobin constructed by Zn porphyrin reconstituted α-subunits, rMb with Zn porphyrin/Cyt *c*, and a co-crystal of Cyt *c*/Zn-substituted Cyt *c*, where ferric heme acts as the electron acceptor from photoexcited Zn porphyrin.[8,12] In contrast, in the present work, the author has investigated the long-range and single-step photoinduced ET between the donor and acceptor with a 29-Å distance in the N80C-based Cyt *b*$_{562}$ co-assemblies containing the heme (FeP) and the ZnP (Figure 1-1a). Furthermore, the photoinduced ET reactions are also investigated in a simple system using six different N80C-based Cyt *b*$_{562}$ heterodimers (Fe-Zn dimers and Zn-Fe dimers; Figure 1-1b).

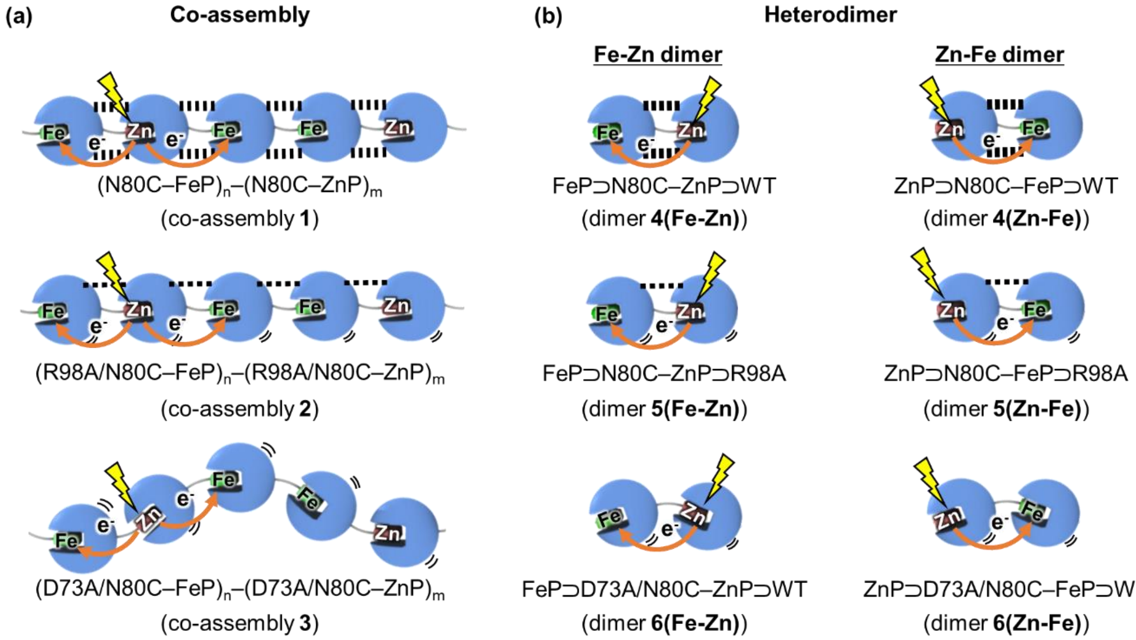

Figure 1-1. Photoinduced ET in (a) three different N80C mutant-based Cyt *b*$_{562}$ co-assemblies and (b) six different Cyt *b*$_{562}$ heterodimers (Fe-Zn dimers and Zn-Fe dimers)

1-2. Results and Discussion

Preparation and characterization of Cyt *b*562 assemblies, co-assemblies, and heterodimers.

The Cyt b_{562} assemblies containing FeP ((N80C–FeP)$_n$, (R98A/N80C–FeP)$_n$, (D73A/N80C–FeP)$_n$) were prepared as previously reported.[10] The Cyt b_{562} assemblies containing ZnP ((N80C–ZnP)$_m$, (R98A/N80C–ZnP)$_m$, and (D73A/N80C–ZnP)$_m$) were prepared in a reaction of N80C with maleimide-linked ZnP on the surface of the protein as shown in Figure 6. After denaturation by guanidine-HCl (GdmCl), heme and excess maleimide-linked ZnP were removed by extraction using 2-butanone and the aqueous solution was then neutralized. The obtained protein units were identified by ESI-TOF MS and UV-vis spectra. The CD spectrum of (N80C–ZnP)$_m$ exhibits the split-type Cotton effect in the range of 390–450 nm, which indicates that ZnP has a fixed orientation in the assembly (Figures 1-2)

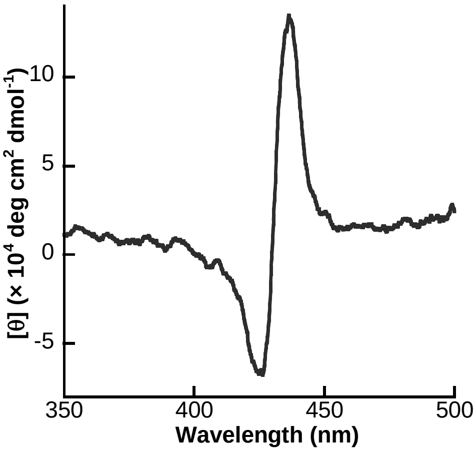

Figure 1-2. CD spectrum of (N80C–ZnP)m in 100 mM potassium phosphate buffer, pH 7.0, at 20 °C.

The Cyt b_{562} co-assemblies (co-assemblies **1**, **2**, and **3**) were prepared by mixing the FeP-containing assembly and the ZnP-containing assembly and the changes of the profiles in size exclusion chromatography (SEC) were reached within 10 h, indicating attainment of equilibrium. The resulting co-assemblies were identified by UV-vis spectra (Figures 1-3a, 1-4).

The six different Cyt b_{562} heterodimers (Figure 1-1b) were also prepared by mixing of two proteins via maleimide-thiol conjugation (Figure 1-3b–d), and purified by SEC. The obtained heterodimers were identified by UV-vis spectra and SEC (Figure 1-5).

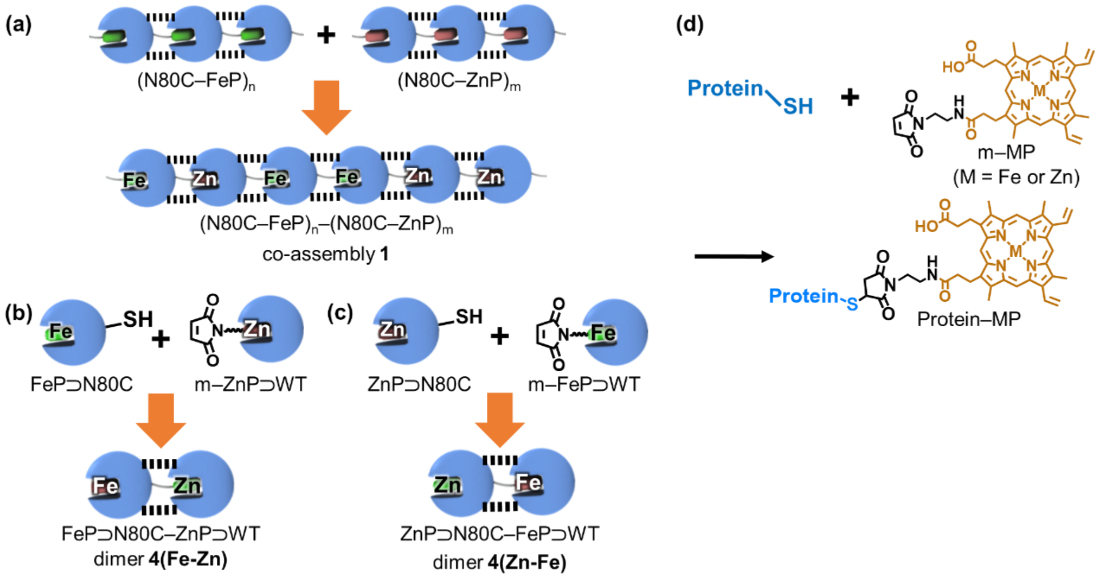

Figure 1-3. Preparation methods for (a) co-assembly **1**, (b) dimer **4(Fe-Zn)**, and (c) dimer **4(Zn-Fe)**, and (d) a schematic representation of the reaction between the protein scaffold and the maleimide-linked metalloporphyrin (m–MP: M = Fe or Zn) via maleimide–thiol conjugation.

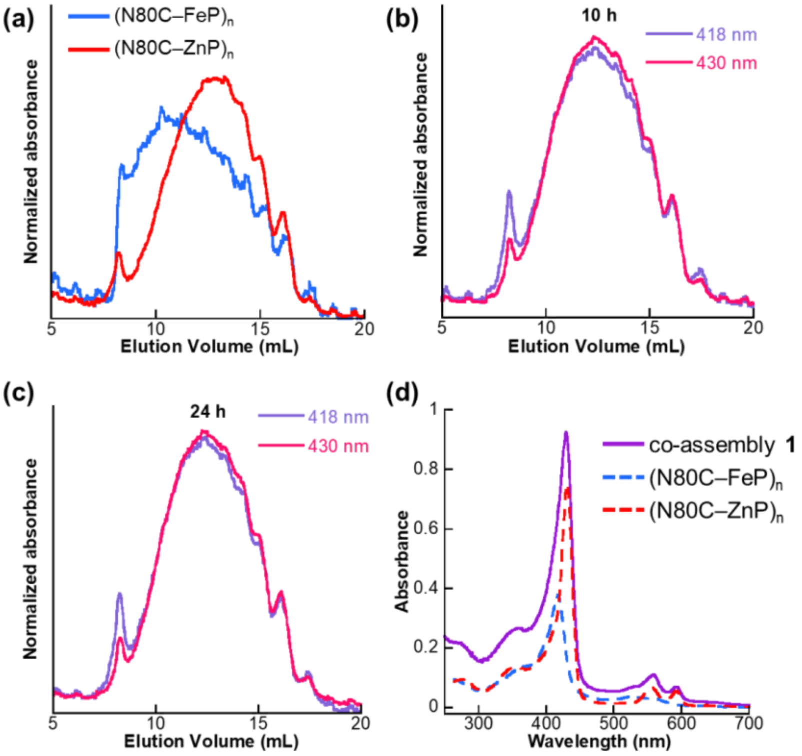

Figure 1-4. Characterization of co-assembly **1**. Size exclusion chromatography traces of (a) $(N80C–FeP)_n$ (blue) and $(N80C–ZnP)_m$ (red), and (b, c) co-assembly **1** (n/m = 1/1) after mixing the assemblies for (b) 10 h and (c) 24 h at room temperature. These traces were monitored at 418 nm (violet) and 430 nm (red), which are the λ_{max} of Cyt b_{562} and ZnP⊃WT, respectively. (d) UV-vis spectra of co-assembly **1** (n/m = 1/1, violet), $(N80C–FeP)_n$ (blue) and $(N80C–ZnP)_m$ (red). Condition: [N80C–ZnP] = 3 μM and [N80C–FeP] = 3 μM in 100 mM potassium phosphate buffer, pH 7.0, Superdex 200 10/300 GL.

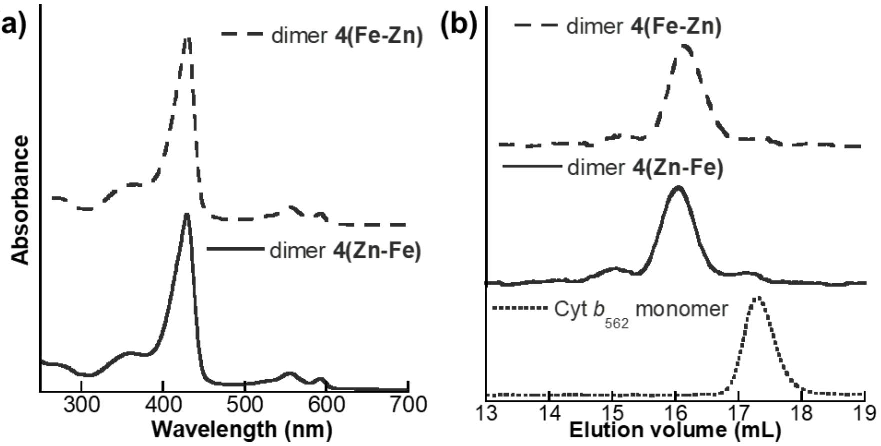

Figure 1-5. Characterization of dimers **4(Zn-Fe)** and **4(Fe-Zn)**. (a) UV-vis spectra of dimers **4(Fe-Zn)** (dash line) and **4(Zn-Fe)** (solid line). (b) SEC traces of dimers **4(Fe-Zn)** and **4(Zn-Fe)**, and Cyt b_{562} (dotted line). Condition: Superdex 200 increase column.

Evaluation of photoinduced ET in the co-assemblies

Photoinduced ET reactions within the co-assemblies and heterodimers were investigated by observing transient absorption changes after ns-pulse laser flash photolysis. According to previous reports using ET systems containing hemoproteins with Zn and Fe porphyrins, the charge separation (CS) within co-assemblies and heterodimers should occur via the long-lived triplet excited states of ZnP (~10 ms), whereas the involvement of singlet excited states is ruled out owing to the short excitation lifetime (~1 ns) for their long donor–acceptor distance (29 Å).[2,8c] Thus, the photochemical process after electronic excitation within these co-assemblies and heterodimers is proposed as shown in Scheme 1-1: (i) photoexcitation to generate the singlet state of the ZnP species (^{1}ZnP); (ii) intersystem crossing to obtain the long-lived triplet excited state (^{3}ZnP); (iii) CS between ^{3}ZnP and the ferric FeP (Fe^{3+}P) in the protein co-assemblies and heterodimers; (iv) charge recombination (CR) between the ZnP radical cation species (ZnP$^{\bullet+}$) and the ferrous FeP (Fe^{2+}P) to recover the ground state.

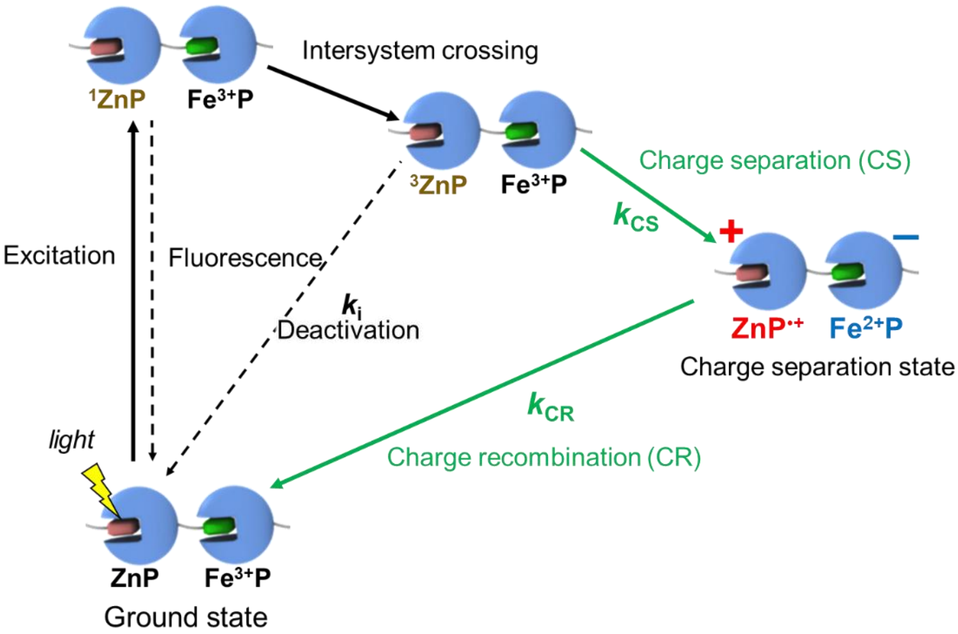

Scheme 1-1. Photochemical process of oxidative ET in the co-assemblies and heterodimers

First, flash photolysis transient absorption measurements of co-assembly **1**, which has a rigid structure derived from the H-bond interaction was performed. The decay curves of the 460 nm absorption band of ^{3}ZnP were monitored in co-assemblies **1** having various *n/m* ratios (*n/m* = 1/1, 2/1, 3/1) and (N80C–ZnP)$_m$ (Figures 1-6a). Biexponential decay curves (eq 1) were observed for the co-assemblies, whereas the decay for (N80C–ZnP)$_m$ was found to generate a monoexponential decay curve (eq 2).

$$\Delta\text{Abs} = \alpha e^{-k_a t} + \beta e^{-k_i t} \tag{1}$$

$$\Delta\text{Abs} = \beta e^{-k_i t} \tag{2}$$

These findings indicate that CS occurs within the co-assemblies. The biexponential fitting parameters include two kinetic constants, k_i and k_a: the former is the triplet decay constant without ET and the latter is the sum of the k_i and k_{CS}, a kinetic constant of CS. The obtained kinetic parameters are summarized in Table 1-1. The slower decays observed in the co-assemblies correspond to the deactivation of ^{3}ZnP in (N80C–ZnP)$_m$ (k_i = 90 ± 3 s^{-1}). The average k_{CS} values of the co-assemblies were determined to be approximately 530 ± 40 s^{-1}. Interestingly, the k_i and k_{CS} values were found to be mostly independent of the *n/m* ratio while the populations of decay components depend on the *n/m* ratio: an increase in the *n/m* ratio in the co-assembly provides a larger population of the faster decay component ($\alpha/(\alpha + \beta)$) as shown in Table 1-1. This finding appears to be reasonable because not all of the N80C–ZnP units in the co-assembly contribute to the ET reactions due to the successive alignment of

N80C–ZnP units. Additionally, the N80C–ZnP units with the successive alignments in the co-assembly should statistically decrease with the increase of the ratio of *n/m*.

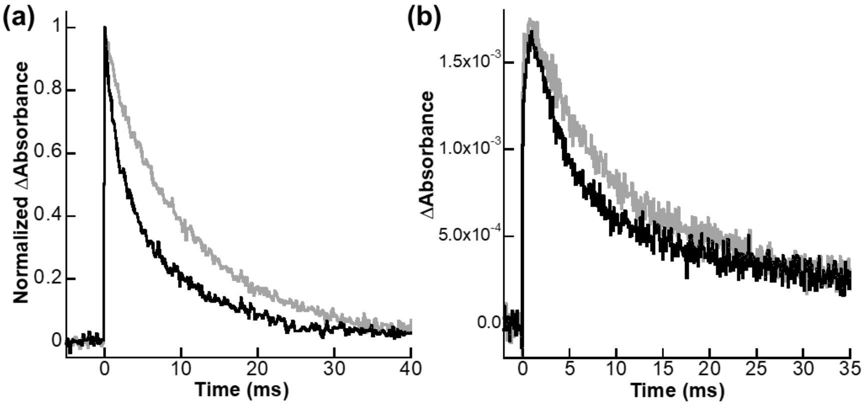

Figure 1-6. Transient absorption decay of (N80C–ZnP)$_m$ (grey) and co-assembly 1 (*n/m* = 3/1, black). (a) Normalized transient absorption decay at 460 nm and (b) 680 nm.

Table 1-1. Electron Transfer Kinetic Parameters for Co-assembly **1**[a]

n/m	$\frac{\alpha}{\alpha+\beta}$[b]	$\frac{\beta}{\alpha+\beta}$[b]	k_{CS} (s^{-1})[b]	k_{CR} (s^{-1})[c]	k_i (s^{-1})[b]
0/1[d]	—	—	—	—	90 ± 3[e]
1/1	0.25 ± 0.02	0.75 ± 0.02	530 ± 62	910 ± 90	81 ± 3
2/1	0.31 ± 0.08	0.69 ± 0.08	510 ± 100	974 ± 120	94 ± 10
3/1	0.44 ± 0.02	0.56 ± 0.02	520 ± 30	913 ± 120	91 ± 4
average[f]	—	—	530 ± 40	930 ± 50	87 ± 3

[a] Conditions: [N80C–ZnP] = 3 μM and [N80C–FeP] = 0–9 μM in 100 mM potassium phosphate buffer, pH 7.0, at 20 °C under an N_2 atmosphere. [b] Parameters were obtained from eq 1. [c] k_{CR} was obtained from eq 3. [d] Transient decay of (N80C–ZnP)$_m$. [e] k_i was obtained from eq 2. [f] The averaged kinetic constants of co-assembly **1** were calculated using all of the experimental results.

The kinetic constants of CR in co-assembly **1** were also evaluated by monitoring the transient absorption changes of the ZnP$^{\bullet+}$ species which has a characteristic peak at 680 nm (Figures 1-6b). The absorption of the co-assembly **1** at 680 nm after laser irradiation rapidly increase within 1 ~ 2 ms and then undergoes fast decay within 3 ~ 5 ms and slow decay afterwards. Table 1-1 shows the summary of kinetic parameters analyzed by eq 3.

$$\Delta \mathrm{Abs} = a_1 e^{-k_a t} + a_2 e^{-k_{CR} t} + a_3 e^{-k_i t} \tag{3}$$

The kinetic constants of CR, k_{CR}, are determined to be 930 ± 50 s^{-1} on average. Similar to the results inferred from the k_{CS} values, no correlation was observed between the kinetic constants and the *n/m* ratio.

Next, an investigation of transient absorption spectral changes of co-assembly **2** with a semi-rigid structure (*vide supra*) after the laser flash photolysis was carried out in the same manner used to investigate co-assembly **1** (Figures 1-7). The kinetic parameters are summarized in Table 1-2. The averaged values of k_{CS}, k_{CR}, and k_{i} for co-assembly **2** were determined to be 300 s^{-1}, 430 s^{-1}, and 88 s^{-1}, respectively. The k_{CS} and k_{CR} values of the semi-rigid co-assembly are both smaller than those of the rigid co-assembly, whereas the k_{i} values are close to each other. These results indicate two important characteristics of co-assembly **2**: the photochemical properties of the ^{3}ZnP of co-assembly **2** are almost same to those of co-assembly **1**, while slower ET events in CS and CR were observed in co-assembly **2** compared with co-assembly **1**. This indicates that the H-bond network in co-assembly **1** could be important for the ET events in terms of the population of the faster phasic decay in co-assembly **2**. Furthermore, the increase of the *n/m* ratio enhances the population of the faster phasic decay in co-assembly **2**. Although this relation is similar to the relation observed for co-assembly **1**, the population of the faster phase in co-assembly **2** is smaller than that in co-assembly **1**. This finding suggests that co-assembly **2** is a mixture of the rigid and flexible structures which are formed by the weakened H-bond interaction relative to co-assembly **1**.

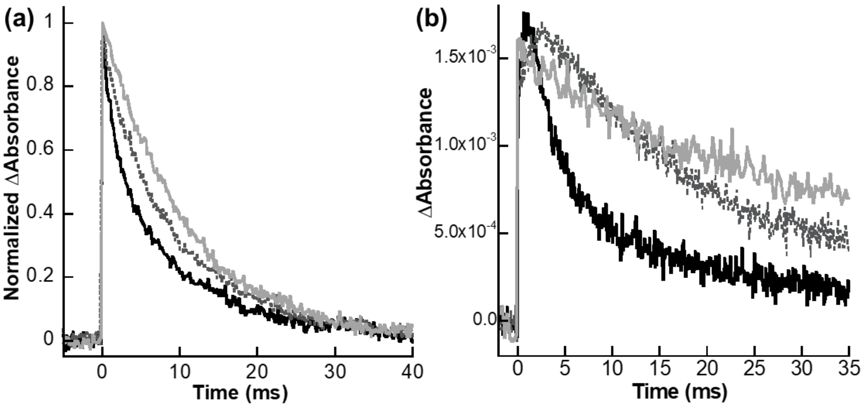

Figure 1-7. Transient absorption decays of co-assemblies (black solid line: co-assembly **1**, grey dotted line: co-assembly **2**, grey solid line: co-assembly **3**, n/m = 3/1) at (a) 460 nm and (b) 680 nm.

Table 1-2. Electron Transfer Kinetic Parameters for Co-assembly **2**[a]

n/m	$\frac{\alpha}{\alpha+\beta}$[b]	$\frac{\beta}{\alpha+\beta}$[b]	k_{CS} (s^{-1})[b]	k_{CR} (s^{-1})[c]	k_i (s^{-1})[b]
0/1[d]	—	—	—	—	86 ± 5[e]
2/1	0.17 ± 0.03	0.83 ± 0.03	300 ± 260	450 ± 130	86 ± 13
3/1	0.23 ± 0.06	0.77 ± 0.06	310 ± 70	410 ± 20	90 ± 8
average[f]	—	—	300 ± 70	430 ± 40	88 ± 3

[a]Conditions: [R98A/N80C–ZnP] = 3 μM and [R98A/N80C–FeP] = 0–9 μM in 100 mM potassium phosphate buffer, pH 7.0, at 20 °C under an N_2 atmosphere. [b]Parameters were obtained from eq 1. [c]k_{CR} was obtained from eq 3. [d]Transient decay of (R98A/N80C–ZnP)$_m$. [e]k_i was obtained from eq 2. [f]The averaged kinetic constants of co-assembly **2** were calculated using all of the experimental results.

The transient absorption decays of co-assembly **3** with the flexible structure without the interprotein H-bond were evaluated. In contrast to the results observed for the co-assemblies **1** and **2**, the decay curve of ^{3}ZnP in co-assembly **3** is fitted by the monoexponential equation to provide essentially the same kinetic constant as (N80C–ZnP)$_m$ (k_i = 89 ± 1 s^{-1}, Figure 1-7), clearly indicating that CS does not occur in the co-assembly **3**. This could be caused by the longer distance between ZnP and FeP for the ET events and/or the lack of the H-bond network in the flexible structure.

Both CS and CR in co-assembly **1** are significantly faster than in the other two co-assemblies. The major differences among these co-assemblies are the strength of the interprotein H-bond network and the related structural rigidity which should provide a shorter ZnP–FeP distance compared with a more flexible structure. Thus, these findings emphasize the importance of an interprotein H-bond interaction in providing a favorable ZnP–FeP distance and/or the pathway for ET in this system.

Evaluation of photoinduced ET in heterodimers

The ET event observed in each co-assembly includes a mixture of reactions with two possible directions as shown in Figure 1-1a. Since these properties would provide an obscure ET parameter, the exact kinetic parameters with defined directions were determined using six types of Cyt b_{562} heterodimers as shown in Figure 1-1b. The transient absorption changes of a series of heterodimers were monitored and analyzed in the same manner as co-assemblies (Figures 1-8 – 1-10). The kinetic parameters are summarized in Table 1-3. Form the kinetic results, the following three characteristics were identified: (i) the most favorable ET reactions in both CS and CR were observed in the dimer **4(Zn-Fe)** system; (ii) the kinetic parameters of the dimer

4(Fe-Zn) system clearly indicate slower ET events relative to the dimer **4(Zn-Fe)**; and (iii) the interprotein H-bond is important for ET events (this observation is consistent with the results observed in the co-assemblies).

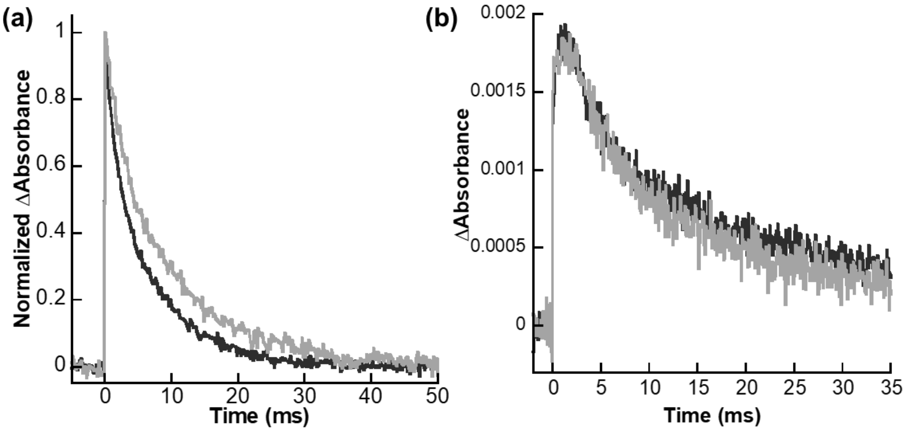

Figure 1-8. Transient absorption decays of dimers **4(Zn-Fe)** (black) and **4(Fe-Zn)** (grey) at (a) 460 nm and (b) 680 nm.

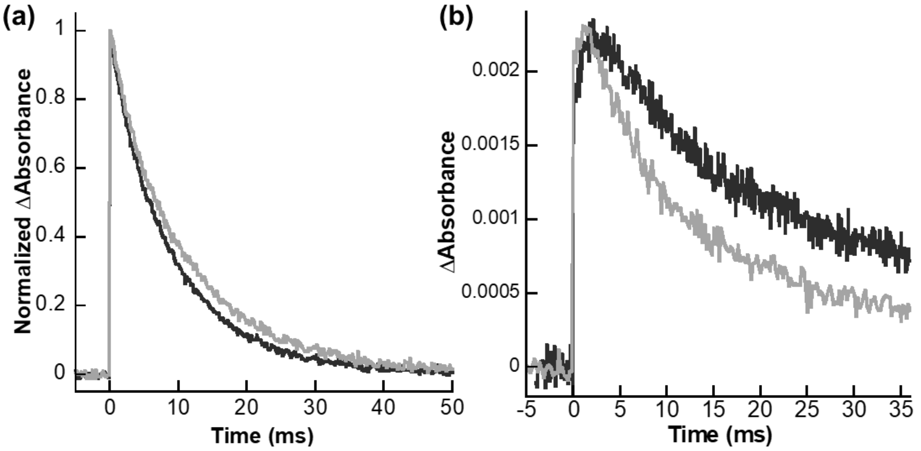

Figure 1-9. Transient absorption decays of dimers **5(Zn-Fe)** (black) and **5(Fe-Zn)** (grey) at (a) 460 nm and (b) 680 nm.

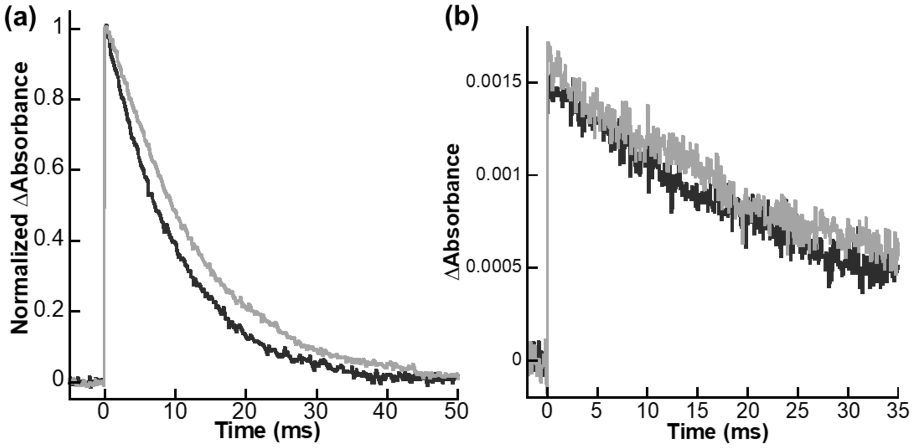

Figure 1-10. Transient absorption decays of dimers **6(Zn-Fe)** (black) and **6(Fe-Zn)** (grey) at (a) 460 nm and (b) 680 nm.

Table 1-3. Kinetic Constants of Oxidative ET of Heterodimers[a]

	k_{CS} (s^{-1})[b]	k_{CR} (s^{-1})[c]	k_i (s^{-1})[b,f]
dimer **4(Zn-Fe)**	600 ± 30	920 ± 30	120 ± 2
dimer **4(Fe-Zn)**	320 ± 40	580 ± 70	87 ± 2
dimer **5(Zn-Fe)**	370 ± 50	520 ± 20	100 ± 3
dimer **5(Fe-Zn)**	120 ± 10	180 ± 4	78 ± 1
dimer **6(Zn-Fe)**	N.D.[d]	N.D.[d]	100 ± 2[e]
dimer **6(Fe-Zn)**	N.D.[d]	N.D.[d]	80 ± 1[e]

[a] Conditions: About 3 μM of heterodimer in 100 mM potassium phosphate buffer, pH 7.0, at 20 °C under an N_2 atmosphere. [b] Parameters were obtained from eq 1. [c] k_{CR} was obtained from eq 3. [d] Not-detected. [e] k_i was obtained from eq 2. [f] These small differences of k_i values are considered to be caused by the difference of degree of solvation of ZnP or protein-conjugated ZnP in the heterodimers.[13, 14]

It is especially notable that Zn-Fe dimers mediate faster ET than the corresponding Fe-Zn dimers except for the dimers **6** which do not mediate ET. Also of interest is that the kinetic parameters depend on the ET direction, although both the Zn-Fe and the Fe-Zn dimers are expected to have similar structures. The structural differences are only derived from the position of ZnP and FeP and the chemical modification of the propionic acid of the protoporphyrin IX ligand. However, the effect of the propionic acid on the redox potential is considered to be negligible to induce this significant change.[15] Thus, the kinetic difference should be caused by the position of the FeP and ZnP.

Reductive ET in dimers 4(Fe-Zn) and 4(Zn-Fe)

The reductive ET events from the viewpoint of Marcus theory (*vide infra*) in the dimers 4 were also examined to evaluate the properties of the ET reactions. The reductive quenching of ^{3}ZnP by ferrous FeP (Fe^{2+}P) provides the ZnP radical anion (ZnP$^{\bullet-}$) as a chare separation species (Scheme 1-2).[12b,16] The driving force for this ET reaction is completely different from the oxidative ET as shown in Scheme 1. Evaluating the kinetic constants of the reductive ET give important insights into the properties of the ET reaction using Marcus theory.

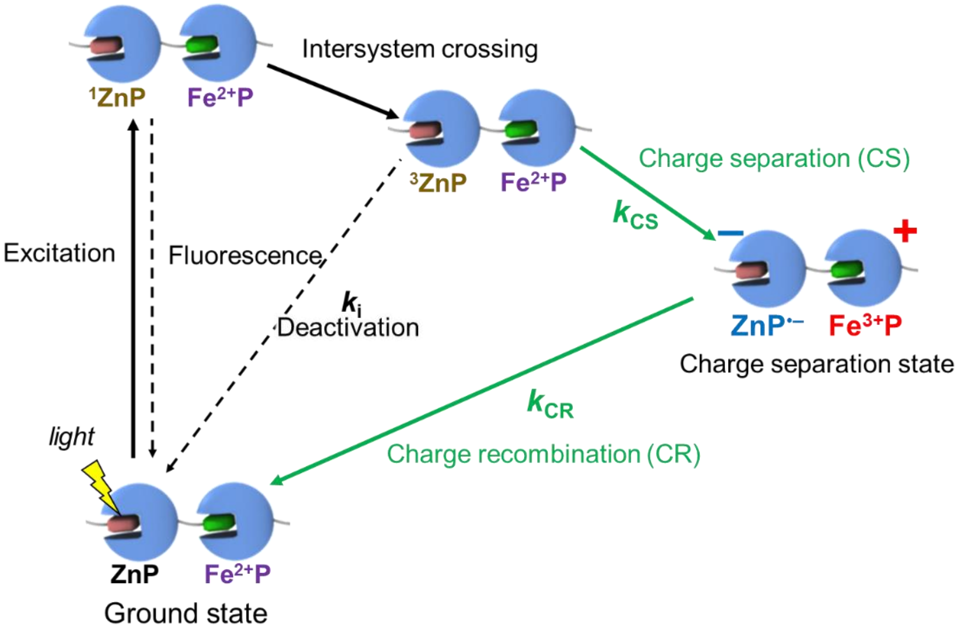

Scheme 1-2. Photochemical process of reductive ET in the co-assemblies and heterodimers

The transient absorption changes of the reduced dimers **4** were recorded after the flash photolysis. The ^{3}ZnP decays of both dimers 4(Fe-Zn) and 4(Zn-Fe) measured at 460 nm follow biexponential kinetics, indicating that the ET reaction proceeds from Fe^{2+}P to ^{3}ZnP (Figure 1-11a, Table 1-4). The CR process of the ET reactions was evaluated using the observed triexponential transient decay at 700 nm (Figure 1-11b, Table 1-4).[16] Faster CS and CR values were observed in dimer **4(Zn-Fe)** compared with dimer **4(Fe-Zn)** and this result is consistent with the oxidative ET.

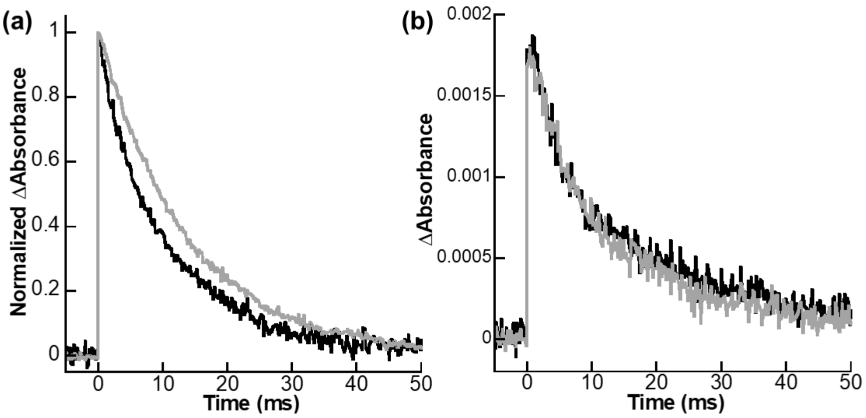

Figure 1-11. Transient absorption decays of reduced dimers **4(Zn-Fe)** (black) and **4(Fe-Zn)** (grey) at (a) 460 nm and (b) 680 nm.

Table 1-4. Reductive Electron Transfer Kinetics of Dimers **4(Zn-Fe)** and **4(Fe-Zn)**[a]

	k_{CS} (s^{-1})[b]	k_{CR} (s^{-1})[c]	k_{i} (s^{-1})[b]
dimer **4(Zn-Fe)**	140 ± 10	14 ± 8	78 ± 2
dimer **4(Fe-Zn)**	53 ± 15	5 ± 3	69 ± 2

[a] Conditions: About 3 μM of reduced heterodimers in 100 mM potassium phosphate buffer, pH 7.0, at 20 °C under an N_2 atmosphere. [b] Parameters were obtained from eq 1. [c] k_{CR} was obtained from eq 3.

Evaluation of physical properties of ET

According to Marcus theory, the kinetic constant of non-adiabatic ET is given by

$$k_{ET} = \sqrt{\frac{\pi}{h^2 \lambda k_B T}} H_{AB}^2 exp\left\{-\frac{(\Delta G^\circ + \lambda)^2}{4\lambda k_B T}\right\}$$

$$= k_0 exp\left\{-\frac{(\Delta G^\circ + \lambda)^2}{4\lambda k_B T}\right\} \qquad (4)$$

where the kinetic constant of ET (k_{ET}) depends on the driving force for ET ($-\Delta G^\circ$), the reorganization energy (λ), and the electronic coupling matrix element (H_{AB}) or k_0 which represents the kinetic constant of ET at $\Delta G^\circ = -\lambda$.[2] Applying the kinetic constants observed in the dimers **4** to eq 4 confirms whether the major factor for the kinetic difference between dimers **4(Zn-Fe)** and **4(Fe-Zn)** is derived from the electronic coupling matrix element or the reorganization energy.

Table 1-5. Driving Forces (–ΔG°) for the Oxidative and Reductive CSs and CRs for the Heterodimers

	Charge separation, $-\Delta G^{\circ}$ (eV)	Charge recombination, $-\Delta G^{\circ}$ (eV)
Oxidative ET	0.97	0.73
Reductive ET	0.33	1.37

Table 1-6. Redox Potentials of FeP in Wild-type Cyt b_{562} and ZnP in the Reconstituted Protein Which Were Used to Estimate the ΔG° Values for CS and CR.

Half-reaction	**Redox potential vs. NHE**
$ZnP^{\bullet+}/ZnP$	0.9 V[a]
$ZnP/ZnP^{\bullet-}$	-1.2V[b]
$Fe^{3+}P/Fe^{2+}P$	168 mV[c]

[a] Data was taken from ref 8b. [b] This value was estimated from the redox potential of $ZnTPP/ZnTPP^{\bullet-}$ with a pyridine-derivative ligand in ref 17. [c] Data was taken from ref 18.

Table 1-7. The Excited-State Energies for ZnP⊃WT.

	Excited-state energy (eV)
^{1}ZnP	2.08[a]
^{3}ZnP	1.70[b]

[a] Energy of S_1 band obtained from ZnP⊃WT fluorescence emission band at 596 nm. [b] Energy of T_1 band obtained from ZnP⊃WT phosphorescence emission band at 730 nm.[19]

The driving force was estimated from the redox potentials of each species which appears during the ET reaction (Tables 1-5 – 1-7). The experimental k_{ET} values for CS and CR of the dimers **4** were plotted as a function of $-\Delta G^{\circ}$ (Figure 1-12). The plots were fitted to eq 4 using a nonlinear least squares analysis, yielding the values of k_0, H_{AB}, and λ for both dimers **4(Fe-Zn)** and **4(Zn-Fe)** (Table 1-8). The reorganization energies of both dimers are similar ($\lambda \approx 0.76$ eV) while the H_{AB} and k_0 values are different. These results indicate that the difference between the ET kinetic constant of the Zn-Fe dimer and the Fe-Zn dimer is not derived from the reorganization energy but from the electronic coupling matrices of these heterodimers.

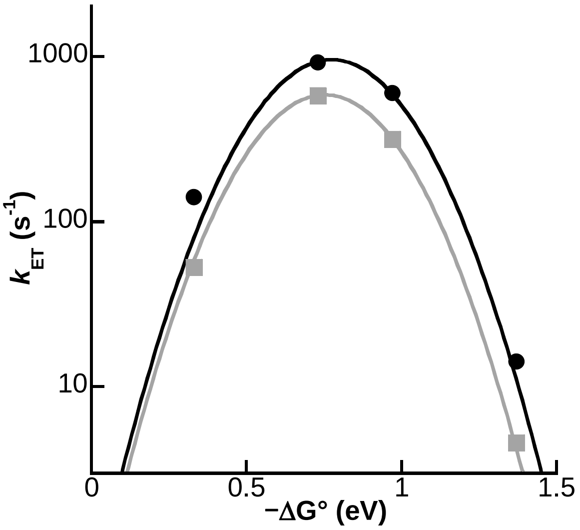

Figure 1-12. Driving-force dependence of the ET kinetics in dimers **4(Zn-Fe)** (black) and **4(Fe-Zn)** (grey).

Table 1-8. Parameters of ET Reactions of the Heterodimers Obtained from Equation 4

	k_0 (s^{-1})	H_{AB} (cm^{-1})	λ (eV)
dimer **4(Zn-Fe)**	950 ± 40	1.80×10^{-3}	0.77 ± 0.02
dimer **4(Fe-Zn)**	580 ± 4	1.40×10^{-3}	0.75 ± 0.01

Furthermore, because eq 4 from Marcus theory is based on a single-step ET, the close fitting of the ET kinetic constants to eq 4 provides evidence for the single-step ET occurring in the heterodimers. Additionally, the redox potentials of the aromatic residues in Cyt b_{562} (Tyr101, Tyr105, Phe61, and Phe65) are much higher than the redox potential of ZnP in the heterodimers (TyrOH$^{\bullet+}$/TyrOH: $E^0 \geq 1.4$ V,[20] Phe$^{\bullet+}$/Phe: $E^0 \geq 2.0$ V,[21] ZnP$^{\bullet+}$/ZnP: $E^0 \approx 0.9$ V[8b,22]) to achieve multistep electron transfer although these residues are located near the heme-binding site. Additionally, the electron hopping through TyrO$^{\bullet}$/TyrOH ($E^0 = 0.93$ V[23]) is implausible due to the lack of suitable proton acceptor nearby the Tyr residues to decrease the activation barrier of the concerted oxidation and deprotonation. Hence, it is suggested that the single-step ET occurs in the system.[24]

Structure-dependent ET pathway and the role of the interprotein H-bond network in the heterodimers

The kinetic constant of electron tunneling (k_0) generally depends on the donor–acceptor distance as equation below

$$k_0 = 10^{13} exp\{-\beta(r - r_0)\} \tag{5}$$

where r_0 is the close contact distance (r_0 = 3 Å).[2] In the previous work, the structure of the dimer of FeP⊃N80C–FeP with WT, FeP⊃N80C–FeP⊃WT was estimated from a molecular dynamics (MD) simulation and validated by AFM and CD spectroscopy measurement.[10] It is reported that the quantum calculation of ET in protein using MD-simulated donor–acceptor distance mostly reproduces the experimental results.[25] Thus, the MD-simulated heme–heme distance of FeP⊃N80C–FeP⊃WT (29 Å) was employed as the donor–acceptor distance for ET. The k_0 value calculated using this distance and the β value in the protein was determined to be less than 51 s^{-1}, which is much slower than the k_0 value obtained from transient absorption measurements of the heterodimers. Beratan *et al.* have analyzed the ET pathway in hemoproteins, especially in Cyt b_{562}.[25] It was found that two tunneling pathways are available for the ET reaction in Cyt b_{562}: one pathway crosses the edge of the heme molecule, and the other pathway includes the heme-axial ligand. The former pathway is solely dependent on the protein structure. In contrast, the latter tunneling pathway strongly depends on the protein structure and the k_{ET} value is usually different from the value predicted from the donor–acceptor distance and distance decay constant. Thus, it can be hypothesized that the rapid ET reactions in the heterodimers and co-assemblies are caused by the structure-dependent tunneling pathway.

It is known that in most cases, the ET reaction in Cyt b_{562} occurs through the distance-dependent pathway. It has been reported that the Asp73 residue is involved in the structure-dependent ET pathway.[26] The MD-optimized structure of FeP⊃N80C–FeP⊃WT indicates that the interprotein H-bond network is linked from the His102 residue (axial ligand) to the Asp73′ residue (Figure 1-13) and these two residues are related to the structure-dependent ET pathway.

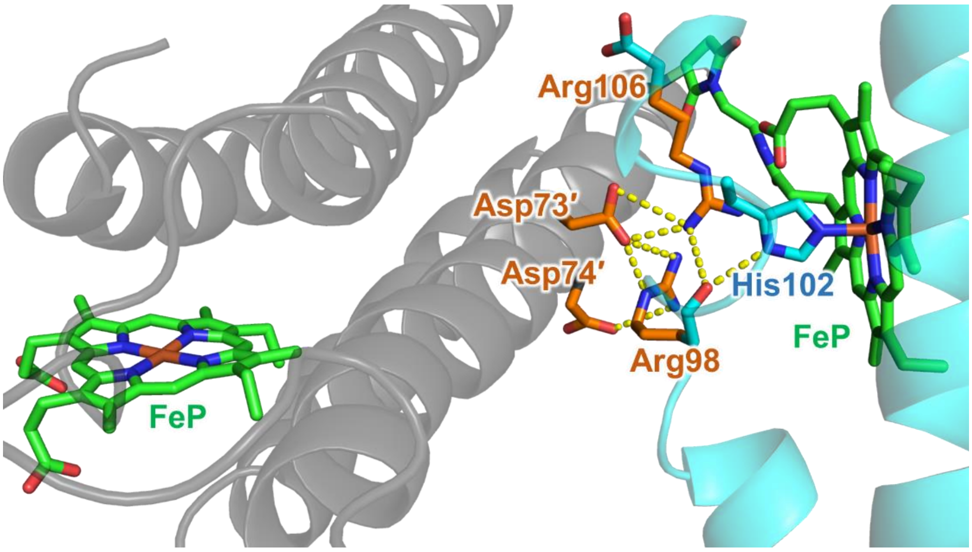

Figure 1-13. MD-optimized structure of FeP⊃N80C–FeP⊃WT. The His102 residue is linked to the carbonyl group of the Arg98 main chain by an H-bond, which is related to the H-bond network between proteins. The Asp73′ residue is also related to the structure-dependent ET pathway.

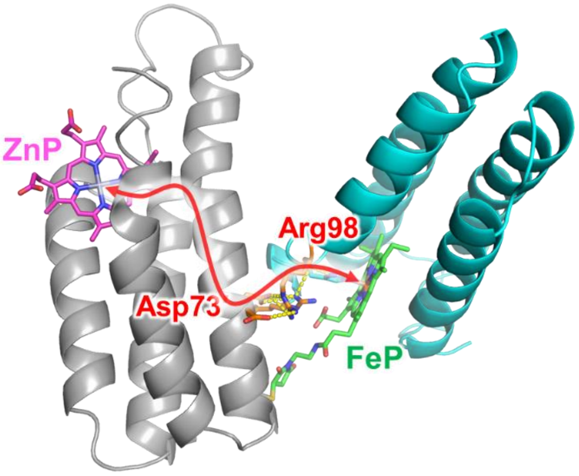

Figure 1-14. Proposed ET tunneling pathway in dimer **4(Zn-Fe)**. The red line in the model dimer structure shows the tunneling pathway.

As mentioned above, mutation of Arg98 or Asp73′ to Ala causes a significant deceleration of the ET reactions. These results provide strong evidence that the interprotein H-bond network is related to the tunneling pathway. Therefore, a plausible ET pathway in dimers **4** is shown in Figure 1-14: from donor ZnP (or FeP) to acceptor FeP (or ZnP) through the coordinating His102, the interprotein H-bond network including Arg98 and Asp73′, and Met7′. Intraprotein pathway from Asp73′ to heme moiety via the coordinating Met7′ is reported by Beratan *et al.*[26] Support for this hypothesis is provided by observations of ET reactions in the flexible or semi-rigid co-assemblies and heterodimers where H-bonds were eliminated. In this case, the ET pathway between protein matrices will be weakened or disappeared by the mutation of residues contributing to the interprotein H-bond interaction, resulting in the weak or extinct electron coupling. Furthermore, the structure of the protein matrix in the MD-optimized dimers is slightly distorted compared to the wild-type Cyt b_{562} monomer (WT: RMSD = 1.64 Å, N80C: RMSD = 1.47 Å). Hence, it is possible that these structural changes induce the rapid ET reaction.

It is also possible that the change of rigidity affects the kinetics of ET. Even in this case, the interprotein H-bond network, which affects the rigidity of co-assemblies and heterodimers, is considered as the plausible ET pathway to achieve this long-range ET in co-assemblies and heterodimers. This is because that only the interprotein H-bond network can surves the structure-dependent ET pathway, which is essential to conduct faster ET than predicted from ET distance. Therefore, it is considered that the rigidity itself does not have significant effect on the kinetics of ET, but the change of the strength and distance of H-bond network affects the kinetics of ET significantly.

The reason for the different ET kinetics between Zn-Fe and Fe-Zn dimers is rationalized by this plausible ET pathway. It is known that substitution of heme with other metalloporphyrins such as Zn porphyrin provides partial structural changes.[27] Especially, the Zn porphyrin substitution will elongate the distance between the metal center in porphyrin and the S atom of the axial Met ligand, which is experimentally observed in cytochrome *c*. The tunneling pathway in the heterodimers and co-assembly could be very sensitive to structural changes occurring in the proteins. Especially, the axial Met ligand in heterodimer is a part of plausible ET pathway. Therefore, the slightly deviated positioning of the cofactor and residues will affect the ET kinetics in the Zn-Fe and Fe-Zn dimers.

1-3. Summary

The author demonstrates long-range ET reactions in Cyt b_{562} N80C mutant-based co-assemblies and heterodimers containing Fe and Zn porphyrin. Although the plausible donor–acceptor distance (29 Å) in structurally-defined heterodimers and co-assemblies is generally quite long with respect to single-step ET in proteins, the experimental kinetic constants of the ET in the present systems are much larger than the predicted k_0 value from the donor–acceptor distance and the reported protein distance decay constant (β). Taken together with the finding that the interprotein H-bond network connected to the axial ligand residue of FeP and ZnP is essential for rapid long-range ET, it is hypothesized that the single-step ET reaction occurs via a structure-dependent tunneling pathway. This plausible ET pathway is also supported by the larger kinetic constants of the Zn-Fe dimer relative to those of the Fe-Zn dimer, which have slight structural differences. However, the discussion of the precise pathway should be considered after performing quantum-mechanics level calculations which would provide additional information of the effect of protein structure and residues.[28] These findings will give us the new insight not only into the modulation of donor–acceptor distance[2] or reorganization energy of protein[29] but also into the fine-tuning of the protein structure and electron transfer pathway which are effective to control the ET kinetics in hemoprotein. Although the fine-tuning of these factors requires distinct computational simulation, this strategy will be an effective tool to design an artificial system to replicate the efficient ET in photosynthetic proteins.

1-4. Experimental Section

Materials and methods

ESI-TOF MS analyses were performed with a Bruker Daltonics micrOTOF II mass spectrometer. UV-vis spectra were measured with a Shimadzu UV-3150 or UV-2550 double-beam spectrometer or JASCO V-670 spectrophotometer. Circular dichroism (CD) spectrum was recorded with a JASCO J-820S spectrometer. Luminescence spectra were measured with a JASCO FP-8600 fluorescence spectrometer. Size exclusion chromatographic (SEC) analyses were performed using an ÄKTApurifier system (GE Healthcare) at 4 °C. The pH measurements were carried out with an F-52 Horiba pH meter. Air-sensitive manipulations were performed in a UNILab glove box (MBraun, Germany). The equipment used for flash photolysis experiments is described below.

Iron and zinc protoporphyrin IX complexes (FeP, ZnP) with a maleimide group provided at one of the propionate side chains via a linker molecule (m–FeP, m–ZnP) were prepared according to previous reports.[24] ZnP was synthesized using a conventional procedure.[25] FeP and other reagents and chemicals were purchased and used as received. Cytochrome b_{562} (Cyt b_{562}) and its mutants were expressed in the TG1 strain of *E. coli* and purified as previously reported.[26] Apo-forms of the proteins (wild-type Cyt b_{562} (WT), N80C, R98A, and D73A/N80C) were prepared by Teale's conventional 2-butanone method.[27]

Preparation of Cyt *b*$_{562}$ assemblies containing ZnP

The synthesized maleimide-linked Zn porphyrin, m–ZnP, (1 mg) in a DMF solution (400 μL) was added to 222 μM of reduced N80C Cyt *b*$_{562}$ in 50 mM Tris-HCl buffer (pH 8.0, 1.5 mL). The mixture was then gently stirred at room temperature for 4 h under an N_2 atmosphere. Then, a mixture of 4 M guanidine-HCl and 200 mM histidine-HCl in 50 mM Tris-HCl buffer (pH 7.3, 2 mL) was added to the protein solution for denaturation. The native heme and unreacted m–ZnP cofactors were removed from the aqueous phase by performing a 2-butanone extraction five times. The solution was dialyzed against 1 L of 100 mM potassium phosphate buffer (pH 7.0). The obtained assembly, (N80C–ZnP)$_m$, was then concentrated using an Amicon Ultra (Merck Millipore) concentrator and stored at –80 °C. The obtained protein units were characterized by ESI-TOF MS and UV-vis spectroscopic measurements. Other assemblies, (R98A/N80C–ZnP)$_m$ and (D73A/N80C–ZnP)$_m$ were prepared according to the same procedure used for preparation of (N80C–ZnP)$_m$ and characterized by ESI-TOF MS: N80C–ZnP (*m/z* calcd: 1044.1 (z = 12+), found: 1044.08), R98A/N80C–ZnP (*m/z* calcd: 1037.02 (z = 12+), found: 1036.98), D73A/N80C–ZnP (*m/z* calcd: 1040.44 (z = 12+), found: 1040.30).

Preparation of cytochrome *b*$_{562}$ co-assemblies

The N80C Cyt *b*$_{562}$ co-assembly containing FeP and ZnP (co-assembly **1**, (N80C–FeP)$_n$–(N80C–ZnP)$_m$) was prepared by mixing the (N80C–FeP)$_n$ and (N80C–ZnP)$_m$ assembly (*n/m* = 1/1, 2/1, 3/1, [N80C–ZnP] = 3 μM) and allowing it to equilibrate for more than 10 hours under an N_2 atmosphere. The equilibration was confirmed by size exclusion chromatography using Superdex 200 10/300 GL (GE Healthcare). Other co-assemblies, co-assembly **2** and co-assembly **3**, were prepared according to the same procedures used to prepare co-assembly **1**.

Preparation of cytochrome *b*$_{562}$ Fe-Zn heterodimers

Reconstituted wild-type Cyt *b*$_{562}$ with maleimide-linked ZnP (m–ZnP⊃WT, 50 nmol) and N80C Cyt *b*$_{562}$ (FeP⊃N80C, 150 nmol) were added to 4 mL of 100 mM phosphate buffer solution (pH 8.0). The mixture was stirred for 1 h at 4 °C. After the reaction, 2 mg of dithiothreitol (DTT) was added and the reaction mixture was purified by gel filtration chromatography using a Superdex 200 Increase 10/300 GL column (GE Healthcare). The obtained dimeric protein, dimer **4(Fe-Zn)**, FeP⊃N80C–ZnP⊃WT, was oxidized by potassium ferricyanide or reduced by DTT and purified again using a HiTrap desalting column (GE

Healthcare). The same procedure was used to prepare and characterize dimer **5(Fe-Zn)** and dimer **6(Fe-Zn)**.

Preparation of cytochrome b_{562} Zn-Fe heterodimers

Reconstituted wild-type Cyt b_{562} with maleimide-linked FeP (m–FeP⊃WT, 50 nmol) and reconstituted N80C Cyt b_{562} with ZnP (ZnP⊃N80C, 150 nmol) were added to 4 mL of 100 mM phosphate buffer solution (pH 8.0). The mixture was stirred for 1 h at 4 °C. After the reaction, 2 mg of DTT was added and the reaction mixture was purified by gel filtration chromatography using a Superdex 200 Increase 10/300 GL column (GE Healthcare). The obtained dimeric protein, dimer **4(Zn-Fe)**, ZnP⊃N80C–FeP⊃WT, was oxidized by potassium ferricyanide or reduced by DTT and purified again using a HiTrap desalting column (GE Healthcare). The same procedures were used to prepare and characterize dimer **5(Zn-Fe)** and dimer **6(Zn-Fe)**.

Kinetic analysis

The ET kinetic parameters from transient absorption changes were determined as described below. To simplify the kinetic model, we omitted the nanosecond dynamics such as direct deactivation of the singlet state (S_1) by fluorescence and intersystem crossing (~ 1 ns). The kinetics scheme is shown in Scheme 1-3a. Here, A and B correspond to a triplet species (T_1) of ET-active ZnP and a CS species, respectively.

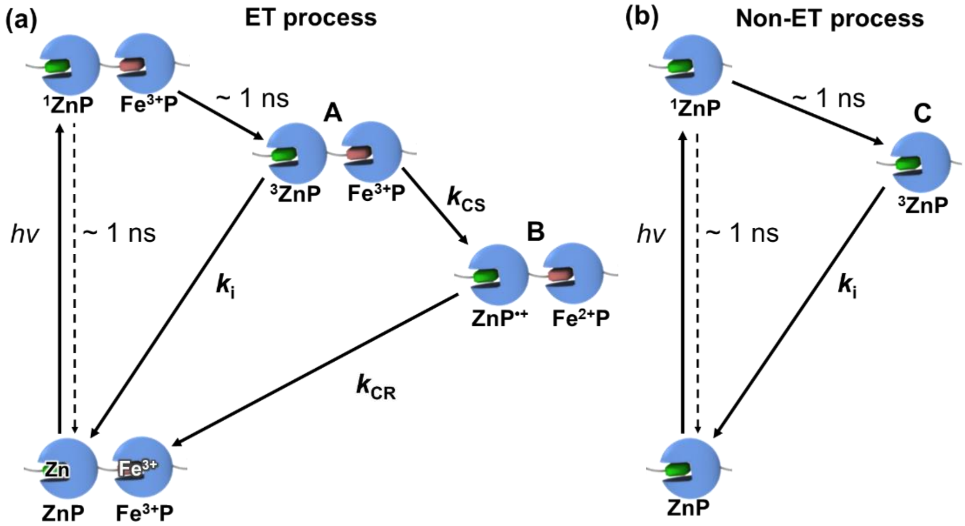

Scheme 1-3. (a) Kinetic model of the charge separation (CS) and charge recombination (CR) processes by an ET-active ZnP species in Cyt b_{562} co-assemblies or heterodimers. The CS process provides CS species (B) from T_1 species (A), then the CS species (B) returns to the ground state. (b) Kinetic model of the photochemical reaction in an ET-inactive ZnP species within co-assemblies and heterodimers. The T_1 species (C) is only deactivated to the ground state.

The differential equations describing the ET processes are shown in eqs 6 and 7.

$$\frac{d[A]}{dt} = -(k_{CS} + k_i)[A] \tag{6}$$

$$\frac{d[B]}{dt} = k_{CS}[A] - k_{CR}[B] \tag{7}$$

[A] and [B] are the concentrations of A and B, respectively.

The concentration of B at $t = 0$ is zero:

$$[B]_0 = 0 \tag{8}$$

Therefore, the time-dependent concentration changes of A and B are represented as:

$$[A] = [A]_0 e^{-k_a t} \tag{9}$$

$$[B] = \frac{k_{CS}}{k_{CR} - k_a}[A]_0(e^{-k_a t} - e^{-k_{CR} t}) \tag{10}$$

$$k_a = k_{CS} + k_i \tag{11}$$

In this system, some fractions of ZnP in co-assemblies and heterodimers do not contribute to the ET reactions due to the presence of the repeating sequence of the ZnP-modified proteins in co-assemblies and the structurally-undefined assembling units in H-bond eliminated co-assemblies and heterodimers. The photochemical reaction of these fractions is shown in Scheme 1-3b and C is defined as a T_1 species of ET-inactive ZnP. The differential equation of the non-ET process (eq 12) leads to the time-dependent concentration changes of C as shown in eq 13.

$$\frac{d[C]}{dt} = -k_i[C] \tag{12}$$

$$[C] = [C]_0 e^{-k_i t} \tag{13}$$

The T_1 species (^{3}ZnP) has a specific absorption band at 460 nm. When the extinction coefficient of the T_1 species at 460 nm is defined as ε_1, the transient absorption at 460 nm is represented by eq 14.

$$\Delta\text{Abs} = \varepsilon_1([A] + [C]) = \varepsilon_1([A]_0 e^{-k_a t} + [C]_0 e^{-k_i t}) \tag{14}$$

Therefore, the transient absorption at 460 nm can be fitted by eq 1.

$$\Delta\text{Abs} = \alpha e^{-k_a t} + \beta e^{-k_i t} \tag{1}$$

In the case of the charge separation state, the CS species (ZnP$^{\bullet+}$ and ZnP$^{\bullet-}$) has the absorption band at ~690 nm (680 nm and 700 nm, respectively). However, the T_1 species also has an absorption in the vicinity of this wavelength, and the transient absorption of this region is the sum of A, B and C. When the extinction coefficient of T_1 and the charge separation species at ~690 nm are defined as ε_2 and ε_3 respectively, the transient absorption are represented by eq 15.

$$\Delta\text{Abs} = \varepsilon_2[A]_0 e^{-k_a t} + \frac{k_{CS}}{k_{CR} - k_a}\varepsilon_3[A]_0(e^{-k_a t} - e^{-k_{CR} t}) + \varepsilon_2[C]_0 e^{-k_i t}$$

$$= \left[\varepsilon_2 + \frac{k_{CS}}{k_{CR} - k_a}\varepsilon_3\right][A]_0 e^{-k_a t} - \frac{k_{CS}}{k_{CR} - k_a}\varepsilon_3 [A]_0 e^{-k_{CR} t} + \varepsilon_2 [C]_0 e^{-k_i t} \tag{15}$$

Assuming that $k_{\mathrm{CR}} > k_{\mathrm{a}}$, the second term of eq 15 is a negative value. Thus, the fitting equation is:

$$\Delta\mathrm{Abs} = \alpha' e^{-k_a t} - \beta' e^{-k_{CR} t} + \gamma' e^{-k_i t} \tag{16a}$$

In contrast, assuming that $k_{\mathrm{a}} > k_{\mathrm{CR}} > k_{\mathrm{a}} - (\varepsilon_3/\varepsilon_2)k_{\mathrm{CS}}$, the first term of eq 15 is a negative value, and therefore,

$$\Delta\mathrm{Abs} = -\alpha' e^{-k_a t} + \beta' e^{-k_{CR} t} + \gamma' e^{-k_i t} \tag{16b}$$

Furthermore, in the case of $k_{\mathrm{a}} - (\varepsilon_3/\varepsilon_2)k_{\mathrm{CS}} > k_{\mathrm{CR}}$,

$$\Delta\mathrm{Abs} = \alpha' e^{-k_a t} + \beta' e^{-k_{CR} t} + \gamma' e^{-k_i t} \tag{16c}$$

Laser flash photolysis

The nanosecond laser flash photolysis studies were carried out using a Q-switched Nd:YAG laser, which delivers 6-ns pulses at 532 nm. The probe source was a continuous 150-W Xenon arc lamp passed through a monochromator. The protein co-assembly solutions (3–12 μM) in degassed 100 mM phosphate buffer (pH 7.0) were prepared in a glovebox in a 10-mm quartz cell. The protein dimer solutions (~ 3 μM) in degassed 100 mM potassium phosphate buffer (pH 7.0) were also prepared in the glovebox in the 10-mm quartz cell. The temperature was maintained at 20 °C during the laser irradiation. The transient absorption changes for the ZnP triplet excited states in the protein assemblies and heterodimers (^{3}ZnP) were monitored at 460 nm. The transient absorption changes for the ZnP radical cation (ZnP$^{\bullet+}$) and radical anion (ZnP$^{\bullet-}$) in the protein assemblies and heterodimers were monitored at 680 nm and 700 nm, respectively. Signals were detected in transmission using a photomultiplier (Unisoku), and the transient signals were digitized using a Tektronix TDS3012 oscilloscope. Signals were averaged from 128-3072 repeated measurements. The data were collected in the 0–100 ms range, and then, transferred to a computer for further data analysis. UV-vis spectra of the protein solutions were measured before and after flash photolysis studies to confirm that the sample remained resistant to significant photodegradation.

The obtained transient absorption decay data were fitted using KaleidaGraph (Version 4.00, Synergy Software). The transient absorption changes of ^{3}ZnP (460 nm) in Cyt b_{562} co-assemblies and heterodimers can be represented by eq 1, whereas the ^{3}ZnP decay in non-ET protein oligomers can be fitted using eq 2,

where k_{i} is the kinetic constant of ^{3}ZnP deactivation without ET, and k_{a} is the sum of the kinetic constant of charge separation (CS: k_{CS}) and k_{i}.

The transient absorption decay of $ZnP^{\bullet +}$ (680 nm) and $ZnP^{\bullet -}$ (700 nm) can be analyzed by eq 3,

where k_{CR} is the kinetic constant of charge recombination (CR). When k_{CR} is higher than k_a, a_2 has a negative value. On the other hand, assuming that k_a is almost equal to or slightly higher than k_{CR}, a_1 becomes negative (See SI).

Driving force of the ET reaction

The driving force ($-\Delta G°$) of both the oxidative and reductive ET reactions can be calculated from the difference of the redox potential in each chemical species (Table 1-6) and the energy of the excited states of ZnP, relative to the ground state. The ^{1}ZnP and ^{3}ZnP energies were obtained by the fluorescence and phosphorescence of reconstituted wild-type Cyt b_{562} with ZnP (ZnP⊃WT, Figure 1-15, Table 1-7).

The fluorescence spectrum of ZnP⊃WT shows two major emission bands, S(0,0) and S(0,1). The S_1 energy can be determined from the emission energy of S(0,0) band (2.1 eV). Meanwhile, the phosphorescence measurement of ZnP⊃WT exhibits an additional emission band with fluorescence emission bands. The additional emission peak near 730 nm is derived from the T(0,0) band (1.7 eV).[19]

1-5. References and Notes

(1) Croce, R.; van Amerongen, H. *Nat. Chem. Biol.* **2014**, *10*, 492–501.

(2) Gray, H. B.; Winkler, J. R. *Q. Rev. Biophys.* **2003**, *36*, 341–372.

(3) Winkler, J. R.; Gray, H. B. *Chem. Rev.* **2014**, *114*, 3369–3380.

(4) (a) Wikström, M.; Sharma, V.; Kaila, V. R. I.; Hosler, J. P.; Hummer, G. *Chem. Rev.,* **2015**, *115*, 2196–2221. (b) Yoshikawa, S.; Shimada, A. *Chem. Rev.* **2015**, *115*, 1936–1989.

(5) (a) Shih, C.; Museth, A. K.; Abrahamsson, M.; Blanco-Rodriguez, A. M.; Di Bilio, A. J.; Sudhamsu, J.; Crane, B. R.; Ronayne, K. L.; Towrie, M.; Vlček, A., Jr.; Richards, J. H.; Winkler, J. R.; Gray, H. B. *Science.* **2008**, *320*, 1760–1762. (b) Takematsu, K.; Williamson, H.; Blanco-Rodríguez, A. M.; Sokolova, L.; Nikolovski, P.; Kaiser, J. T.; Towrie, M.; Clark, I. P.; Vlček, A., Jr.; Winkler, J. R.; Gray, H. B. *J. Am. Chem. Soc.* **2013**, *135*, 15515–15525. (c) Bogdanov, A. M.; Acharya, A.; Titelmayer, A. V.; Mamontova, A. V.; Bravaya, K. B.; Kolomeisky, A. B.; Lukyanov, K. A.; Krylov, A. I. *J. Am. Chem. Soc.* **2016**, *138*, 4807–4817. (d) Crane, B. R.; Di Bilio, A. J.; Winkler, J. R.; Gray, H. B. *J. Am. Chem. Soc.* **2001**, *123*, 11623–11631.

(6) Renger, G.; Renger, T. *Photosynth. Res.* **2008**, *98*, 53–80.

(7) (a) Gray, H. B.; Winkler, J. R. *Proc. Natl. Acad. Sci. U. S. A.* **2005**, *102*, 3534–3539. (b) Winkler, J. R.; Gray, H. B. *J. Am. Chem. Soc.* **2014**, *136*, 2930–2939.

(8) (a) Hayashi, T.; Hitomi, Y.; Ogoshi, H. *J. Am. Chem. Soc.* **1998**, *120*, 4910–4915. (b) Hitomi, Y.; Hayashi, T.; Wada, K.; Mizutani, T.; Hisaeda, Y.; Ogoshi, H. *Angew. Chem. Int. Ed.* **2001**, *40*, 1098–1101. (c) Tezcan, F. A.; Crane, B. R.; Winkler, J. R.; Gray, H. B. *Proc. Natl. Acad. Sci. U. S. A.* **2001**, *98*, 5002–5006. (d) Xiong, P.; Nocek, J. M.; Vura-Weis, J.; Lockard, J. V; Wasielewski, M. R.; Hoffman, B. M. *Science.* **2011**, *330*, 1075–1078.

(9) (a) Luo, Q.; Hou, C.; Bai, Y.; Wang, R.; Liu, J. *Chem. Rev.* **2016**, *116*, 13571–13632. (b) Bai, Y.; Luo, Q.; Liu, J. *Chem. Soc. Rev.* **2016**, *45*, 2756–2767.

(10) Oohora, K.; Fujimaki, N.; Kajihara, R.; Watanabe, H.; Uchihashi, T.; Hayashi, T. *J. Am. Chem. Soc.* **2018**, *140*, 10145–10148.

(11) (a) Sukegawa, J.; Schubert, C.; Zhu, X.; Tsuji, H.; Guldi, D. M.; Nakamura, E. *Nat. Chem.* **2014**, *6*, 899–905. (b) Pettersson, K.; Kilså, K.; Mårtensson, J.; Albinsson, B. *J. Am. Chem. Soc.* **2004**, *126*, 6710–6719. (c) Göransson, E.; Boixel, J.; Monnereau, C.; Blart, E.; Pellegrin, Y.; Becker, H.; Hammarström, L.; Odobel, F. *Inorg. Chem.* **2010**, *49*, 9823–9832. (d) Imahori, H.; Guldi, D. M.; Tamaki, K.; Yoshida, Y.; Luo, C.; Sakata, Y.; Fukuzumi, S. *J. Am. Chem. Soc.* **2001**, *123*, 6617–6628. (e) Bell, T. D. M.; Ghiggino, K. P.; Jolliffe, K. A.; Ranasinghe, M. G.; Langford, S. J.; Shephard, M. J.; Paddon-Row, M. N. *J. Phys. Chem. A* **2002**, *106*, 10079–10088.

(12) (a) Kang, S. A.; Marjavaara, P. J.; Crane, B. R. *J. Am. Chem. Soc.* **2004**, *126*, 10836–10837. (b) Co, N. P.; Young, R. M.; Smeigh, A. L.; Wasielewski, M. R.; Hoffman, B. M. *J. Am. Chem. Soc.* **2014**, *136*,

12730–12736. (c) McGourty, J. L.; Blough, N. V; Hoffman, B. M. *J. Am. Chem. Soc.* **1983**, *105*, 4470–4472. (d) Koshiyama, T.; Shirai, M.; Hikage, T.; Tabe, H.; Tanaka, K.; Kitagawa, S.; Ueno, T. *Angew. Chem. Int. Ed.* **2011**, *50*, 4849–4852

(13) Kim, J. E.; Pribisko, M. A.; Gray, H. B.; Winkler, J. R. *Inorg. Chem.* **2004**, *43*, 7953–7960.

(14) The calculated solvation area of FeP and FeP with the linker in Cyt b_{562} dimer are 154 Å^2 and 132 Å^2, respectively. The redox potential of FeP without linker (dimer **4(Fe-Zn)**) is considered to be same with FeP in wild-type Cyt b_{562}. Although the redox potential of FeP with the linker (dimer **4(Zn-Fe)**) is plausibly changed due to the smaller solvation than FeP, this change will provide small positive shift.[30] Assuming that the redox potential change would be +50 mV, the k_0 value of dimer **4(Zn-Fe)** obtained from eq 4 would be $(1.09 \pm 0.07) \times 10^3$ s^{-1}, which is slightly larger than the case of no redox potantial change (Table 6). Since the k_0 value is still larger than that observed in dimer **4(Fe-Zn)**, the small positive shift of the FeP redox potential is not significant.

(15) Harada, K.; Makino, M.; Sugimoto, H.; Hirota, S.; Matsuo, T.; Shiro, Y.; Hisaeda, Y.; Hayashi, T. *Biochemistry* **2007**, *46*, 9406–9416.

(16) Shen, C.; Kostić, N. M. *Inorg. Chem.* **1996**, *35*, 2780–2784.

(17) Kadish, K. M.; Shiue, L. R.; Rhodes, R. K.; Bottomley, L. A. *Inorg. Chem.* **1981**, *20*, 1274–1277.

(18) Liu, J.; Chakraborty, S.; Hosseinzadeh, P.; Yu, Y.; Tian, S.; Petrik, I.; Bhagi, A.; Lu, Y. *Chem. Rev.* **2014**, *114*, 4366–4469.

(19) (a) Balzani, V.; Ceroni, P.; Juris, A. *Photochemistry and Photophysics: Concepts, Research, Applications;* Wiley-VCH: Weinheim, 2014; pp68–90. (b) Cowan, J. A.; Gray, H. B. *Inorg. Chem.*, **1989**, *28*, 4554–4556.

(20) Warren, J. J.; Winkler, J. R.; Gray, H. B. *FEBS Lett.* **2012**, *586*, 596–602.

(21) Merkel, P. B.; Luo, P.; Dinnocenzo, J. P.; Farid, S. *J. Org. Chem.* **2009**, *74*, 5163–5173.

(22) It is known that the redox potential of Zn porphyrin is not markedly affected by the protein matrix.[16] Therefore, we have applied the redox potential of Zn porphyrin in Cyt *c* as the redox of Zn porphyrin in Cyt b_{562} because the structures including the coordinating amino acid residues are similar.

(23) Dempsey, J. L.; Winkler, J. R. Gray, H. B. *Chem. Rev*. **2010**, *110*, 7024–7039.

(24) The electron hopping via oxidation of TyrO$^-$ (TyrO$^\bullet$/TyrO$^-$: $E^0 = 0.71$ V[20]) is thermodynamically favorable. However, the pK_a of TyrOH (pK_a = 10.1) is too high to form tyrosinate *in situ*. Thus, this hopping seems to be impossible.

(25) Prytkova, T. R.; Shunaev, V. V.; Glukhova, O. E.; Kurnikov, I. V. *J. Phys. Chem. B* **2015**, *119*, 1288–1294.

(26) Prytkova, T. R.; Kurnikov, I. V.; Beratan, D. N. *Science.* **2007**, *315*, 622–625.

(27) Qian, C.; Yao, Y.; Tong, Y.; Wang, J.; Tang, W. *J. Biol. Inorg. Chem.* **2003**, *8*, 394–400.

(28) (a) Monni, R.; Haddad, A. A.; van Mourik, F.; Auböck, G.; Chergui, M. *Proc. Natl. Acad. Sci. U. S. A.* **2015**, *112*, 5602–5606. (b) Suess, C. J.; Hirst, J. D.; Besley, N. A. *J. Comput. Chem.* **2017**, *38*, 1495–1502.

(29) Farver, O.; Marshall, N. M.; Wherland, S.; Lu, Y.; Pecht, I.; *Proc. Natl. Acad. Sci. U. S. A.* **2013**, *110*, 10536–10540.

(30) Tezcan, F. A.; Winkler, J. R.; Gray, H. B. Effects of Ligation and Folding on Reduction Potentials of Heme Proteins. *J. Am. Chem. Soc.*, **1998**, *120*, 13383–13388.

(31) (a) Kitagishi, H.; Kakikura, Y.; Yamaguchi, H.; Oohora, K.; Harada, A.; Hayashi, T. *Angew. Chem. Int. Ed.* **2009**, *48*, 1271–1274.(b) Onoda, A.; Kakikura, Y.; Uematsu, T.; Kuwabata, S.; Hayashi, T. *Angew. Chem. Int. Ed.* **2012**, *51*, 2628–2631.

(32) Oohora, K.; Mashima, T.; Ohkubo, K.; Fukuzumi, S.; Hayashi, T. *Chem. Commun.* **2015**, *51*, 11138–11140.

(33) Kitagishi, H.; Oohora, K.; Yamaguchi, H.; Sato, H.; Matsuo, T.; Harada, A.; Hayashi, T. *J. Am. Chem. Soc.* **2007**, *129*, 10326–10327.

(34) Teale, F. W. J. *Biochim. Biophys. Acta.* **1959**, *35*, 543.

Chapter 2

Multivalent effect of arginine residues for cellular uptake of cytochrome b_{562} assembly

2-1. Introduction

Artificially-constructed protein assembling systems are promising materials for biological application.[1] Over the last decade, great efforts of chemists and biologists have demonstrated several approaches for preparing the protein assemblies using biological and/or chemical strategies. Various structures and sizes of protein assemblies are now available. Nevertheless, applications of these artificial protein assemblies have still been under investigation. Several researchers reported the utilization of the artificial protein assemblies toward light harvesting systems,[2] artificial enzymes,[3] biomedical therapeutic materials,[4] and so on.

Especially, it is expected to apply protein assemblies to biomedical fields such as drug delivery due to their general biocompatibility and sub-micrometer size range.[5] In the case of natural protein assemblies, the cage-like protein assemblies such as viral-like particles and ferritin are attractive nanocarrier to deliver the drug molecules which are attached covalently or encapsulated inside the cavity. It is known that these cage protein assemblies often have high cellular uptake ability. Thus, various groups have been reported to employ these natural protein cages to deliver their cargo molecules into the cell.[6,7] While the various biomedical applications of natural protein assemblies are widely studied, application of artificial protein assemblies to the biomedical fields are still limited to date. Some researchers reported the application of the artificial protein assemblies to the drug delivery system.[8] However, artificial protein assemblies are usually designed without considering the cellular uptake ability. Therefore, it is necessary to increase the cellular uptake ability of protein assemblies in order to apply them to the drug delivery system.

In this context, the author has focused on the oligoarginine (Rn) tag, one of the cell-penetrating peptide, in order to deliver the artificial protein assemblies inside the cells.[9] It is known that a sequential alignment of Arg residues, can induce cell penetration. It is also known that an octaarginine (R8) tag acts as a modest cell penetrating peptide among the Rn tag to deliver various types of cargo into cells. The cellular uptake ability of the Rn tag is derived from the cluster effect of Arg residues concentration. Thus, it is revealed that the branched-chain R8 tag can also have high cellular uptake ability.[9b]

From these characteristics, the author proposed that an Arg cluster formed in an artificial protein assembly would allow constructing a unique system for cellular uptake.[10] While a protein monomer with a small Rn tag would not be taken up by cells, an assembly of the protein units would provide the Arg cluster for the cell penetration. In this study, the author investigated the cellular uptake of both N80C mutant-based rigid and flexible Cyt b_{562} assemblies[11] with Rn tags where the diarginine (R2) or tetraarginine (R4) tag is attached onto each protein surface. The R2 and R4 tags generally do not provide the ability to penetrate cells. It was believed that the rigid assembly would be efficiently penetrated into the cells due to a multivalent interaction between Arg residues and the cell surface. The multivalent effect provided by pre-organized Arg residues displayed on the same sides of the linear assembly is schematically shown in Figure 2-1.

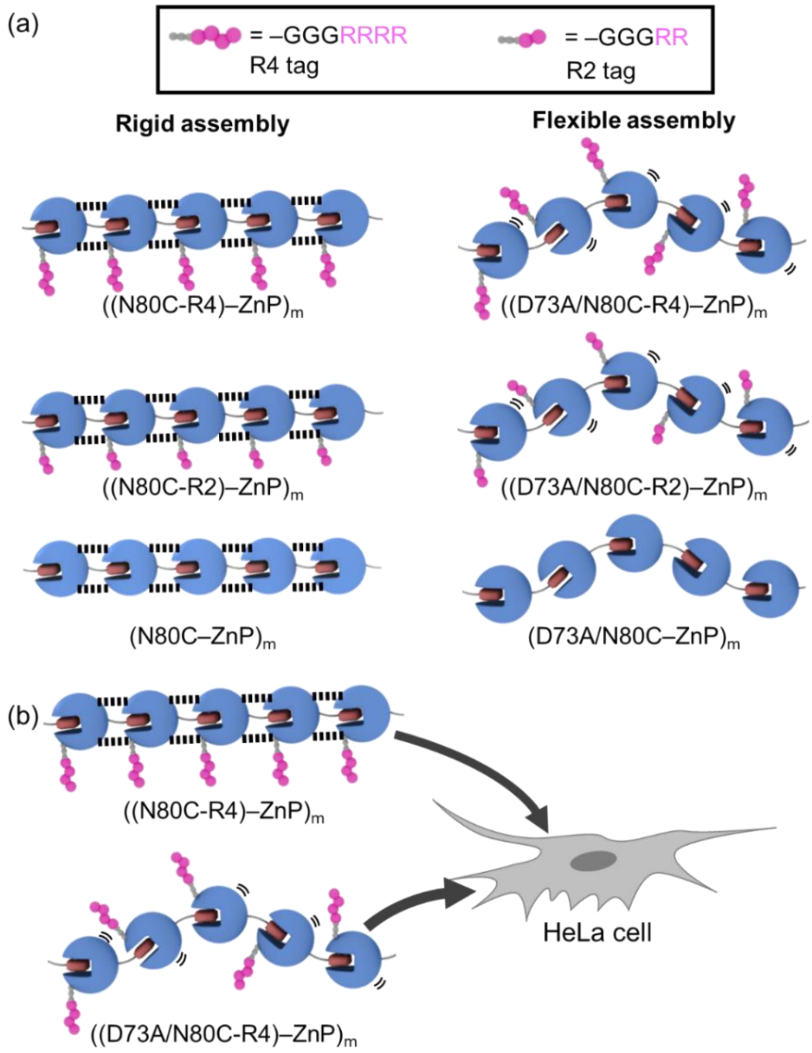

Figure 2-1. Schematic representations of (a) the rigid/flexible Cyt b_{562} assemblies and (b) cellular uptake of Cyt b_{562} assemblies to the HeLa cells.

2-2. Results and Discussion

Preparation of Rn tag attached Cyt b_{562} assemblies

The R4 and R2 tags were fused genetically to the C-terminal of the N80C Cyt b_{562} via glycine trimers as a linker to obtain N80C-R4 and N80C-R2 respectively. The preparation of Cyt b_{562} assemblies is achieved using m–ZnP instead of m–FeP in order to utilize the fluorescence of ZnP as the probe for monitoring the cellular uptake events. The reaction of m–ZnP with N80C-R4, N80C-R2, and N80C mutants afforded ((N80C-R4)–ZnP)$_{m}$, ((N80C-R2)–ZnP)$_{m}$, and (N80C–ZnP)$_{m}$, respectively. After the purification, size exclusion chromatography (SEC) and UV-vis/CD spectroscopy experiments (Figures 2-2–2-4)[12] indicated the formation of the ((N80C-R4)–ZnP)$_{m}$, ((N80C-R2)–ZnP)$_{m}$, and (N80C–ZnP)$_{m}$ as shown in Figure 2-1. The CD spectra of the assemblies (Figure 2-4) are particularly useful because they show split-type Cotton effects at the Soret band absorptions, which indicates the formation of rigid assembly as described in the previous report.

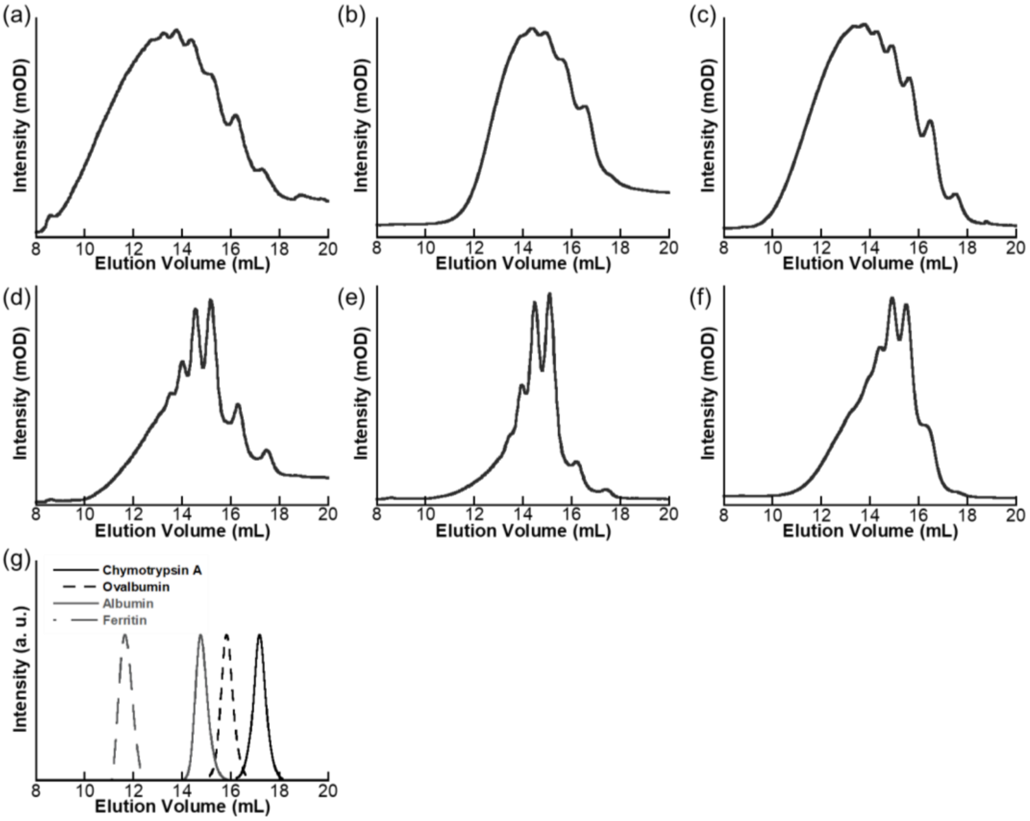

Figure 2-2. SEC traces of (a) ((N80C-R4)–ZnP)$_{m}$, (b) ((N80C-R2)–ZnP)$_{m}$, (c) (N80C–ZnP)$_{m}$, (d) ((D73A/N80C-R4)–ZnP)$_{m}$, (e) ((D73A/N80C-R2)–ZnP)$_{m}$, and (f) (D73A/N80C–ZnP)$_{m}$. (g) SEC traces of the authentic proteins (ferritin, albumin, ovalbumin, and chymotrypsin A). Conditions: [monomer unit] = 20 μM, eluent: PBS, temperature: 4 ºC, detection: absorbance at 430 nm.

The flexible assemblies, ((D73A/N80C-R4)–ZnP)$_m$, ((D73A/N80C)–ZnP)$_m$, and (D73A/N80C–ZnP)$_m$ were prepared in a similar manner and characterized (Figures 2-1–2-4). Especially, the CD spectra of these flexible assemblies are similar to the CD spectrum of ZnP reconstituted Cyt *b*$_{562}$ monomer, indicating the formation of flexible assemblies.

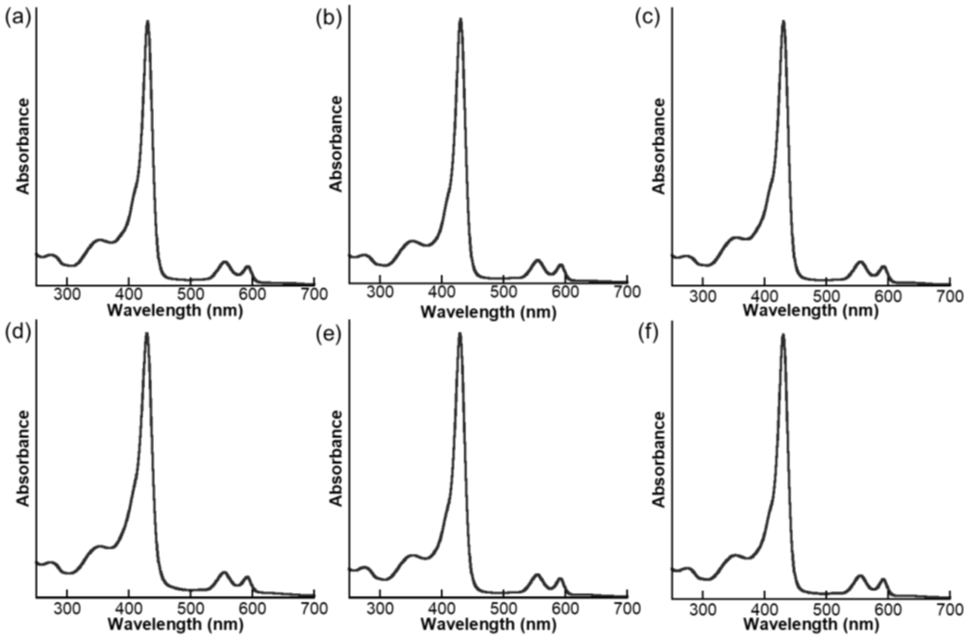

Figure 2-3. UV-vis spectra of (a) ((N80C-R4)–ZnP)$_m$, (b) ((N80C-R2)–ZnP)$_m$, (c) (N80C–ZnP)$_m$, (d) ((D73A/N80C-R4)–ZnP)$_m$, (e) ((D73A/N80C-R2)–ZnP)$_m$, and (f) (D73A/N80C–ZnP)$_m$ in PBS.

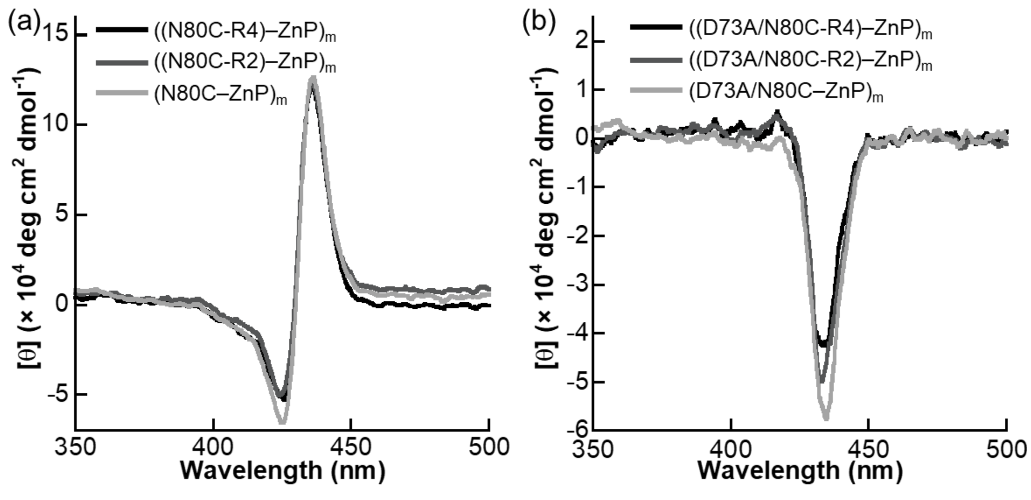

Figure 2-4. CD spectra of (a) rigid assemblies (black: ((N80C-R4)–ZnP)$_m$, dark grey: ((N80C-R2)–ZnP)$_m$, light grey: (N80C–ZnP)$_m$) and (b) flexible assemblies (black: ((D73A/N80C-R4)–ZnP)$_m$, dark grey: ((D73A/N80C-R2)–ZnP)$_m$, light grey: (D73A/N80C–ZnP)$_m$) in PBS.

Preparation of Rn tag attached reconstituted Cyt *b*$_{562}$ with ZnP

As a control sample for the analysis of the multivalent effect, the ZnP reconstituted wild-type Cyt *b*$_{562}$ (rCyt *b*$_{562}$), R4 and R2-attached variants, rCyt *b*$_{562}$-R4, rCyt *b*$_{562}$-R2 were prepared by the removal of heme from protein and subsequent addition of Zn-protoporphyrin IX.

Preparation of fluorescein-labeled Cyt *b*$_{562}$ assemblies and monomers

The fluorescein-labeling of Cyt *b*$_{562}$ assemblies, FITC-((N80C-R4)–ZnP)$_m$, and FITC-((D73A/N80C-R4)–ZnP)$_m$ were prepared by the conjugation of fluorescein isothiocyanate (FITC) to the amine group of protein matrices. The apparent ratio of FITC to the ZnP in the assembly is approximately 1/5 (Figure 2-5). The fluorescein-labeling of Cyt *b*$_{562}$ monomers, Flu-rCyt *b*$_{562}$-R4, and Flu-rCyt *b*$_{562}$, were carried out by the conjugation of ZnP reconstituted N80C mutant monomers with fluorescein-5-maleimide at the C80 positions.

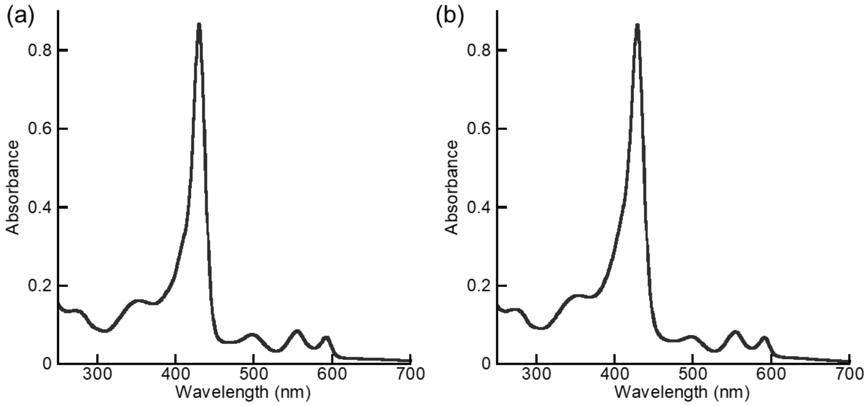

Figure 2-5. UV-vis spectra of (a) FITC-((N80C-R4)–ZnP)$_m$ and (b) FITC-((D73A/N80C-R4)–ZnP)$_m$. Absorbance around 490 nm corresponds to the λ_{max} of fluorescein.

Cellular uptake of Cyt *b*$_{562}$ assemblies and monomers to the HeLa cell

Cellular uptake events of both of the rigid and flexible assemblies were investigated using HeLa cells and characterized by fluorescence confocal microscopy. The culture medium (OPTI-MEM) containing the assemblies was added to cells adhered to a glass-bottom dish and the cells were incubated for 30 min at 37 °C. Fluorescence confocal microscopy measurements of the cells were made after washing with phosphate buffered saline (PBS). Figures 2-6a–f and 2-11 show the fluorescence confocal micrographs. Interestingly, fluorescence intensity detected in the range of 570–620 nm, indicating fluorescence from ZnP, was observed in all cases, indicating uptake of all of the assemblies. The fluorescence intensities measured for the cells treated with ((N80C-R4)–ZnP)$_m$, ((D73A/N80C-R4)–ZnP)$_m$, and ((D73A/N80C-R2)–ZnP)$_m$ are stronger than those observed in the case of assemblies without Rn tags.[13] These results indicate that cellular uptake efficiency is qualitatively enhanced by the introduction of R4/R2 tags onto the protein surface compared to the corresponding assemblies without Rn tags. In contrast, surprisingly, the strong fluorescence was observed in the cells treated with corresponding monomers, rCyt b_{562}-R4 and rCyt b_{562}-R2 (Figures 2-6g,h, 2-12a,b). The strong fluorescence was also detected with rCyt b_{562} despite the absence of the Rn tag (Figures 2-6i, 2-12c). Here, the author doubted that the ZnP itself was removed from the protein matrix and incorporated because ZnP is non-covalently bound in the heme pocket via the reversible interactions (K_d = 500 nM in rCyt b_{562}).[14] To confirm this possibility, the cellular uptake of fluorescein-labeled monomers and assemblies were performed.

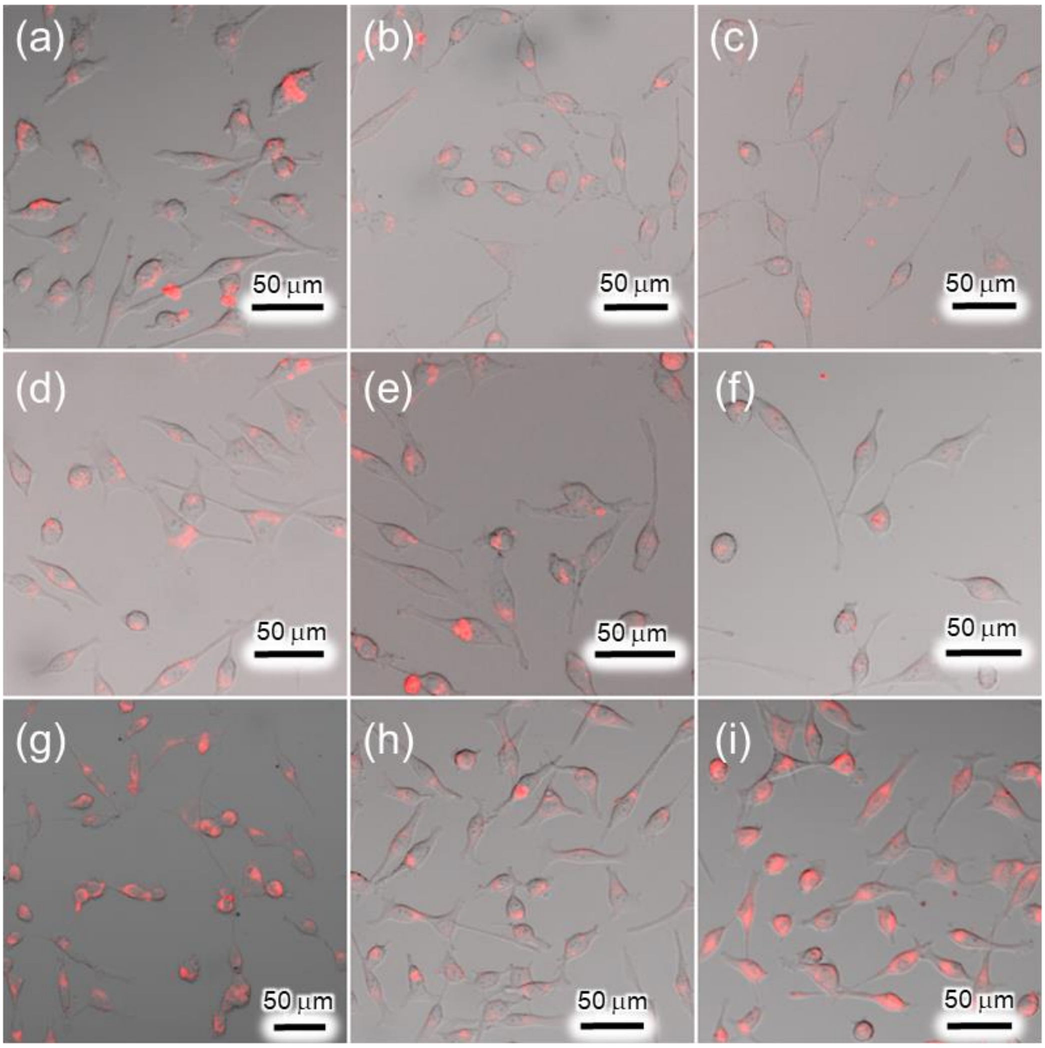

Figure 2-6. The overlaid fluorescence bright field images of HeLa cells incubated with (a) ((N80C-R4)–ZnP)$_m$, (b) ((N80C-R2)–ZnP)$_m$, (c) (N80C–ZnP)$_m$, (d) ((D73A/N80C-R4)–ZnP)$_m$, (e) ((D73A/N80C-R2)–ZnP)$_m$, (f) (N80C)–ZnP)$_m$, (g) reconstituted Cyt b_{562}-R4 with ZnP (rCyt b_{562}-R4), (h) rCyt b_{562}-R2, (i) rCyt b_{562}. λ_{ex} = 488 nm for assemblies or 561 nm for rCyt b_{562}. λ_{obs} = 570–620 nm.

Cellular uptake of fluorescein-labeled Cyt b_{562} assemblies and monomers to the HeLa cell

The fluorescein-labeled monomer Cyt b_{562}, Flu-rCyt b_{562}-R4 and Flu-rCyt b_{562}, were incubated to the cells to evaluate the cellular uptake using fluorescence confocal microscopy. Figure 2-7a,b shows no green fluorescence from fluorescein moiety in the cells treated with Flu-rCyt b_{562}-R4 and Flu-rCyt b_{562}, whereas strong red fluorescence was observed from ZnP. This finding clearly indicates that no incorporation of the protein matrices into the cells occurred in the case of Flu-rCyt b_{562}-R4 and Flu-rCyt b_{562}, and only the ZnP which has dissociated from the heme pocket was internalized into the cells. On the other hand, the incorporation of the protein moieties in the assembling systems was confirmed using fluorescein-labeled assemblies, FITC-((N80C-R4)–ZnP)$_m$ and FITC-((D73A/N80C-R4)–ZnP)$_m$ (Figure 2-6c,d). The co-localization of both red and green fluorescence from fluorescein and ZnP were observed, which indicates the internalization of the whole assembling system.[15] In contrast to the R8 tag, the R4 and/or R2 tags did not provide adequate cell penetration. However, the multivalent effect induced by the assembly to provide sufficient cell-penetrating ability.[16]

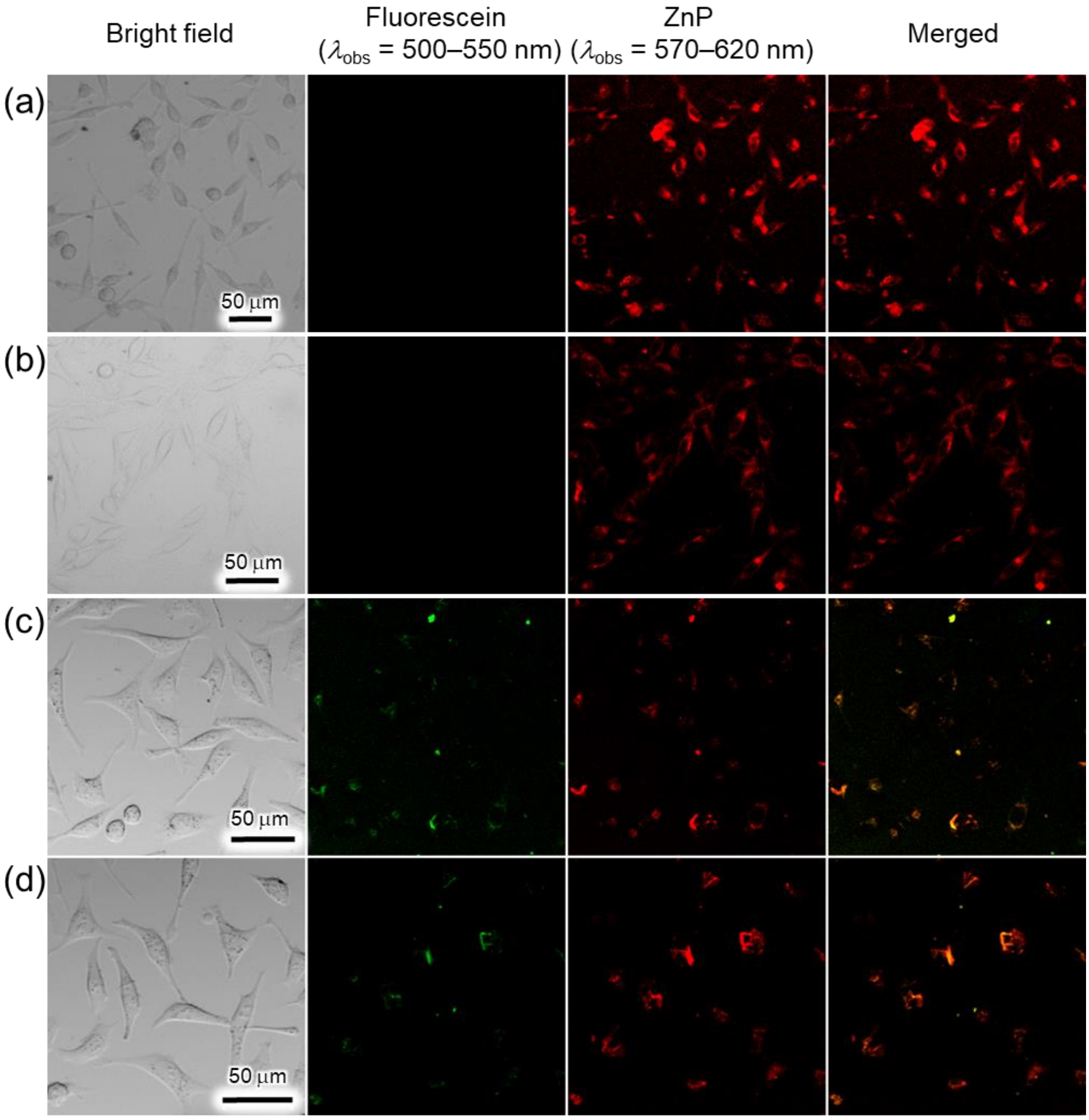

Figure 2-7. Bright field and fluorescence microscopic images of HeLa cells incubated with (a) Flu-rCyt *b*562-R4, (b) Flu-rCyt *b*562, (c) FITC-((N80C-R4)–ZnP)$_m$, and (d) FITC-((D73A/N80C-R4)–ZnP)$_m$. λ_{ex} = 561 nm (for monomers) and 488 nm (for assemblies).

Analysis of relative cellular uptake efficiencies of Cyt *b*562 assemblies

Relative cellular uptake efficiencies of the protein assemblies were evaluated by measuring the fluorescence spectra of the cell lysates (Figures 2-8 and 2-9). The fluorescence intensities derived from ZnP were analyzed by peak fitting as shown in Figure 2-10. Figure 2-8 shows the cellular uptake efficiencies of ((N80C-R4)–ZnP)$_m$, ((N80C-R2)–ZnP)$_m$, ((D73A/N80C-R4)–ZnP)$_m$, ((D73A/N80C)–ZnP)$_m$, and (D73A/N80C–ZnP)$_m$ relative to (N80C–ZnP)$_m$ obtained from peak fitting. Introduction of the R4/R2 tags significantly increases the cellular uptake efficiencies: in the rigid assemblies, 2.0-fold and 10-fold increases in ((N80C-R2)–ZnP)$_m$ and ((N80C-R4)–ZnP)$_m$ were observed respectively relative to (N80C–ZnP)$_m$, and in the flexible assemblies, the 1.4-fold and 2.6-fold increase in ((D73A/N80C-R2)–ZnP)$_m$ and ((D73A/N80C-R2)–ZnP)$_m$ were observed respectively compared to (D73A/N80C–ZnP)$_m$. In a comparison of the rigid and flexible assemblies, the rigid R4 tag assembly exhibits the 2.9-fold higher efficiency than the corresponding flexible assembly although there are almost no differences in the case of assemblies without Rn tags. These findings suggest that the pre-organized R4 tags in the rigid assembly provide more effective cellular uptake than the randomly positioned R4 tags in the flexible assembly.

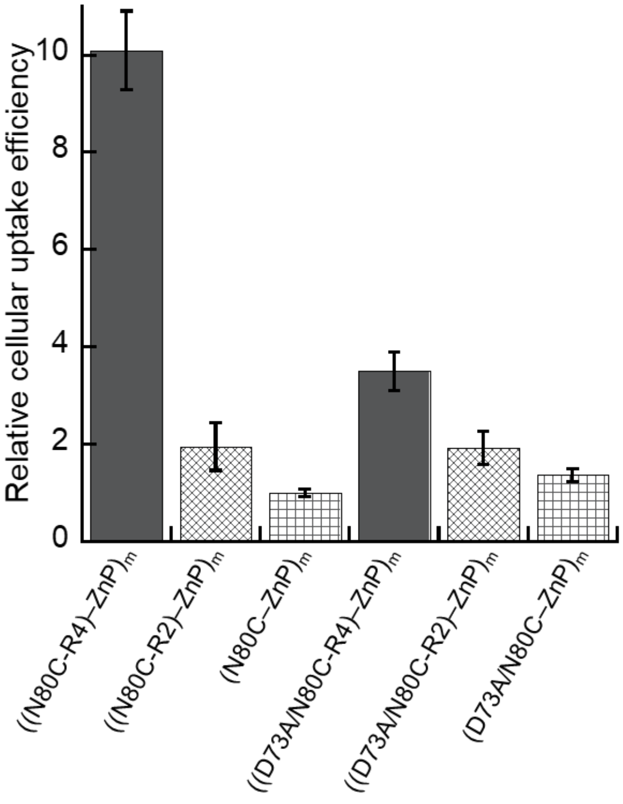

Figure 2-8. Relative cellular uptake efficiencies based on fluorescence intensities of the lysate of the cell treated with the assemblies.

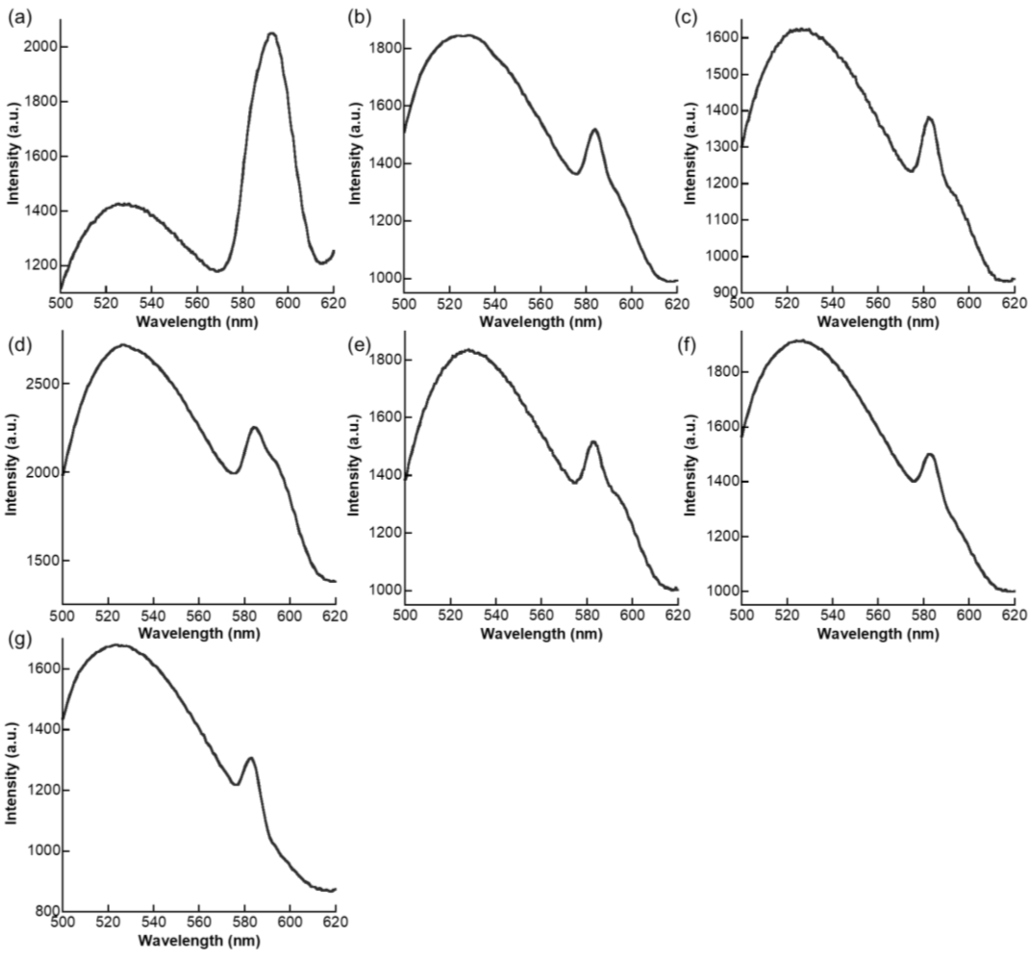

Figure 2-9. Fluorescence spectra of lysate of the cells treated by (a) ((N80C-R4)–ZnP)$_m$, (b) ((N80C-R2)–ZnP)$_m$, (c) (N80C–ZnP)$_m$, (d) ((D73A/N80C-R4)–ZnP)$_m$, (e) ((D73A/N80C-R2)–ZnP)$_m$ and (f) (D73A/N80C–ZnP)$_m$. (g) Control fluorescence spectra of lysate of cells incubated without any proteins under the same condition as the cellular uptake experiments.

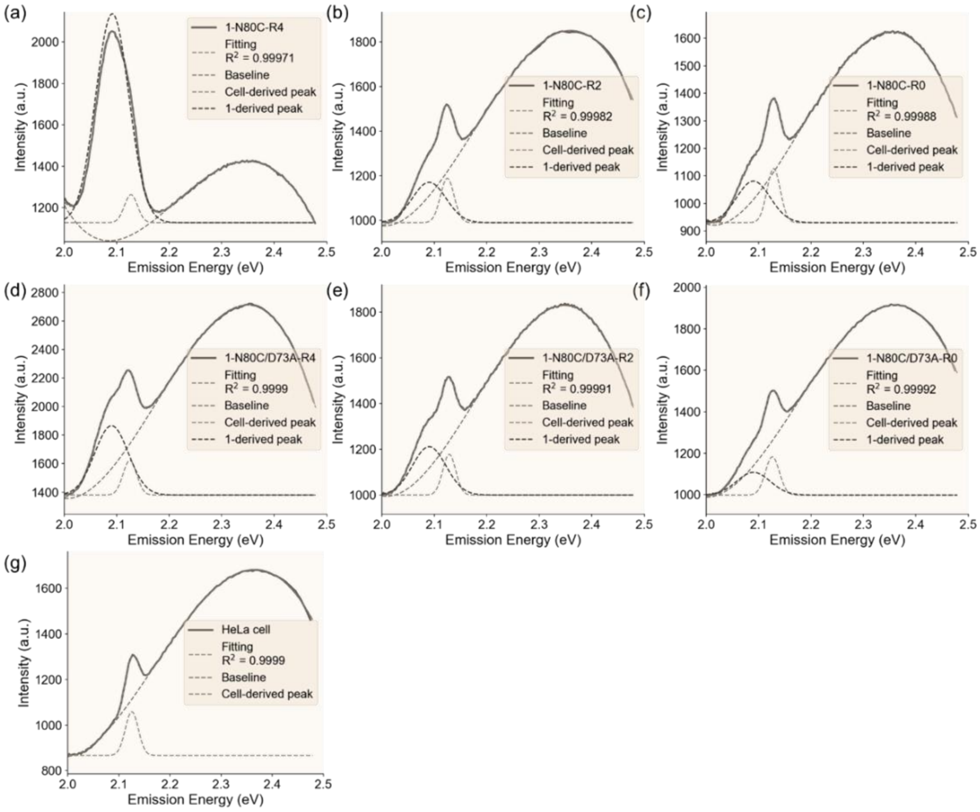

Figure 2-10. Plots of fluorescence intensity against fluorescence emission energy and the peak fitting results of lysate of the cells treated with (a) ((N80C-R4)–ZnP)$_m$, (b) ((N80C-R2)–ZnP)$_m$, (c) (N80C–ZnP)$_m$, (d) ((D73A/N80C-R4)–ZnP)$_m$, (e) ((D73A/N80C-R2)–ZnP)$_m$, and (f) (D73A/N80C–ZnP)$_m$. (g) Control fluorescence intensity of lysate of cells incubated without any proteins under the same conditions used in the cellular uptake experiment. The baseline was assigned using the quartic function (green). The fluorescence of Zn porphyrin moiety (594 nm, 2.091 eV, red) and the cell-intrinsic fluorescence (583 nm, 2.127 eV, cyan) were evaluated with the Gaussian distribution. The fitting results are indicated with an orange line with the R^2 value.

2-3. Summary

Cellular uptake efficiencies of rigid and flexible Cyt b_{562} assemblies with ZnP and R4/R2 tags were investigated. It is found that the combination of the R4 tag and the rigid assembly provides the best cellular uptake efficiency among them. Although the R8 is the best Rn tag for internalization of its cargo molecules, the multivalent effect of shorter Rn tags in the assembly provides enhanced cellular uptake ability. Especially, the present rigid Cyt b_{562} assembly can induce the efficient multivalent effects by the pre-organized Rn tags on the helical structure. These findings are expected to contribute to the development of artificial protein assemblies for use in cellular delivery applications based on the multivalent effect.

2-4. Experimental Section

Materials and methods

Instruments: ESI-TOF and MALDI-TOF MS analyses were performed with a Bruker Daltonics micrOTOF II spectrometer and an Autoflex III mass spectrometer, respectively. UV-vis spectra were measured with a Shimadzu BioSpec-nano spectrophotometer or Shimadzu UV-3150 double-beam spectrophotometer. Circular dichroism (CD) spectra were recorded with a JASCO J-820S spectrophotometer. Size exclusion chromatographic (SEC) analyses were performed using a Superdex 200 10/300 Increase GL column (GE Healthcare) with an ÄKTApurifier or ÄKTA Pure 25 systems (GE Healthcare) at 4 ºC. pH measurements were made with an F-72 Horiba pH meter. Fluorescence micrographs were obtained using a Nikon A1+ laser microscope system equipped with a Nikon CFI Plan Apo VC 20 (NA: 0.75, WD: 1.00) objective lens. Image analysis was performed using the ImageJ software (Version 1.51j8). Fluorescence spectra were recorded with a Shimadzu RF-6000 spectrofluorophotometer.

Materials: Maleimide-tethered Zn porphyrin, m–ZnP and Zn protoporphyrin IX, ZnP, were prepared according to previously reported procedures. Unless mentioned otherwise, all protein solutions were dissolved in a phosphate buffered saline (PBS). Other reagents and chemicals were purchased and used as received. Deionized water was prepared using a Millipore Integral3 apparatus.

Protein Sequence of Cytochrome b_{562} and its Mutants

wild-type Cyt b_{562}

ADLEDNMETLNDNLKVIEKADNAAQVKDALTKMRAAALDAQKATPPKLEDKSPDSP
EMKDFRHGFDILVGQIDDALKLANEGKVKEAQAAAEQLKTTRNAYHQKYR

wild-type Cyt b_{562}-R2

ADLEDNMETLNDNLKVIEKADNAAQVKDALTKMRAAALDAQKATPPKLEDKSPDSP
EMKDFRCGFDILVGQIDDALKLANEGKVKEAQAAAEQLKTTRNAYHQKYRGGGRR

wild-type Cyt b_{562}-R4

ADLEDNMETLNDNLKVIEKADNAAQVKDALTKMRAAALDAQKATPPKLEDKSPDSP
EMKDFRCGFDILVGQIDDALKLANEGKVKEAQAAAEQLKTTRNAYHQKYRGGGRRR
R

N80C
ADLEDNMETLNDNLKVIEKADNAAQVKDALTKMRAAALDAQKATPPKLEDKSPDSP
EMKDFRHGFDILVGQIDDALKLACEGKVKEAQAAAEQLKTTRNAYHQKYR

N80C-R2
ADLEDNMETLNDNLKVIEKADNAAQVKDALTKMRAAALDAQKATPPKLEDKSPDSP
EMKDFRHGFDILVGQIDDALKLACEGKVKEAQAAAEQLKTTRNAYHQKYRGGGRR

N80C-R4
ADLEDNMETLNDNLKVIEKADNAAQVKDALTKMRAAALDAQKATPPKLEDKSPDSP
EMKDFRHGFDILVGQIDDALKLACEGKVKEAQAAAEQLKTTRNAYHQKYRGGGRRR
R

N80C/D73A
ADLEDNMETLNDNLKVIEKADNAAQVKDALTKMRAAALDAQKATPPKLEDKSPDSP
EMKDFRHGFDILVGQIADALKLACEGKVKEAQAAAEQLKTTRNAYHQKYR

N80C/D73A-R2
ADLEDNMETLNDNLKVIEKADNAAQVKDALTKMRAAALDAQKATPPKLEDKSPDSP
EMKDFRHGFDILVGQIADALKLACEGKVKEAQAAAEQLKTTRNAYHQKYRGGGRR

N80C/D73A-R4
ADLEDNMETLNDNLKVIEKADNAAQVKDALTKMRAAALDAQKATPPKLEDKSPDSP
EMKDFRHGFDILVGQIADALKLACEGKVKEAQAAAEQLKTTRNAYHQKYRGGGRRR
R

Preparation of Cytochrome b_{562} and its Mutants

The gene expression systems used to obtain wild-type cytochrome b_{562}, Cyt b_{562}, and its mutants, N80C and N80C/D73A, were reported in our previous paper.[17] The insertion of C-terminal peptide-tag gene sequences into the Cyt b_{562} expression plasmids was performed by the polymerase chain reaction (PCR) using the KOD-Plus-Neo kit (Toyobo Life Science) according to the protocol of the manufacturer. The wild-type Cyt b_{562} and N80C/D73A mutant genes cloned into pUC118 were used as a template. The primer sequences used to insert the peptide-tag are shown in Table 2-1.

After PCR, the template DNA plasmids were digested with Dpn I (Thermo Fisher Scientific). Then, self-ligation of PCR products was carried out by Ligation high Ver.2 and T4 polynucleotide kinase (Toyobo Life Science) to obtain the desired plasmid DNAs. *E. coli* DH5α competent cells were transformed with the plasmids. After cell culture, the plasmids were purified using the PureLink™ Quick Plasmid Miniprep Kit (Thermo Fisher Scientific). DNA sequencing was performed to verify each correct mutation in the gene sequence. The peptide-tag fused Cyt b_{562} mutants were overexpressed in the *E. coli* strain BL21 and purified using cation exchange and gel filtration column chromatography as previously described.[17] The obtained peptide-tag fused Cyt b_{562} mutants were characterized by SDS-PAGE and MALDI-TOF MS, and stored at –80 ˚C.

The expression plasmids of peptide-tag fused N80C variants were prepared using the plasmid of peptide-tag fused Cyt b_{562} genes and primers used for N80C mutants reported in our previous paper.[17]

Table 2-1. The primers for the preparation of peptide-tag sequence insertion to template plasmid DNA.

Protein	**Primer**
wild-type Cyt b_{562}-R4 and D73A/N80C-R4	Forward: GGTGGCGGTCGTCGCCGTCGCTAATTCCTCATTTCCCTGTTGCCT Reverse: ACGATACTTCTGGTGATAGGCGTTGCGGGTCGTTTTCAGTTGCTC
wild-type Cyt b_{562}-R2 and D73A/N80C-R2	Forward: TAATTCCTCATTTCCCTGTTGCCTGCACTCAGGTAACAGGGAACT Reverse: GCGACGACCGCCACCACGATACTTCTGGTGATAGGCGTTGCGGGT

Surface Modification Reaction of Cytochrome *b*$_{562}$ Mutants

The m–ZnP (0.1 mg) in a DMSO solution (100 μL) was added to 191 μM of reduced N80C-R4 in 100 mM potassium phosphate buffer (pH 8.0, 350 μL). The mixture was then gently stirred at room temperature for 4 h under an N_2 atmosphere. Then, 1 mL of 7 M guanidine-HCl and 0.2 mL of 200 mM histidine-HCl were added to the protein solution for denaturation. The native heme and unreacted m–ZnP were removed from the aqueous phase by 2-butanone extraction performed five times. The solution was dialyzed against 1 L of PBS three times. The obtained assembly, ((N80C-R4)–ZnP)$_m$ was then concentrated using an Amicon Ultra concentrator (Merck Millipore) and stored at –80 °C. The obtained protein units were characterized by ESI-TOF MS and UV-vis spectroscopic measurements. Other assemblies, ((N80C-R2)–ZnP)$_m$, (N80C–ZnP)$_m$, ((D73A/N80C-R4)–ZnP)$_m$, ((D73A/N80C-R2)–ZnP)$_m$, and (D73A/N80C–ZnP)$_m$ were prepared according to the same procedure for preparation of ((N80C-R4)–ZnP)$_m$ and characterized by ESI-TOF MS: N80C-R4–ZnP (*m/z* calcd: 1110.40 (z = 12+), found: 1110.24), N80C-R2–ZnP (*m/z* calcd: 1084.38 (z = 12+), found: 1084.23), N80C–ZnP (*m/z* calcd: 1044.11 (z = 12+), found: 1043.88), D73A/N80C-R4–ZnP (*m/z* calcd: 1106.73 (z = 12+), found: 1106.55), D73A/N80C-R2–ZnP (*m/z* calcd: 1080.71 (z = 12+), found: 1080.48), D73A/N80C–ZnP (*m/z* calcd: 1040.44 (z = 12+), found: 1040.30)

Reconstitution of Cytochrome *b*$_{562}$ with Zn Protoporphyrin IX

The solution of histidine-HCl (200 mM, 1 mL) was added to the solution of wild-type Cyt *b*$_{562}$ (50 μM, 10 mL in 100 mM potassium phosphate buffer, pH 7.0). The solution mixture was acidified using 1 M HCl for denaturation and the native heme was removed from the aqueous phase by performing a 2-butanone extraction five times. The solution was dialyzed against 1 L of PBS to obtain the apo-form of Cyt *b*$_{562}$. Then, a solution of ZnP (2 mM, 375 μL in DMSO) was added to protein solution and the mixture was stirred overnight at 4 °C in the dark. The resultant solution was purified by anion exchange chromatography with a DEAE Sepharose Fast Flow column (GE healthcare). The obtained protein, rCyt *b*$_{562}$ was concentrated using an Amicon Ultra (Merck Millipore) concentrator and stored at –80 °C. The reconstituted protein was characterized by UV-vis spectroscopy. Other reconstituted proteins including Cyt *b*$_{562}$, rCyt *b*$_{562}$-R4, rCyt *b*$_{562}$-R2, were prepared according to the same procedure used for the preparation of rCyt *b*$_{562}$ and characterized by UV-vis spectroscopy. Reconstituted N80C-R4 and N80C with were prepared in the same manner to afford rN80C-R4, rN80C, respectively.

Modification of Cytochrome *b*$_{562}$ Assemblies with Fluorescein

FITC (6.1 mM 3.86 μL in DMSO) was added to a solution of ((N80C-R4)–ZnP)$_m$ (140 μM) in 100 mM of bicarbonate buffer (pH 9.0, 110 μL). Then, the mixture was gently stirred at room temperature for 3 h. The resultant solution was purified by gel filtration chromatography with a Sephadex G-25 column, concentrated using an Amicon Ultra (Merck Millipore) concentrator and stored at –80 °C to obtain FITC-((N80C-R4)–ZnP)$_m$. The obtained protein assembly was characterized by UV-vis spectroscopy. The FITC-((D73A/N80C-R4)–ZnP)$_m$ assembly was prepared according to the same procedure used for the preparation of FITC-labelled FITC-((N80C-R4)–ZnP)$_m$.

Preparation of Fluorescein Attached Cytochrome *b*$_{562}$

The fluorescein-5-maleimide (7.1 mM, 32 μL) in DMSO was added to a solution of reduced rN80C-R4 (150 μM) in 100 mM of potassium phosphate buffer (pH 8.0, 0.5 mL). Then the mixture was gently stirred at room temperature for 3 h. The reaction mixture was then purified by the gel filtration chromatography using the Sephadex G-25 column and concentrated using an Amicon Ultra (Merck Millipore) concentrator and stored at –80 °C. The obtained protein, Flu-rCyt *b*$_{562}$-R4, was characterized by UV-vis spectroscopy. Another fluorescein-labeled Cyt *b*$_{562}$ monomer, rCyt b$_{562}$, was prepared according to the same procedure using rN80C.

SEC Analysis

For SEC analysis, PBS was used as an eluent. The analysis was performed with a flow rate of 0.5 mL/min at 4 ºC with monitoring of the absorbance at 430 nm and 280 nm for detection. The column was validated using the following reagents (Gel Filtration Calibration kits HMW and LMW, GE Healthcare): ferritin (440 kDa), albumin (67 kDa), ovalbumin (44.0 kDa), chymotrypsin A (25.7 kDa) (Figure 2-2g).

Fluorescence Imaging for Cellular Uptake

HeLa cells (ca. 4.0 × 10^4 cells/mL) were seeded to a 35 mm glass bottom dish (14 mm glass diameter, FC14-10N) and incubated at 37 °C in a humidified CO_2 atmosphere (5%) for 24 h. The medium was replaced with OPTI-MEM containing Cyt *b*$_{562}$ assemblies (13 μM as monomers, 600 μL), and the cells were incubated for 30 min. The cells were then washed with

PBS and soaked in DMEM-FBS (600 μL). Then, the dish was mounted on the stage of a fluorescence microscope for fluorescence imaging (Figures 2-6, 2-7, 2-11, 2-12).

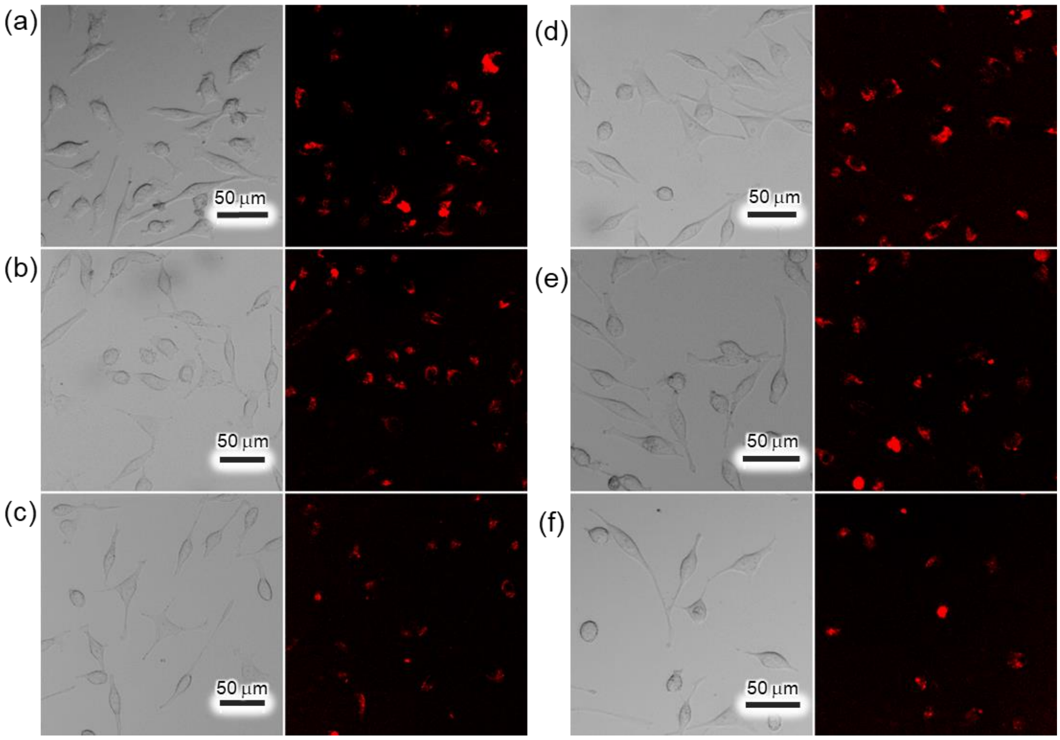

Figure 2-11. Bright field and fluorescence microscopic images of HeLa cells incubated with (a) ((N80C-R4)–ZnP)$_m$, (b) ((N80C-R2)–ZnP)$_m$, (c) (N80C–ZnP)$_m$, (d) ((D73A/N80C-R4)–ZnP)$_m$, (e) ((D73A/N80C-R2)–ZnP)$_m$ and (f) (D73A/N80C–ZnP)$_m$. λ_{ex} = 488 nm, λ_{obs} = 570–620 nm.

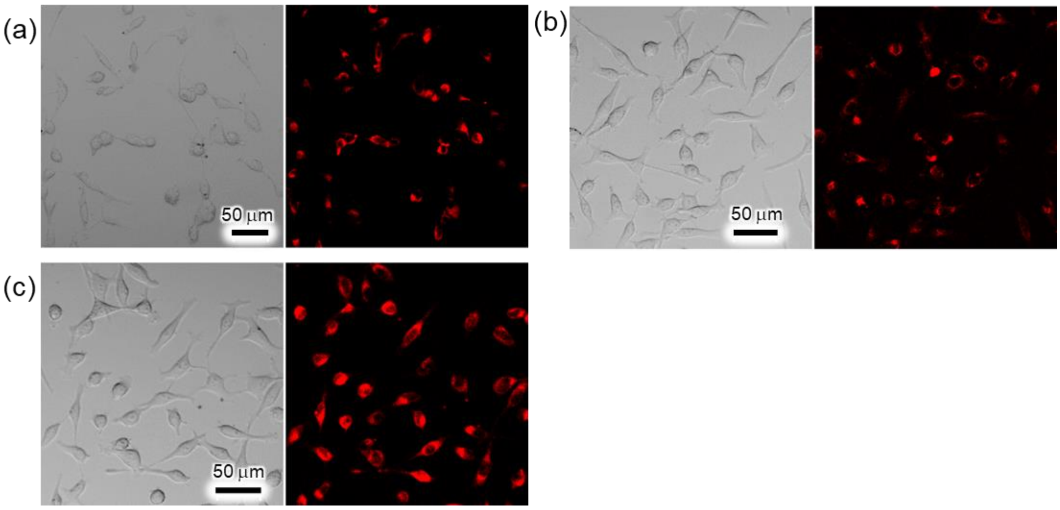

Figure 2-12. Bright field and fluorescence microscopic images of HeLa cells incubated with (a) rCyt b_{562}-R4, (b) rCyt b_{562}-R2, and (c) rCyt b_{562}. λ_{ex} = 561 nm, λ_{obs} = 570–620 nm.

Evaluation of Relative Cellular Uptake Efficiencies of the Assemblies by Quantification of Zn Porphyrin in the Cells

HeLa cells (ca. 2 × 10^6 cells) suspended in DMEM-FBS (4 mL) were seeded in a 100 mm dish and incubated at 37 °C in a humidified CO_2 atmosphere (5%) for 24 h. The medium was replaced with the OPTI-MEM containing Cyt b_{562} assemblies (13 μM as monomers, 3 mL). The cells were incubated for 30 min. The cells were then washed with PBS and dissociated from the dish surface by incubating them with trypsin–EDTA (2 mL) for 2–5 min at 37 °C. After the addition of DMEM-FBS (2 mL) and PBS (2 mL) to the dish, the resulting cell suspension was centrifuged, and the cell pellet was then sonicated to prepare cell lysate (1 mL). The fluorescence spectra of the supernatant solutions were measured (λ_{ex} = 430 nm).

For the quantitative analysis of cellular uptake of assemblies, fluorescence spectra of cell lysates were fitted using Python package, SciPy (Version 1.1.0). From the fluorescence spectrum of HeLa cells (Figure 2-9g), it is found that the HeLa cell itself has an intrinsic fluorescence peak around 583 nm. Therefore, the peak area of HeLa cell-intrinsic fluorescence is defined as the standard to indicate the amount of cells.

For the fitting of fluorescence peak using the Gaussian distribution function, the x-axes in the fluorescence spectra (Figure 2-9) were converted from wavelength to fluorescence emission energy (Figure 2-10). Then, the cell-derived fluorescence except for the peak at approximately 583 nm was defined as the background and fitted using quartic function ($f = ax^4 + bx^3 + cx^2 + dx + e$, green dotted line in Figure 2-10). The peak fitting was carried out to calculate the fluorescence peak area of the Zn porphyrin moiety (~2.091 eV, red dotted line in Figure 2-10) and the cell-intrinsic fluorescence (~2.127 eV, cyan dotted line in Figure 2-10) and visualized using Python package, matplotlib (Version 2.2.2). The fitting curve (orange dotted line) was validated by the small deviation ($R^2 > 0.999$). The relative value indicating the amount of protein assembly uptake was defined as the ratio of the fluorescence peak area of the Zn porphyrin moiety and cell-intrinsic fluorescence.

2-5. References and Notes

(1) (a) Luo, Q.; Hou, C.; Bai, Y.; Wang, R.; Liu, J. *Chem. Rev.* **2016**, *116*, 13571–13632. (b) Bai. Y.; Luo. Q.; Liu. J.; *Chem. Soc. Rev*. **2016**, *45*, 2756–2767.

(2) (a) Miao, L.; Han, J.; Zhang, H.; Zhao, L.; Si, C.; Zhang, X.; Hou, C.; Luo, Q.; Xu, J.; Liu, J. *ACS Nano*. **2014**, *8*, 3743–3751. (b) Sun, H.; Zhang, X.; Miao, L.; Zhao, L.; Luo, Q.; Xu, J.; Liu, J. *ACS Nano*. **2016**, *10*, 421–428.

(3) Song, W. J.; Tezcan, F. A. *Science*. **2014**, *346*, 1525–1528.

(4) (a) Li, Q.; So, C. R.; Fegan, A.; Cody, V.; Sarikaya, M.; Vallera, D. A.; Wagner, C. R. *J. Am. Chem. Soc*. **2010**, *132*, 17247–17257. (b) Petersburg, J. R.; Shen, J.; Csizmar, C. M. Murphy, K. A.; Spanier, J.; Gabrielse, K.; Griffith, T. S.; Fife, B.; Wagner, C. R. *ACS Nano*. **2018**, *12*, 6563–6576.

(5) Fegan, A.; White, B.; Carlson, J. C. T.; Wagner, C. R.; *Chem. Rev*. **2010**, *110*, 3315.

(6) (a) Molino, N. M.; Wang, S.-W. *Curr. Opin. Biotechnol*. **2014**, *28*, 75–82. (b) Aljabali, A. A. A.; Shukla, S.; Lomonossoff, G. P.; Steinmetz, N. F.; Evans, D. J. *Mol. Pharmaceutics.* **2013**, *10*, 3–10.

(7) Fujita, K.; Tanaka, Y.; Sho, T.; Ozeki, S.; Abe, S.; Hikage, T.; Kuchimaru, T.; Kizaka-Kondoh, S.; Ueno, T. *J. Am. Chem. Soc*. **2014**, *136*, 16902–16908.

(8) (a) Biswas, S.; Kinbara, K.; Niwa, T.; Taguchi, H.; Ishii, N.; Watanabe, S.; Miyata, K.; Kataoka, K.; Aida, T. *Nat. Chem.* **2013**, *5*, 613–620. (b) Fegan, A.; Kumarapperuma, S. C.; Wagner, C. R.: *Mol. Pharmaceutics*. **2012**, *9*, 3218–3227.

(9) (a) Futaki, S.; Suzuki, T.; Ohashi, W.; Yagami, T.; Tanaka, S.; Ueda, K.; Sugiura, Y. *J. Biol. Chem.* **2001**, *276*, 5836–5840. (b) F. Shiroh. *Adv. Drug Deliv. Rev*. **2005**, *57*, 547–558.

(10) (a) van Dun, S.; Schill, S.; Milroy, L.-G.; Brunsveld, L. *Chem. Eur. J.* **2018**, *24*, 16445–16451. (b) Yoon, Y.-R.; Lim, Y.; Lee, E.; Lee, M. *Chem. Commun.* **2008**, 1892–1894.

(11) Oohora, K.; Fujimaki, N.; Kajihara, R.; Watanabe, H.; Uchihashi, T.; Hayashi, T. *J. Am. Chem. Soc.* **2018**, *140*, 10145–10148.

(12) Size exclusion chromatography traces in Figure S2 indicate that the assemblies have the broad molecular weight distributions: dimer to ca. 30 mer in ((N80C-R4)–ZnP)$_\mathrm{m}$; dimer to ca. 20 mer in ((N80C-R2)–ZnP)$_\mathrm{m}$; dimer to ca. 30 mer in (N80C–ZnP)$_\mathrm{m}$; dimer to ca. 20 mer in ((D73A/N80C-R4)–ZnP)$_\mathrm{m}$; dimer to ca. 15 mer in ((D73A/N80C-R2)–ZnP)$_\mathrm{m}$ and dimer to ca. 20 mer in (D73A/N80C–ZnP)$_\mathrm{m}$.

(13) In the fluorescence microscopy, the differences in fluorescence intensity between cells treated with ((N80C-R2)–ZnP)$_\mathrm{m}$ and (N80C–ZnP)$_\mathrm{m}$ is negligible.

(14) Della Pia, E. A.; Chi, Q.; Elliott, M.; Macdonald, J. E.; Ulstrup, J.; Jones, D. D. *Chem. Commun*. **2012**, *48*, 10624–10626.

(15) In the present study, experimental results to evaluate the protein structure after the incorporation into the cell are unavailable and it is under investigation.

(16) The mechanism of the incorporation is considered to be the typical endocytosis which is seen in other cell-penetrating peptides (ref 17). This is supported by the punctate fluorescence signals derived from Zn porphyrin moieties on the protein units incorporated into the cell.

(17) Nakase, I.; Akita, H.; Kogure, K.; Gräslund, A.; Langel, Ü.; Harashima, H.; Futaki, S. *Acc. Chem. Res*. 2012, 45, 1132.

Chapter 3

Thermodynamically controlled formation of ring-shaped trimer and linear assembly of cytochrome b_{562}

3-1. Introduction

Supramolecular assembling systems provide unique structures and thermodynamic behaviors due to reversible interactions between building blocks. These properties are attractive for the development of functional materials.[1] Biomolecules have significant potential for use as building blocks and investigations of artificial protein assemblies have been recognized as an emergent topic over the past decade.[2] Many researchers have been reported the artificial protein assemblies with various supramolecular structures including fibers,[3] rings,[4] 2D sheets,[5] cages,[6] and tubes[7] so far.

Generally, fibrous supramolecular assemblies can reversibly transform into the ring-shaped structure.[8] This reversible transformation has derived the interaction between the terminus of fibrous assembly. The thermodynamic control of fiber ring conformational change depends on the rigidity of assemblies, and the flexible linear assembly can easily transform to cyclic assembly in a manner which depends on the concentration of their building block.[8,9] However, in the case of protein assembly, most of the fibrous (or linear) protein assemblies do not exhibit the transformation to the corresponding ring-shaped (or cyclic) protein assembly and *vice versa* due to the low flexibility. Additionally, both natural[10] and artificial ring-shaped protein assembly[4] often has highly-ordered protein–protein interface, which decreases the flexibility between proteins. Thus, thermodynamic control of ring–chain transformation of protein assembly is still challenging.

For the formation of the ring-shaped protein assembly, the distance between proteins is one of the crucial factors to stabilize the ring-shaped assembly. However, too much stabilization of assembly via protein–protein interaction would result in the selective formation of ring-shaped assembly. Therefore, the moderate linker length is important to induce the reversible ring–chain transformation. The author has found that N80C Cyt b_{562} assembly with the moderately long linker between the heme and the maleimide moiety shows the predominant formation of the ring-shaped protein assembly in dilute solution, whereas the formation of linear protein assembly in the concentrated solution (Figure 3-1).

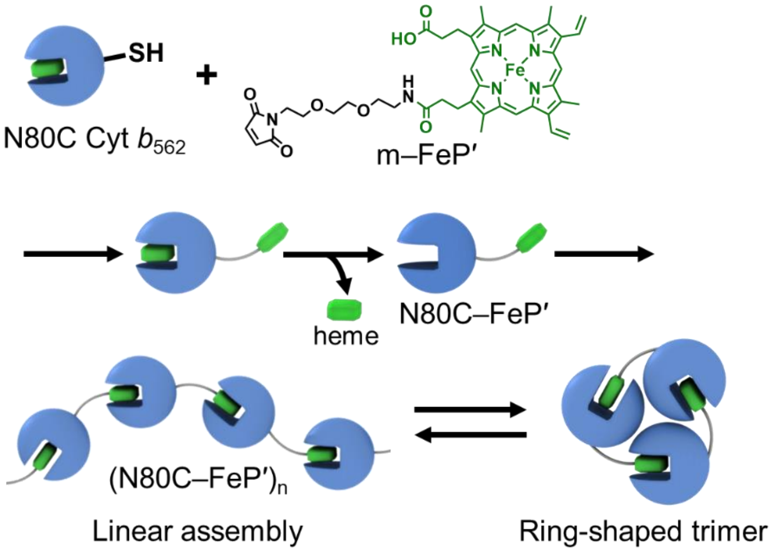

Figure 3-1. Schematic representation of the preparation of N80C Cyt b_{562} assembly using maleimide-tethered heme, m–FeP′, and two equilibrium states: linear assembly and ring-shaped trimer.

3-2. Results and Discussion

Preparation and size exclusion chromatographic analysis of N80C Cyt *b*₅₆₂ assembly using synthetic heme with long linker

Maleimide-tethered heme, m–FeP′, which has a linker derived from 2,2’-(ethylenedioxy)bis(ethylamine), was reacted with the N80C mutant to yield the monomer unit, N80C–FeP′ (Figure 3-1). The modified protein was characterized by LC-MS: found *m/z* = 1050.36, calcd *m/z* = 1050.61 (*z* = 12+). (Figures 3-2).

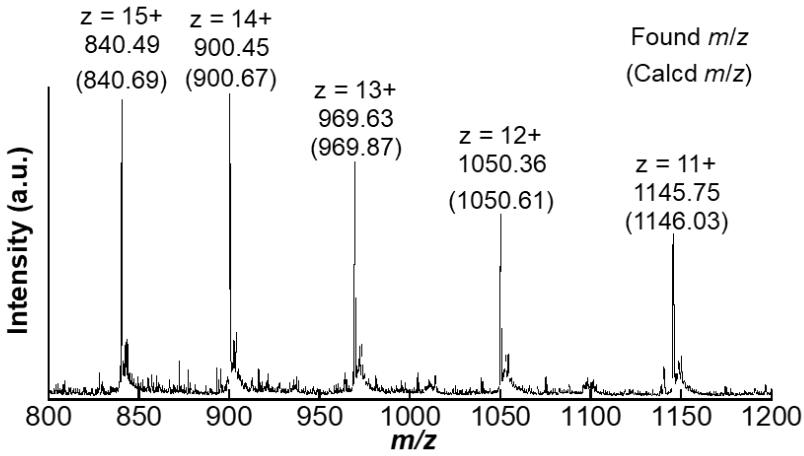

Figure 3-2. ESI-TOF MS of N80C–FeP′ (positive mode).

The size exclusion chromatography (SEC) of obtained (N80C–FeP′)$_n$ shows typical profiles with a broad molecular weight distribution which was seen in the previous systems in concentrated solution (Figure 3-3a, black), while dilution of the protein solution gradually increases the intensity of a peak which elutes at 10.9 mL (Figure 3-3a, red). The addition of the apo-form of Cyt b_{562} to the dilute solution of (N80C–FeP′)$_n$ decreases the intensity of the 10.9 mL peak with concomitant increases of new adjacent peaks eluting at 10.5 mL and 11.7 mL (Figure 3-3b).[11] Elution volumes of the monomer and linearly-assembled oligomers from dimer to hexamer were validated by the correlation between the estimated elution volumes against the logarithm value of the molecular weight of oligomers (Figure 3-4). It was revealed that the component of 10.9 mL elution, which increasingly forms upon dilution of (N80C–FeP′)$_n$ solution elutes between linearly-assembled dimer (11.7 mL) and a trimer (10.5 mL). This behavior is characteristic of (N80C–FeP′)$_n$ compared with a series of the previous assembling systems (Figures 3-13 and 3-14).[12]

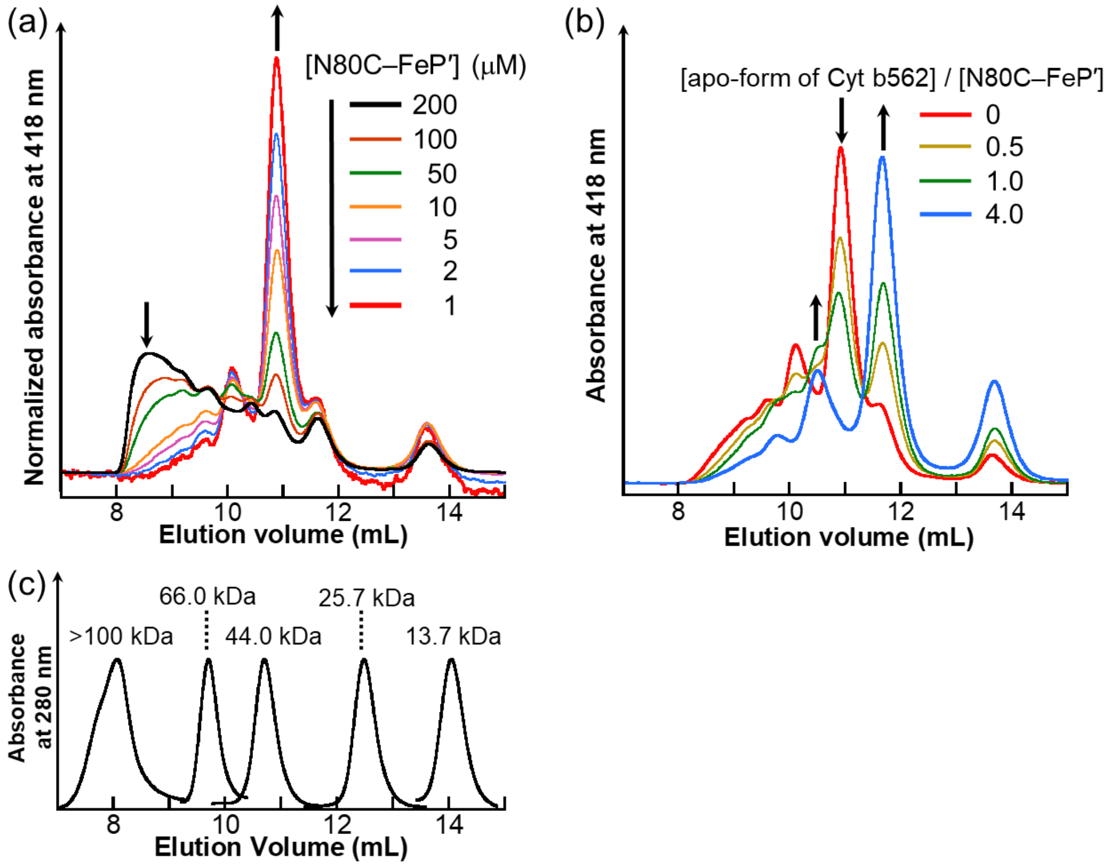

Figure 3-3. SEC profiles of (a) (N80C–FeP′)$_n$ at various concentration, (b) (N80C–FeP′)$_n$ ([N80C–FeP′] = 10 μM) formed upon capping by the apo-form of Cyt b_{562}, and (c) authentic samples: blue dextran (>100 kDa), albumin (66.0 kDa), ovalbumin (44.0 kDa), chymotrypsin (25.7 kDa), ribonuclease (13.7 kDa). Conditions: eluent = 100 mM potassium phosphate buffer,

pH 7.0, column = Superdex75 Increase.

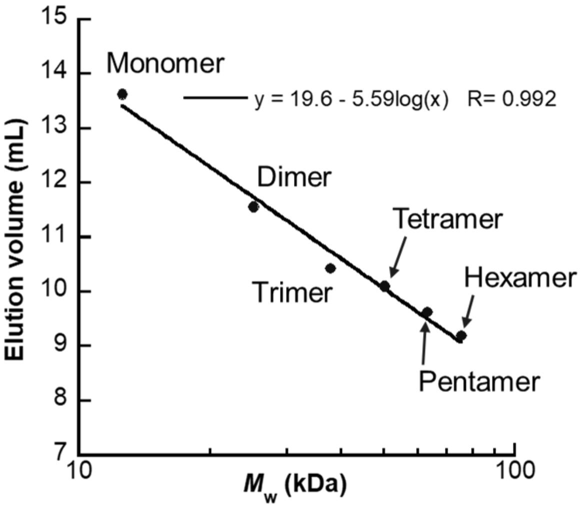

Figure 3-4. Plots of the estimated elution volumes of monomer and linear oligomers of N80C–FeP′ against the logarithm value of the corresponding molecular weight. The linear correlation in the plots indicates that the estimation is plausible.

Characterization of the isolated oligomer formed in a dilute condition

For the analysis of the molecular weight, the oligomer eluted at 10.9 mL by SEC, the ESI-TOF MS measurement of the isolated oligomer was performed.[13] Interestingly, the mass number identified in the deconvoluted mass spectrum is consistent with the number calculated for the trimer assembly (Figure 3-5a,b). The UV-vis spectrum of the isolated trimer was almost consistent with that of wild-type Cyt b_{562}, whereas slightly broad peaks were observed in UV-vis spectrum of the entire (N80C–FeP′)$_n$ (Figure 3-6) owing to the exposed heme moiety at the terminus. This result suggests that the heme moiety is not exposed in the isolated trimer. Taken together, (N80C–FeP′)$_n$ is estimated to predominantly form a ring-shaped structure in a dilute condition. The dynamic and static light scattering measurements indicate that the hydrodynamic diameter and molecular weight of this trimer are 6.47 nm and 38.0 kDa, respectively (Figure 3-7). These values are generally consistent with expected values for the ring-shaped trimer.

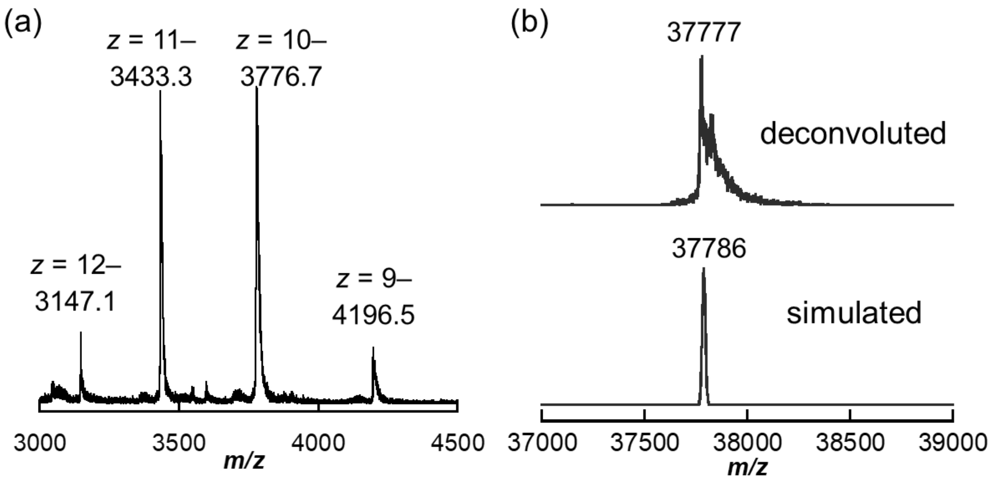

Figure 3-5. (a) ESI-TOF MS of oligomer eluted at 10.9 mL isolated by SEC in negative mode with the expected charge states. (b) Deconvoluted mass spectrum (top) and mass spectrum simulated as a trimer of N80C–FeP′ (bottom).

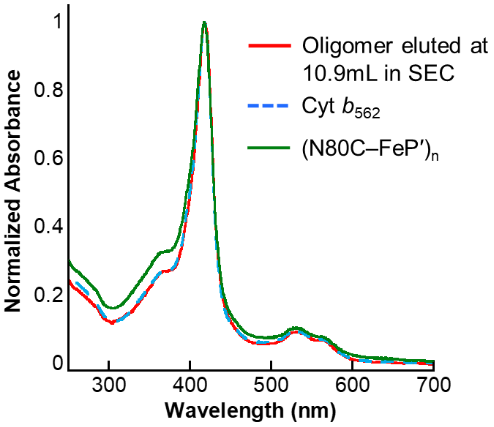

Figure 3-6. UV-vis spectra of the isolated oligomer, (N80C–FeP′)$_n$, and Cyt b_{562}

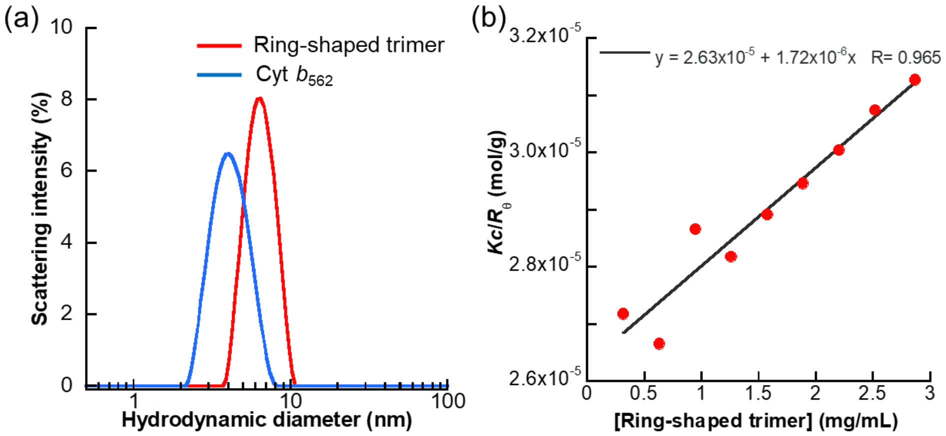

Figure 3-7. (a) Diameter distribution of Cyt b_{562} and the isolated ring-shaped trimer by dynamic scattering measurements. Conditions: [Monomer] = 100 μM, in 100 mM potassium phosphate buffer (pH 7.0) (b) Zimm plots obtained from static light scattering results of the isolated ring-shaped trimer. Protein concentration was calculated using the monomer concentration determined from the UV-vis spectrum and the molecular weight of the monomer unit. The optical constant, *K*, was calculated using *dn*/*dc* = 0.2 mL/g.

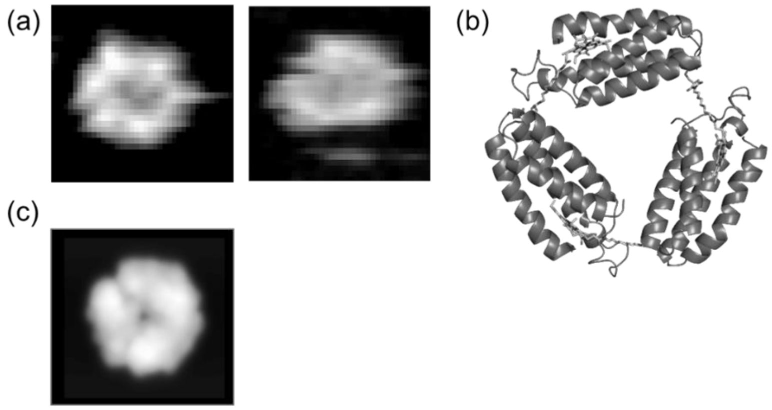

Figure 3-8. (a) Representative AFM image of the isolated ring-shaped trimer. (b) An energy-minimized model of the ring-shaped trimer. (c) Simulated AFM image. AFM images are depicted in the 20 nm × 20 nm squares.

The shape of the isolated trimer on the mica substrate was directly observed by high-speed atomic force microscopy (AFM).[14] Images of ring-shaped objects with about 15-nm diameter were observed in the solution (Figure 3-8a). This structure is slightly larger than the hydrodynamic diameter determined from dynamic light scattering. Considering the artifact caused by the interaction between the proteins and the flat substrate, we estimated a model for a flatly assembled ring-shaped trimer (Figure 3-8b). The simulated AFM image obtained by this model quite matches the experimental results supporting the direct observation of the ring-shaped trimer by AFM (Figure 3-8c). In contrast to the isolated ring-shaped trimer, a sample observed immediately after dilution of concentrated (N80C–FeP′)$_n$ solution reveals the fibrous structures with submicrometer lengths. This behavior is similar to the behavior exhibited by previous systems using the short linker.[15] Structural changes occurring upon interactions with substrate require that the ring-shaped trimer is flexible. Evidence for such flexibility can be inferred from the circular dichroism (CD) spectrum of the Soret band region (390–480 nm), which is similar to that of wild-type of Cyt b_{562} (Figure 3-9). This result suggests that no heme–heme exciton coupling occurs in (N80C–FeP′)$_n$ and the ring-shaped trimer.

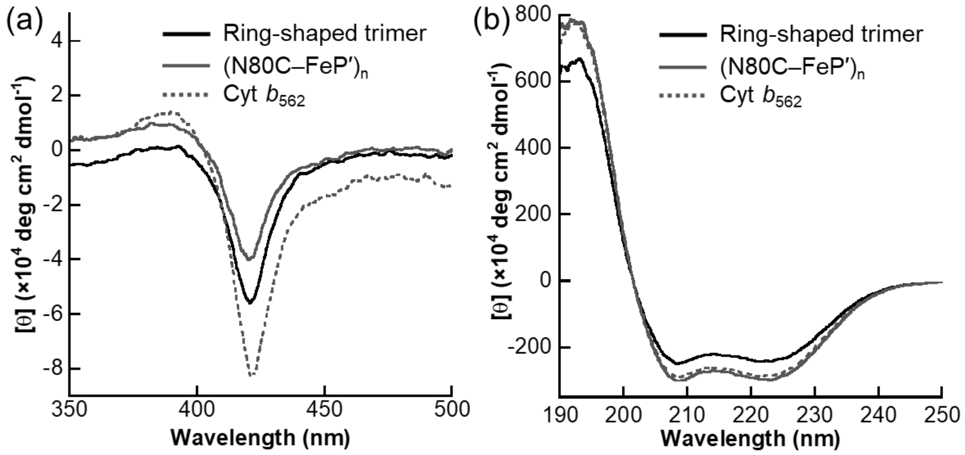

Figure 3-9. CD spectra of the isolated ring-shaped trimer, (N80C–FeP′)$_n$, and Cyt b_{562} at (a) Soret band region and (b) Far-UV region.

Thermodynamic stability analysis of the ring-shaped trimer of N80C–FeP′

Thermodynamic stability of the isolated ring-shaped trimer, (N80C–FeP′)$_n$, and holo- and apo-forms of Cyt b_{562} was evaluated by observing CD signal changes at 222 nm during the denaturation which occurs upon addition of guanidinium chloride (GdmCl) as shown in Figure 3-10a. Table 3-1 summarizes the value of [GdmCl]$_m$, the concentration of GdmCl for half denaturation. It is obvious that the ring-shaped trimer is more thermodynamically stable than the (N80C–FeP′)$_n$ and the apo-form of Cyt b_{562}. Compared with holo-form of Cyt b_{562}, the ring-shaped trimer has a lower [GdmCl]$_m$ value, possibly due to the lack of the hydrogen bonding interaction of one of two propionate side chains with the protein matrix, the structural distortion and/or steric repulsion between proteins.

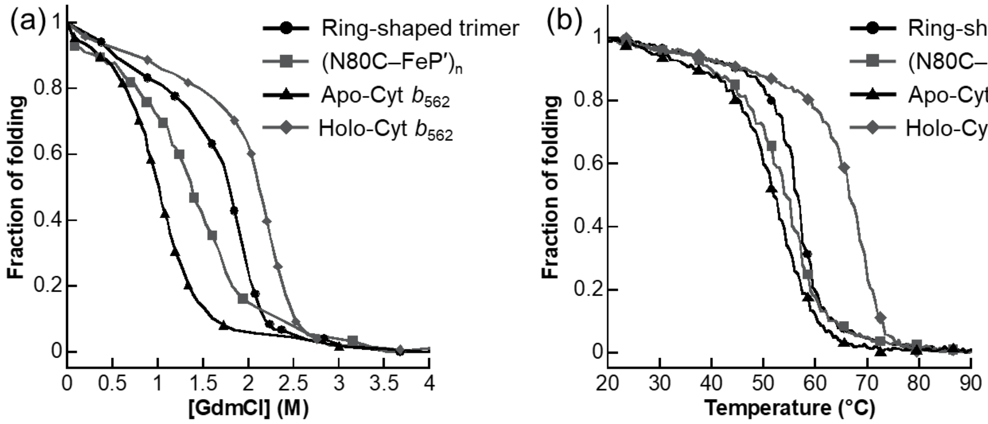

Figure 3-10. Fraction changes of folded protein obtained by CD signal changes at 222 nm (a) upon addition of GdmCl and (b) by the increase of temperature.

The denaturation of the protein which occurs upon increasing the temperature was also evaluated (Figure 3-10b). The values of T_m, the temperature for half protein unfolding, are summarized in Table 3-1. The results of the heat denaturation are generally consistent with those obtained by denaturation using denaturant. Both of the denaturation experiments indicate that the thermodynamic stability of the ring-shaped trimer is higher than that of (N80C–FeP′)$_n$. This stability could be caused by having the heme moieties fully incorporated within the protein matrix without exposure of the terminal structures in a linear oligomer.

Table 3-1. Denaturation parameters of the ring-shaped trimer, (N80C–FeP′)$_n$, and apo- and holo-form of Cyt b_{562}.[a]

	Ring-shaped trimer	(N80C–FeP′)$_n$	Apo-form of Cyt b_{562}	Holo-form of Cyt b_{562}
[GdmCl]$_m$/M	1.8	1.4	1.0	2.1
T_m/°C	56.5	54.5	52.0	66.5

[a] Denaturation behaviors were evaluated by CD spectrum (Figure 3-10). [GdmCl]$_m$ and T_m are the concentration of added GdmCl and temperature providing the half denaturation, respectively. Conditions: [protein] = 10 μM, solvent: 100 mM potassium phosphate buffer, pH 7.0.

Kinetic analysis of the formation and decomposition of the ring-shaped trimer

Heating of a solution of (N80C–FeP′)$_n$ appears to cause denaturation and disassembly of the protein assembly. The assembling behaviors of N80C–FeP′ cooled after the heat denaturation at 80 °C for 20 min were monitored by SEC measurements (Figure 3-11). The SEC trace after a 1-min cooling period indicates the formation of oligomers including the transiently formed linear trimer eluted at 10.5 mL.[16] After a 5-min cooling period, the transiently formed linear trimer decreases and the ring-shaped trimer is mainly formed. After 2 h, the size distribution is close to reaching equilibrium. These changes in the SEC profiles indicate that the ring-shaped trimer has a larger barrier to formation relative to the linear trimer,[17] but this barrier to the formation is relatively low because the equilibration is almost complete within 5 minutes. Moreover, peak fitting of the SEC trace of the (N80C–FeP′)$_n$ before denaturation was performed to estimate the population of each oligomer (Figure 3-12). The population of the linear trimer was found to be ca. 10 % of the ring-shaped trimer, which indicates that the ring-shaped trimer is more thermodynamically stable relative to the linear trimer.

The kinetic stability of the isolated ring-shaped trimer was evaluated by the SEC analysis of the incubated ring-shaped trimer at 25 °C in the concentrated solution state (100 μM). After allowing the solution to stand for 24 h, it was found that ca. 70 % of the ring-shaped trimer remains (Figure 3-11b).

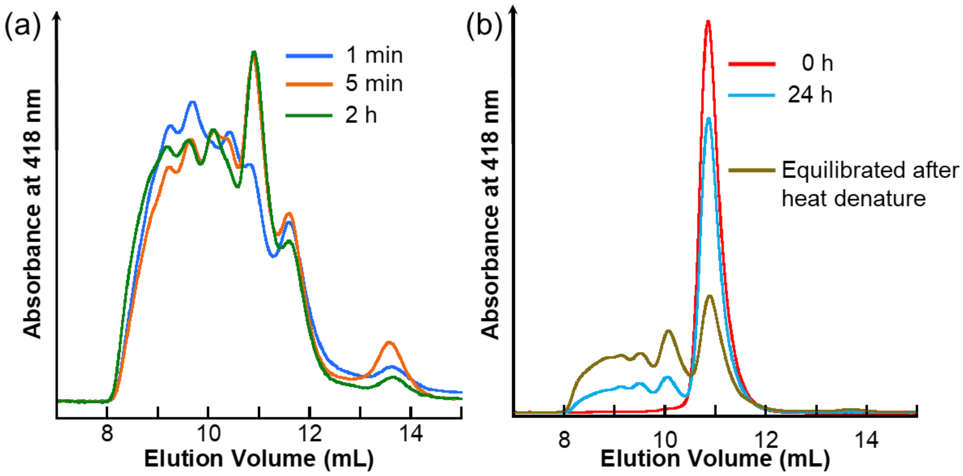

Figure 3-11. (a) SEC traces of (N80C–FeP′)$_n$ cooled after heat denaturation. (b) SEC traces of the isolated ring-shaped trimer after concentration. Cyan and red lines show the samples standing at 25 °C for 0 h and 24 h, respectively, after concentration. The brown line shows the sample equilibrated after heat denaturation. Conditions: [N80C–FeP′] = 20 μM, in (a) and 100 μM in (b), other conditions are the same as described in Figure 3-3.

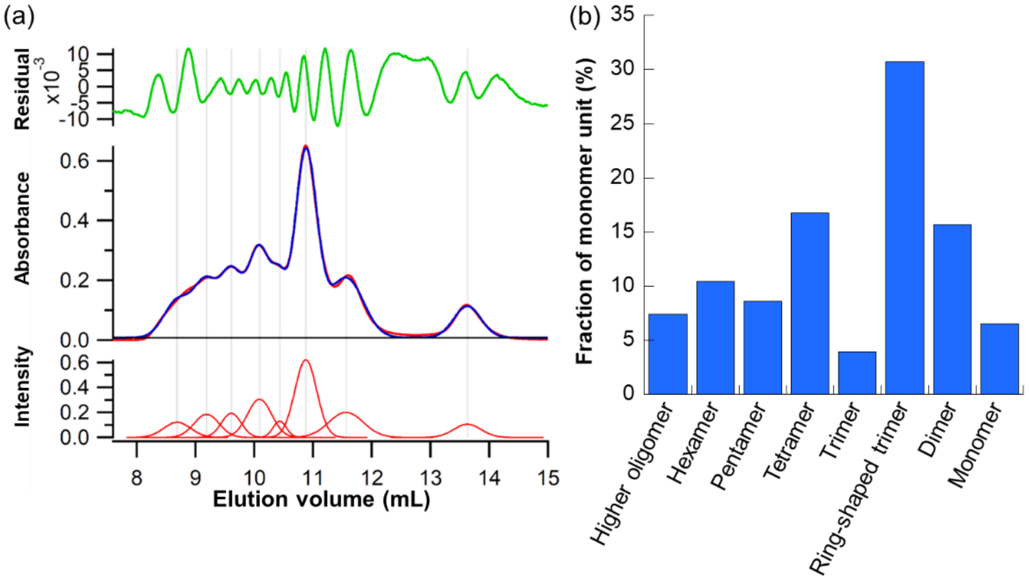

Figure 3-12. (a) Fitting results of the SEC trace of the (N80C–FeP′)$_n$. (b) The population of each oligomer estimated from the fitting results.

These findings indicate three thermodynamic and kinetic characteristics of the (N80C–FeP′)$_n$: (i) the ring-shaped trimer is thermodynamically more stable than the linear oligomers in dilute solution; (ii) the linear trimer is particularly much more unstable than the ring-shaped trimer; and (iii) the kinetic barrier from the linear trimer to the ring-shaped trimer is low, while the kinetic barrier of the reverse reaction is relatively high and provides kinetic stability to the ring-shaped trimer even in a concentrated solution.

3-3. Summary

The present Cyt b_{562} assembling system prepared via the heme–heme pocket interaction is found to form a thermodynamically stable ring-shaped structure. The ring-chain equilibrium generally occurs in a broad distribution in supramolecular polymerization of the simple molecules/proteins.[4,8] In contrast, the specific and unique stabilization of the ring-shaped trimer is generated in this system due to the structural factors derived from the structure of Cyt b_{562}, the heme attachment position and the length of the linker between the heme moiety and the protein. Further detailed investigations of the mechanism of formation of the unique ring-shaped structure are expected to contribute to the construction of supramolecular protein assemblies.

3-4. Experimental Section

Materials and methods

Instruments: ESI-TOF MS analyses were performed with a Bruker Daltonics micrOTOF II mass spectrometer. UV-vis spectra were measured with a Shimadzu BioSpec-nano or Shimadzu UV-3600 plus double-beam spectrometer. Circular dichroism (CD) spectra were recorded with a JASCO J-820S spectrometer. Size exclusion chromatographic (SEC) analyses were performed with an ÄKTA Pure 25 system (GE Healthcare) at 4 ºC. Dynamic light scattering (DLS) and static light scattering (SLS) measurements were performed using a Zetasizer µV (Malvern Instruments). pH measurements were made with an F-72 Horiba pH meter.

Materials: Maleimide-tethered heme derivatives m–FeP′ and m–FeP were prepared according to procedures reported in the literature.[18] Cyt b_{562} and its mutants were prepared by our previously reported methods.[15] Other reagents and chemicals were purchased and used as received. Unless mentioned otherwise, all protein solutions were dissolved in a 100 mM potassium phosphate buffer (pH 7.0). Deionized water was prepared using a Millipore Integral3 apparatus.

Protein sequence of cytochrome *b*$_{562}$ mutants

Cyt *b*$_{562}$

ADLEDNMETLNDNLKVIEKADNAAQVKDALTKMRAAALDAQKATPPKLEDKSPDSP
EMKDFRHGFDILVGQIDDALKLANEGKVKEAQAAAEQLKTTRNAYHQKYR

N80C

ADLEDNMETLNDNLKVIEKADNAAQVKDALTKMRAAALDAQKATPPKLEDKSPDSP
EMKDFRHGFDILVGQIDDALKLACEGKVKEAQAAAEQLKTTRNAYHQKYR

H63C

ADLEDNMETLNDNLKVIEKADNAAQVKDALTKMRAAALDAQKATPPKLEDKSPDSP
EMKDFRCGFDILVGQIDDALKLANEGKVKEAQAAAEQLKTTRNAYHQKYR

Preparation of surface modified cytochrome *b*$_{562}$ mutants

The synthesized Fe porphyrin, m–FeP′ (0.1 mg) in a DMSO solution (0.1 mL) was added to 166 μM of reduced N80C mutant solution. The mixture was then gently stirred at room temperature for 75 min under an N_2 atmosphere. Then, reaction mixture was acidified using 1 M HCl for denaturation. The native heme and excess m–FeP′ were removed from the aqueous phase by 2-butanone extraction performed five times. The solution was dialyzed against 1 L of 100 mM potassium phosphate buffer (pH 7.0). The obtained assembly, (N80C–FeP′)$_n$, was then concentrated using an Amicon Ultra concentrator (Merck Millipore) and stored at –80 °C. The obtained protein units were characterized by ESI-TOF MS, UV-vis spectroscopy and size exclusion chromatography using Superdex 75 Increase 10/300 GL and/or 200 Increase 10/300 GL (GE healthcare). Other assemblies, (N80C–FeP)$_n$ and (H63C–FeP′)$_n$ assembly, were prepared and characterized according to the same procedure for (N80C–FeP′)$_n$ and characterized by ESI-TOF MS: N80C–FeP′ (*m/z* calcd: 1050.61 (*z* = +12), found: 1050.30), N80C–FeP (*m/z* calcd: 1044.11 (*z* = +12), found: 1043.88), H63C–FeP′ (*m/z* calcd: 1048.69 (*z* = +12), found: 1048.43)

SEC analysis

The analysis was performed using a Superdex 75 Increase 10/300 GL (GE Healthcare) column or Superdex 200 Increase 10/300 GL (GE Healthcare) column with a flow rate of 0.5 mL/min at 4 ºC with monitoring of the absorbance at 418 nm and 280 nm for detection. The column was validated using the following reagents (Gel Filtration Calibration kits HMW and LMW, GE Healthcare): Superdex 200 Increase: thymoglobulin (669 kDa), ferritin (440 kDa), catalase (232 kDa), albumin (66.0 kDa), ribonuclease A (13.7 kDa); Superdex 75 Increase: blue dextran 2000 (2000 kDa), albumin (66.0 kDa), ovalbumin (44.0 kDa), chymotrypsin (25.7 kDa), ribonuclease A (13.7 kDa).

Light scattering analysis

To analyze the protein solution, a 12 μL quartz cuvette was utilized. Before adding the sample solution into the cuvette, the sample was filtered with a Millex-GV 0.22-μm filter (Merck Millipore). The cuvette was inserted into the apparatus for 30 seconds of equilibration at the 25 °C before measurements were performed. The wavelength of the laser irradiation was 830 nm. The scattering measurement angle was 90°. For dynamic light scattering (DLS) measurements, the autocorrelation functions of the observed signals were analyzed in protein analysis mode. The hydrodynamic diameters of the proteins were obtained using the scattering intensity-based particle size distribution mode (Fig. 3-7a).

For static light scattering (SLS) measurements, the Rayleigh ratio (R_θ) of the samples with different protein concentrations was analyzed from the time-averaged scattering intensity of the samples and toluene as a standard. The obtained R_θ values were analyzed with the Zimm plot equation[19]

$$\frac{Kc}{R_\theta} = \frac{1}{M_w}\left(1 + \frac{q^2 R_g^2}{3}\right) + 2A_2 c \tag{17}$$

where K is an optical constant, c is the sample concentration, M_w is the weight-average molecular weight, q is the scattering vector, R_g is the radius of gyration, A_2 is the second osmotic virial coefficient, and K is given as

$$K = \frac{4\pi^2 n_0^2}{N_A \lambda^4}\left(\frac{dn}{dc}\right)^2 \tag{18}$$

where λ is the wavelength of the light, N_A is Avogadro's number, n_0 is the refractive index of the medium, and dn/dc is the change in refractive index with sample concentration. In the case of a small protein ($R_g < 10$ nm), the qR_g factor is quite small ($qR_g << 1$) enough to regard as negligible and the Zimm plot equation can be expressed as:

$$\frac{Kc}{R_\theta} = \frac{1}{M_w} + 2A_2 c \tag{19}$$

Modeling of the ring-shaped trimer

The modeling was performed using YASARA[20] Structure Version 13.6.16 that employed force field AMBER03[21] for protein residues and GAFF[22] using AM1/BCC[23] partial charges for the heme moiety covalently bound to Cys80. The calculation was carried out using YASARA Structure Version 13.6.16 employing force field AMBER03. To maintain the correct coordination geometry, the distances from the metal to all four pyrrole N atoms of the porphyrin ligand were constrained to 2.0 Å. The hexa-coordination by ligation with Met7 and His102 was represented by two force field arrows and the distances of the Fe–S and Fe–N dative bonds were constrained to 2.3 and 2.0 Å, respectively, according to the NMR structure (PDB ID: 1QPU) of Cyt b_{562}. The partial charge of the metal was set to +2 and the total charge of the heme was set to zero. Manually constructed ring-shaped trimer was solvated in a box of TIP3P water molecules using periodic boundaries at pH 7.0 and a density of 0.997 g/mL. The minimized structure was obtained by steepest descent minimization and simulated annealing at 298 K.

High-speed atomic force microscopy (HS-AFM) imaging

HS-AFM imaging was carried out using a laboratory-designed HS-AFM apparatus operated with tapping mode.[24] The dimensions of the cantilever (Olympus) were 6−7 μm length, 2 μm width, and 90 nm thickness. The nominal spring constant was 0.1−0.2 N/m, the resonant frequency was 0.7−1 MHz, and the quality factor in aqueous solution was ca. 2. For the HS-AFM imaging, the free oscillation amplitude was set to 1−2 nm, and the set-point amplitude was approximately 90% of the free oscillation amplitude. An amorphous carbon tip grown by electron-beam deposition under scanning electron microscopy was used.[25] After the electron-beam deposition, the tip was sharpened by plasma etching under Ar gas (tip apex, d = ca. 4 nm).

In the HS-AFM imaging and processing, mica was used as a substrate. The solution (3 μL) of isolated ring-shaped trimer (1 μM as monomer) or $(\text{N80C–FeP}')_n$ (0.24 μM as monomer) soon after dilution of concentrated solution (1.2 mM as monomer) was deposited onto the freshly cleaved mica substrate. After the 3-min incubation, the substrate was thoroughly washed with a buffer (100 mM potassium phosphate buffer, pH 7.0) to remove excess molecules. The HS-AFM imaging was performed in the buffer at room temperature.

Simulation of AFM images

Simulation of AFM images was performed using custom software based on IgorPro 6 (Version 6.3.6.0, Wavemetrics, Lake Oswego, Ore., USA) software. The pseudo AFM image was generated using a cone-shaped AFM tip with a radius of 0.5 nm and half cone angle of 10°, and the energy minimized structure of the ring-shaped trimer. During the simulation, the orientation of the ring-shaped trimer was rotated along the longitudinal axis of the shape and adjusted so that the appearance of the simulated image was close to the experimental AFM image. After construction of the simulated image, the image was filtered by a low-pass filter with a cut off spatial frequency of 2 nm because the spatial resolution of the HS-AFM is generally limited to 2 nm.

Fitting analysis of SEC chromatogram

The peak fitting was performed using IgorPro (Version 6.1.2.1). The elution peak of each oligomer in SEC was fitted using the Gaussian distribution function. The initial fitting values for lower molecular weight oligomers (monomer to pentamer) were determined from the exact peak top values in SEC and FWHW. The initial fitting values for peaks of oligomers longer than hexamer were assigned using peak top values calculated from the relationship between the molecular weight of monomer to pentamer and elution peak top values (Figure 3-4).

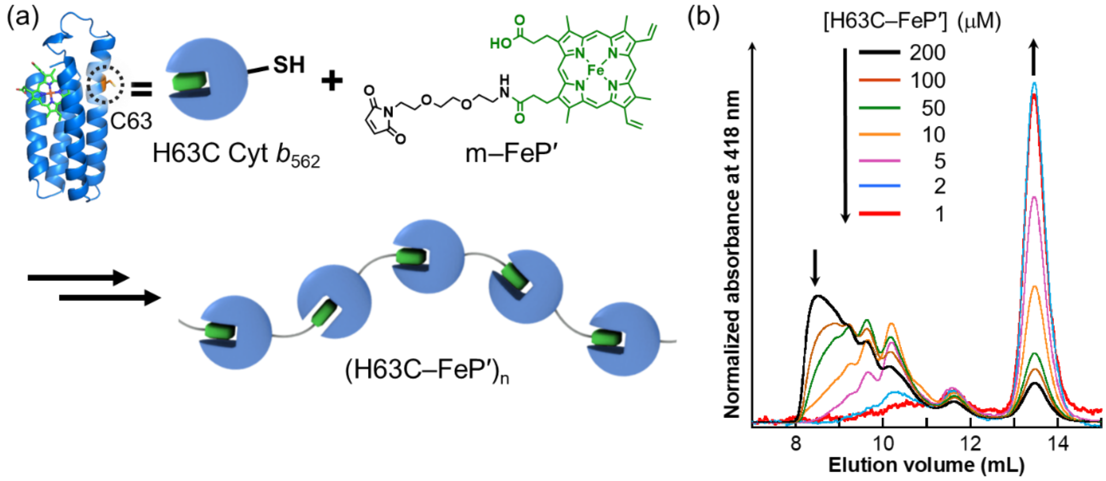

Figure 3-13. (a) Schematic representation for preparation of (H63C–FeP′)$_n$. (b) SEC profiles of (H63C–FeP′)$_n$ at various concentration.

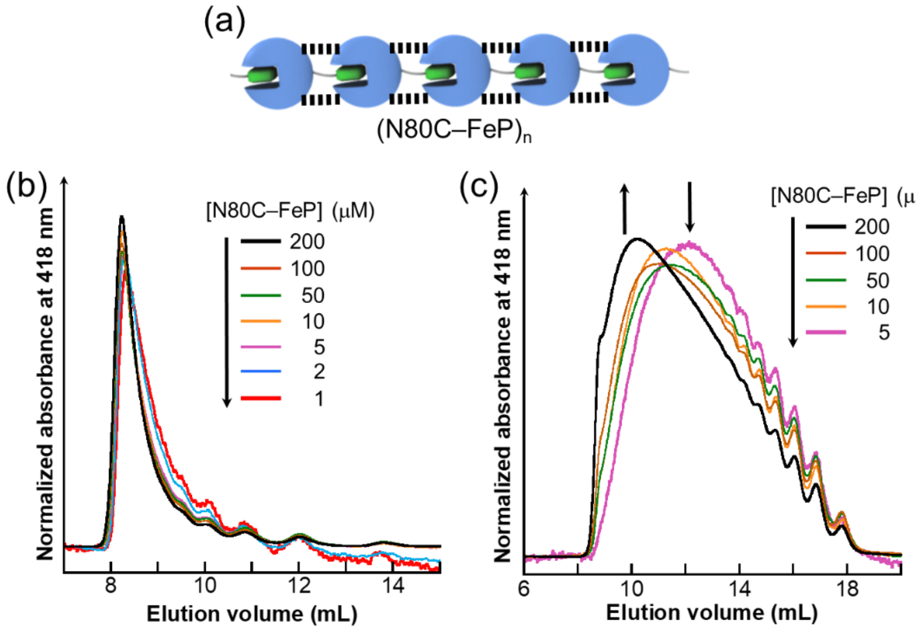

Figure 3-14. (a) Schematic representation of (N80C–FeP)$_n$. (b,c) SEC profiles of (N80C–FeP)n at various concentration using (b) Superdex 75 Increase column and (c) Superdex 200 increase column.

3-5. References and Notes

(1) (a) Brunsveld, L.; Folmer, B. J. B.; Meijer, E. W.; Sijbesma, R. P. *Chem. Rev.* **2001**, *101*, 4071–4097. (b) Krieg, E.; Bastings, M. M. C.; Besenius, P.; Rybtchinski, B. *Chem. Rev.* **2016**, *116*, 2414–2477.

(2) (a) Luo, Q.; Hou, C.; Bai, Y.; Wang, R.; Liu, J. *Chem. Rev.* **2016**, *116*, 13571–13632. (b) Bai. Y.; Luo. Q.; Liu. J.; *Chem. Soc. Rev*. **2016**, *45*, 2756–2767. (c) Levy, Y. *Biochemistry*. **2017**, *56*, 5040–5048.

(3) (a) Hou, C.; Li, J.; Zhao, L.; Zhang, W.; Luo, Q.; Dong, Z.; Xu, J.; Liu, J. *Angew. Chem. Int. Ed.* **2013**, *52*, 5590–5593. (b) Yamanaka, M.; Hoshizumi, M.; Nagao, S.; Nakayama, R.; Shibata, N.; Higuchi, Y.; Hirota, S. *Protein Sci*. **2017**, *26*, 464–474. (c) Miao, L.; Han, J.; Zhang, H.; Zhao, L.; Si, C.; Zhang, X.; Hou, C.; Luo, Q.; Xu, J.; Liu, J. *ACS Nano*. **2014**, *8*, 3743–3751.

(4) (a) Carlson, J. C. T.; Jena, S. S.; Flenniken, M.; Chou, T.; Siegel, R. A.; Wagner, C. R. *J. Am. Chem. Soc*. **2006**, *128*, 7630–7638. (b) Bai, Y.; Luo, Q.; Zhang, W.; Miao, L.; Xu, J.; Li, H.; Liu, J. *J. Am. Chem. Soc*. **2013**, *135*, 10966–10969. (c) Bilgiçer, B.; Thomas III, S. W.; Shaw, B. F.; Kaufman, G. K.; Krishnamurthy, V. M.; Estroff, L. A.; Yang, J.; Whitesides, G. M. *J. Am. Chem. Soc*. **2009**, *131*, 9361–9367. (d) Bastings, M. M. C.; de Greef, T. F. A.; van Dongen, J. L. J.; Merkx, M.; Meijer, E. W. *Chem. Sci*. **2010**, *1*, 79–88.

(5) (a) Suzuki, Y.; Cardone, G.; Restrepo, D.; Zavattieri, P. D.; Baker, T. S.; Tezcan, F. A. *Nature*. **2016**, *533*, 369–373. (b) Gonen, S.; DiMaio, F.; Gonen, T.; Baker, D. *Science*. **2015**, *348*, 1365–1368. (c) Matthaei, J. F.; DiMaio, F.; Richards, J. J.; Pozzo, L. D.; Baker, D.; Baneyx, F. *Nano Lett*. **2015**, *15*, 5235–5239.

(6) (a) Lai, Y. T.; Tsai, K. L.; Sawaya, M. R.; Asturias, F. J.; Yeates, T. O. *J. Am. Chem. Soc*.,**2013**, *135*, 7738–7743. (b) Lai, Y. T.; Reading, E.; Hura, G. L.; Tsai, K, L.; Laganowsky, A.; Asturias, F. J.; Tainer, J. A.; Robinson, C. V.; Yeates, T. O. *Nat. Chem.* **2014**, *6*, 1065–1071. (c) Bale, J. B.; Gonen, S.; Liu, Y.; Sheffler, W.; Ellis, D.; Thomas, C.; Cascio, D.; Yeates, T. O.; Gonen, T.; King, N. P.; Baker, D. *Science*. **2016**, *353*, 389–394. (d) Hsia, Y.; Bale, J. B.; Gonen, S.; Shi, D.; Sheffler, W.; Fong, K. K.; Nattermann, U.; Xu, C.; Huang, P.; Ravichandran, R.; Yi, S.; Davis, T. N.; Gonen, T.; King, N. P.; Baker, D. *Nature*, **2016**, *535*, 136–139.

(7) (a) Biswas, S.; Kinbara, K.; Niwa, T.; Taguchi, H.; Ishii, N.; Watanabe, S.; Miyata, K.; Kataoka, K.; Aida, T. *Nat. Chem.* **2013**, *6*, 613–620. (b) Yang, G.; Zhang, X.; Kochovski, Z.; Zhang, Y.; Dai, B.; Sakai, F.; Jiang, L.; Lu, Y.; Ballauff, M.; Li, X.; Liu, C.; Chen, G.; Jiang, M.; *J. Am. Chem. Soc*. **2016**, *138*, 1932–1937.

(8) de Greef, T. F. A.; Smulders, M. M. J.; Wolffs, M.; Schenning, A. P. H. J., Sijbesma, R. P.; Meijer, E. W. Chem. Rev. **2009**, *109*, 5687–5754.

(9) ten Cate, A. T.; Kooijman, H.; Spek, A. L.; Sijbesma, R. P.; Meijer, E. W. *J. Am. Chem. Soc*. **2004**, *126*, 3801–3808.

(10) (a) O’Donnell, M.; Kuriyan, J.; Kong, X. -P.; Stukenberg, P. T.; Onrust, R. *Mol. Biol. Cell.* **1992**, *3*, 953–957. (b) Singleton, M. R.; Sawaya, M. R.; Ellenberger, T.; Wigley, D. B. *Cell.* **2000**, *101*, 589–600. (c) Kovall, R. A.; Matthews, B. W. *Proc. Natl. Acad. Sci. U. S. A.* **1998**, *95*, 7893–7897.

(11) The previous work shows that the addition of 20 equiv of apo-form of Cyt b_{562} mostly dissociates the assembling system into the dimer and denatured monomer.[26]

(12) In the assembling system obtained by combining m–FeP′ with the H63C mutant, which has a different heme-attached position, the dilution increases the monomeric component (Figure 3-13). A rigid assembly formed by the N80C mutant reacted with m–FeP indicates a simple shift of molecular weight distribution toward a smaller distribution upon dilution (Figure 3-14).

(13) The isolated component is kinetically stable against concentration in the further evaluations (*vide infra*).

(14) Similar triangular assembly of an engineered cytochrome cb_{562} mediated by Ni coordination has been reported, indicating that Cyt b_{562} intrinsically possesses a tendency to form the trimer.[27]

(15) Oohora, K.; Nishiki, F.; Kajihara, R.; Watanabe, H.; Uchihashi, T.; Hayashi, T. *J. Am. Chem. Soc.* **2018**, *140*, 10145–10148.

(16) Although the SEC measurement takes over 20 min, the obvious and definite peaks observed in SEC traces indicate that the oligomeric components have already formed before the injection. Therefore, it rules out the possibility of the drastic changes of the molecular weight distribution during the SEC measurement. If the oligomerization could occur during the measurement, a broad and undefined trace would be obtained.[26]

(17) This kinetic barrier appears to be generated by the structural changes because the CD signal of the isolated ring structure in the far-UV region is slightly weaker relative to the CD signals of the $(\text{N80C–FeP}')_n$ and Cyt b_{562} (Figure 3-9b).

(18) Kitagishi, H.; Kakikura, Y.; Yamaguchi, H.; Oohora, K.; Harada, A.; Hayashi, T. *Angew. Chem., Int. Ed.* **2009**, *48*, 1271–1274.

(19) (a) Zimm, B. H. *J. Chem. Phys.*, **1948**, *16*, 1093–1099. (b) Matsunami, H.; Fujita, C.; Ogawa, K.; Kokufuta, E. *Colloids Surf. B*, **2007**, *56*, 149–154. (c) Kaszuba, M.; Connah, M. T. *Part. Part. Syst. Charact.* **2006**, *23*, 193–196.

(20) Krieger, E.; Darden, T.; Nabuurs, S. B. Finkelstein, A.; Vriend, G. *Proteins.* 2004, **57**, 678–683.

(21) Duan, Y.; Wu, C.; Chowdhury, S.; Lee, M. C.; Xiong, G.; Zhang, W.; Yang, R.; Cieplak, P.; Luo, R.; Lee, T.; Caldwell, J.; Wang, J.; Kollman, P. *J. Comput. Chem.* **2003**, *24*, 1999–2012.

(22) Wang, J.; Wolf, R. M.; Caldwell, J. W.; Kollman, P. A.; Case, D. A. *J. Comput. Chem.* **2004**, *25*, 1157–1174.

(23) Jakalian, A.; Jack, D. B.; Bayly, C. I. *J. Comput. Chem.* **2002**, *23*, 1623–1641.

(24) (a) Ando, T.; Kodera, N.; Takai, E.; Maruyama, D.; Saito, K.; Toda, A. *Proc. Natl Acad. Sci. U. S. A.* 2001, **98**, 12468–12472. (b) Ando, T.; Uchihashi, T.; Fukuma, T. *Prog. Surf. Sci.* **2008**, *83*, 337–437.

(25) Wendel, M.; Lorenz, H.; Kottthaus, J. P. *Appl. Phys. Lett.* **1995**, *67*, 3732–3734

(26) Kitagishi, H.; Oohora, K.; Hayashi, T. *Biopolymers*, **2009**, *91*, 194–200.

(27) Radford, R. J.; Tezcan, F. A. *J. Am. Chem. Soc.* **2009**, *131*, 9136–9137.

Conclusion

Artificial protein assemblies are promising systems to develop novel functional biomaterials due to the supramolecular structures and the physicochemical properties. Especially, the relationship between the structure and chemical property of the artificial protein assembly is still ambiguous because it is difficult to modulate their structures without changing a large part of the building block. Therefore, the author has focused on the physicochemical properties in a series of Cyt b_{562} assemblies with different supramolecular structures, and particularly investigated the influence of changes of the supramolecular structure induced by slight modification.

In Chapter 1, the author has demonstrated the photoinduced electron transfer between Zn porphyrin (ZnP) and Fe porphyrin (FeP) within an N80C mutant Cyt b_{562} co-assembly or heterodimers with a well-defined rigid structure formed by a cofactor–protein interaction and a hydrogen-bond interaction at the protein interface. The photoinduced charge separation (k_{CS} = 320–600 s^{-1}) and following charge recombination (k_{CR} = 580–930 s^{-1}) were observed in both the rigid co-assembly and heterodimers. Compared with the rigid assembling system, slower electron transfers were observed in the semi-rigid and flexible co-assemblies and heterodimers, which weaken and lack the key hydrogen-bond interaction at the protein interface, respectively. Furthermore, analysis of kinetic constants of charge separation and recombination of the heterodimers using the Marcus theory suggests a single-step electron transfer reaction. These findings provide the strong support that the hydrogen bond network at the protein interface in the rigid assembling system is essential for the efficient electron transfer reactions.

In Chapter 2, the author has investigated cellular uptake of rigid and flexible assemblies of N80C mutant Cyt b_{562}. Multivalent effect of cell-penetrating oligoarginine tag on each protein unit in the assemblies improves the efficiency of cellular uptake of the assemblies into HeLa cells. The efficiency depends on the number of arginine residues in the tag and the rigidity of the whole assembling system. Especially, the rigid assembly with tetraarginine tags is incorporated into the cell with 10-fold higher cellular uptake efficiency than the corresponding assembly without arginine tags. These results indicate that the pre-organized oligoarginine moieties in the rigid helical structure of the assembly induce the more efficient multivalent effects than randomly orientated oligoarginine moieties in the flexible assembly.

In Chapter 3, the author has found that the N80C mutant Cyt b_{562} modified by the heme moiety with a moderately long linker exhibits the reversible transformation between long linear assemblies and a ring-shaped trimer. The ring-shaped trimer is thermodynamically more stable than linear assemblies in a dilute condition. The formation of the ring-shaped trimer occurs within 5 min upon cooling after heat denaturation, whereas the isolated ring-shaped trimer using size exclusion chromatography is kinetically stable to enable the concentration and detailed analysis of ring-shaped trimer. The atomic force microscopy (AFM) images show the ring-shaped objects with ca. 15-nm diameter, which is consistent with the simulated AFM images using the model structure of ring-shaped trimer.

Thus, the author has found that the changes of the supramolecular structures of the Cyt b_{562} assemblies significantly affects the physicochemical properties. Particularly, the small change of rigidity of the assembling system would provide a significant effect on the characteristics of the whole assembly. The author believes that these findings will provide important insights into the refined design of novel functional biomaterials using protein assembling system such as efficient electron conducting nanomaterial in living cells, drug delivery system, stimuli-responsible nanomaterial.

List of Publications for This Thesis

1. Photoinduced Electron Transfer within Supramolecular Hemoprotein Co-assemblies and Heterodimers Containing Fe and Zn Porphyrins
   Ryota Kajihara, Koji Oohora, Takashi Hayashi
   Journal of Inorganic Biochemistry. **2019**, *193*, 42–51.
2. Arginine Residues Provide a Multivalent Effect for Cellular Uptake of a Hemoprotein Assembly
   Koji Oohora, Ryota Kajihara, Misa Jiromaru, Hiroaki Kitagishi, Takashi Hayashi
   Chemistry Letters. in press
3. A Ring-shaped Hemoprotein Trimer Thermodynamically Controlled by the Supramolecular Heme–Heme Pocket Interaction
   Koji Oohora, Ryota Kajihara, Nishiki Fujimaki, Takayuki Uchihashi, Takashi Hayashi
   Chemical Communications. **2019**, *55*, 1544–1547.

Supplementary Publication

1. Supramolecular Hemoprotein Assembly with a Periodic Structure Showing Heme–Heme Exciton Coupling
   Koji Oohora, Nishiki Fuijmaki, Ryota Kajihara, Hiroaki Watanabe, Takayuki Uchihashi, Takashi Hayashi
   Journal of the American Chemical Society, **2018**, *140*, 10145–10148